Reaction Spheres for Attitude Control of Microsatellites

Zhu, L.

DOI
10.4233/uuid:9d0f7b28-dc4e-43b8-b838-84dc15b19b04

Publication date
2021

Document Version
Final published version

Citation (APA)
Zhu, L. (2021). *Reaction Spheres for Attitude Control of Microsatellites*. [Dissertation (TU Delft), Delft University of Technology]. https://doi.org/10.4233/uuid:9d0f7b28-dc4e-43b8-b838-84dc15b19b04

REACTION SPHERES FOR ATTITUDE CONTROL OF MICROSATELLITES

REACTION SPHERES FOR ATTITUDE CONTROL OF MICROSATELLITES

Dissertation

for the purpose of obtaining the degree of doctor
at Delft University of Technology
by the authority of the Rector Magnificus, Prof. dr. ir. T.H.J.J. van der Hagen,
chair of the Board for Doctorates,
to be defended publicly on
Thursday 28 October 2021 at 12:30 o'clock

by

Linyu ZHU

Master of Science in Navigation, Guidance & Control,
Northwestern Polytechnical University, Xi'an, China,
born in Xuchang, Henan Province, China.

This dissertation has been approved by the promotors.

Composition of the doctoral committee:

Rector Magnificus,	chairperson
Prof. dr. E.K.A. Gill,	Delft University of Technology, promotor
Dr. J. Guo,	Delft University of Technology, promotor
Independent members:	
Prof. dr. ir. J.L. Herder,	Delft University of Technology
Prof. dr. E.J.E. Cottaar,	Eindhoven University of Technology
Prof. dr. E. Stoll ,	Technical University of Berlin
Dr. ir. H. Polinder ,	Delft University of Technology
Dr. E. Onillon ,	Swiss Center for Electronics and Microtechnology
Prof. dr. L.L.A. Vermeersen ,	Delft University of Technology, reserve member

This research was funded by the China Scholarship Council (CSC), and also supported by Delft University of Technology.

Keywords: reaction sphere, electromagnetic induction, field modeling, performance analysis, motion coupling.

Printed by: Ipskamp Printing

Cover by: Linyu Zhu

ISBN 978-94-6366-460-8

An electronic version of this dissertation is available at
http://repository.tudelft.nl/.

To my loving family.

CONTENTS

SUMMARY

In past decades, small spacecraft have raised worldwide interest for their low cost and short development time. In general, three reaction wheels are needed for three-axis attitude control of general satellites. However, for small spacecraft where both volume and power budgets are limited, employing three wheels is a challenge. Therefore, reaction spheres are proposed as a replacement for reaction wheels. In a reaction sphere, the spherical rotor is driven by forces generated between the stator and the rotor. Since the rotor's spin axis and the output torque could be about any desired axis in the 4π space, a single reaction sphere could be sufficient to implement three-axis control. Till today, various reaction spheres have been developed, but their performances are far from satisfactory. A better understanding of reaction spheres is needed and great improvements of these actuators are expected especially for small satellites.

This dissertation aims at performance modeling of reaction spheres. Through the modeling process, restricting factors of performances and possible improvements are investigated. This work is focused on induction-based reaction spheres (IBRSs), which are selected as the most promising type of reaction sphere for applications to small spacecraft.

The research starts with an in-depth review and analysis of existing reaction spheres. Since spherical actuators with multiple degree-of-freedom (DoF) share many characteristics with reaction spheres, they are included in the review too. The driving unit and the bearing, as the two essential parts of a reaction sphere, are investigated respectively. The advantages and disadvantages of each type of driving unit and bearing are addressed. Concerning the application to attitude control of microsatellites and via an analytic hierarchy process (AHP), the configuration of an induction-based driving unit with ball bearings is focused on for the performance modeling. In the reaction sphere, the rotor is composed of a ferromagnetic core with an external copper layer. Around the rotor, three sets of stator windings are placed about three principal axes. As per superposition principle of vector fields, the rotor shall be able to perform rotations about any desired axis when the three winding sets are energized.

The second part of the research is dedicated to the field modeling and torque modeling in the blocked-rotor state. The magnetic field excited by energized stator windings is modeled analytically. Especially, the magnetic flux density distribution along the transverse direction of the winding set is modeled for the first time and it reveals how transverse end effects change the field distribution. The field information is extremely important since it enables the torque calculation in the blocked-rotor state and also provides a basis for the performance modeling through this work.

The third part of the research focuses on single-axis rotations where the spin axis of the rotor is aligned with that of the revolving magnetic field excited by stator windings. Its performance modeling is conducted through the equivalent circuit approach. Involved circuit parameters are derived from the analytically modeled field distribution.

In this way, performances of the current-controlled reaction sphere, such as the torque-speed curve, the achievable maximum torque, and the corresponding slip frequency can be obtained. Compared to the finite element method (FEM) or experiments on prototypes, the proposed analysis method saves time and costs significantly.

The last part of the research investigates the performance of arbitrary-axis rotations. When the spin axis of the rotor is not aligned with that of the revolving magnetic field, a resistant torque is generated in addition to the expected driving torque. This phenomenon is referred to as motion coupling. Torques influenced by the motion coupling are modeled based on the study results of single-axis rotations and through a hybrid FEM-analytical approach. The developed torque model is applied to an aerostatic-bearing supported electrodynamic reaction sphere.

This dissertation provides an in-depth study of IBRSs. Firstly, the relation between design parameters of IBRSs and their single-axis rotation performances is studied systematically for the first time. Secondly, the research offers a revealing insight into motion coupling involved in arbitrary-axis rotations, which was rarely studied in the past.

SAMENVATTING

Vanwege hun lage kosten en kortere ontwikkelingstijd hebben kleine ruimtevaartuigen de laatste decennia internationaal de aandacht getrokken. Voor 3-assige standregeling van conventionele satellieten zijn vaak drie reactiewielen nodig. Het is echter een probleem om drie wielen te gebruiken voor piepkleine ruimtevaartuigen met beperkte ruimte en energiebudgetten. Daarom worden reactiebollen aangeboden als vervanging voor reactiewielen. De bolvormige rotor wordt voortbewogen door krachten tussen de stator en de rotor in een reactieveld. Omdat de wervelas en het uitgangskoppel van de rotor om elke as in de 4π ruimte kunnen liggen, zou de uitvoering van drie-asbesturing voldoende kunnen zijn door een unieke reactiebol. Er zijn tot op heden verschillende reactiebollen geproduceerd, maar hun prestaties zijn niet toereikend. Er is een grotere kennis van reactiebollen nodig, en er wordt een aanzienlijke vooruitgang van deze actuatoren verwacht, vooral voor kleine ruimtevaartuigen.

Deze dissertatie beoogt de prestaties van reactiebollen te modelleren. Beperkende prestatiefactoren en potentiële verbeteringen worden onderzocht door middel van het modelleerproces. Dit proefschrift richt zich op inductie gebaseerde reactiebollen (IBRS), die voor gebruik in kleine ruimtevaartuigen worden beschouwd als de meest veelbelovende soort reactiebol.

De studie begint met een grondig onderzoek en analyse van bestaande reactiebollen. Sferische actuatoren met talrijke vrijheidsgraden (DoF) worden in het onderzoek opgenomen omdat zij veel kenmerken met reactiebollen gemeen hebben. De aandrijfeenheid en het lager, als twee kritische componenten van een reactiebol, worden afzonderlijk bestudeerd. Elk type aandrijfeenheid en lager wordt besproken in termen van voor- en nadelen. Aangezien de toepassing standregeling van een microsatelliet is en gefilterd wordt door hiërarchische analyse (AHP), zal de prestatiemodellering worden uitgevoerd voor een structuur als een aandrijfmechanisme op basis van elektromagnetische inductie en kogellagers. De rotor in de reactiebol bestaat uit een ferromagnetische kern met een buitenbekleding van koper. Drie sets statorwikkelingen zijn rond de rotor gerangschikt langs drie hoofdassen. Wanneer de drie wikkelingen worden geactiveerd, moet de rotor volgens het superpositiebeginsel van vectorvelden om elke as kunnen draaien.

Het tweede deel van de studie is gewijd aan veld- en koppelmodellering in de geblokkeerde-rotor toestand. Analytische modellering wordt gebruikt om het magnetisch veld te simuleren dat door aangedreven statorwikkelingen wordt opgewekt. Voor het eerst wordt de verdeling van de magnetische fluxdichtheid in de dwarsrichting van de wikkelingenset gemodelleerd, waardoor duidelijk wordt hoe het transversale gevolgen de veldverdeling wijzigt. De veldinformatie is van cruciaal belang omdat zij de berekening van het koppel in de geblokkeerde-rotor toestand mogelijk maakt en tevens als basis dient voor de prestatiemodellering in deze studie.

Het derde deel van de studie richt zich op rotaties met één as, waarbij de rotoras is uitgelijnd met het roterende magnetische veld dat door de statorwikkelingen wordt

gecreëerd. De werking wordt gemodelleerd met behulp van de equivalente circuitmethode. De analytisch gemodelleerde veldverdeling wordt gebruikt om de circuitparameters te berekenen. De koppel-snelheidskromme, het mogelijke maximumkoppel en de bijbehorende slipfrequentie kunnen alle op deze manier worden bepaald voor de stroomgestuurde reactiebol. In vergelijking met de eindige-elementenmethode (FEM) of prototype-experimenten, bespaart de voorgestelde analytische techniek aanzienlijk tijd en geld.

In het laatste deel van de studie wordt gekeken naar de prestaties van rotaties met willekeurige assen. Wanneer de draaias van de rotor niet is uitgelijnd met de draaias van het roterende magnetische veld, ontstaat een weerstandskoppel naast het beoogde aandrijfkoppel. Bewegingskoppeling is de naam die aan dit verschijnsel wordt gegeven. Koppels die door motion coupling worden veroorzaakt, worden gemodelleerd aan de hand van onderzoeksresultaten op het gebied van eenassige rotatie en een hybride FEM-analytische methodologie. Het resulterende koppelmodel wordt gebruikt voor een elektrodynamische reactiebol die wordt ondersteund door aerostatische lagers.

Deze dissertatie biedt een diepgaand onderzoek naar IBRS. Voor het eerst wordt de relatie tussen IBRS-ontwerpparameters en rotatieprestaties bij één as systematisch onderzocht. Ten tweede werpt de studie een nieuw licht op de bewegingskoppeling bij rotaties met willekeurige assen, waaraan tot nu toe weinig aandacht is besteed.

1

INTRODUCTION

1

1.1. BACKGROUND AND MOTIVATION

In space, due to disturbances caused by radiation, gravity, and other factors, uncontrolled rigid bodies tumble naturally. When a spacecraft needs to keep stabilization or to implement specific attitude maneuvers, attitude determination and control subsystems (ADCS) are of great importance. Attitude control can be conducted passively or actively. In a passive way, spacecraft can keep one-axis stabilized in the inertial frame by making use of angular momentum or external torques. Little energy is consumed on board but the maneuverability of the spacecraft is low. To achieve stabilization with high accuracy or to perform desired maneuvers, active attitude control is necessary. Actuators installed on-board provide forces or torques to stabilize or maneuver the spacecraft.

Commonly used actuators for attitude control include propulsive devices, magnetorquers and momentum exchange devices. Propulsive devices typically provide control forces by expelling mass. With a non-zero arm length, the propelling forces generate control toques which change the rotational state of the spacecraft. Magnetorquers provide control torques by generating a magnetic moment that interacts with the geomagnetic field. The working principle of momentum exchange devices is based on the conservation of angular momentum. Within the closed system composed of the spacecraft body and the momentum exchange device, by changing the rotational motion of the actuator, an amount of angular momentum will be transferred to the spacecraft body.

There are three types of momentum exchange devices, including reaction wheels, momentum wheels and control moment gyros (CMGs). Reaction wheels have a zero nominal momentum, while momentum wheels are spinning at high speeds and have a non-zero nominal momentum. Both of them generate control torques by accelerations about a fixed spin axis. On the contrary, CMGs spin at a high speed and generate control torques by altering their spin axes. Compared to propulsive devices and magnetorquers, momentum exchange devices provide a higher control accuracy [1]. Usually, the space mission requires the spacecraft to be three-axis-controlled, for instance, to keep the camera tracking a specific target. To achieve such goals, at least three wheels or CMGs are needed to provide torques about three independent axes.

In recent years, small spacecraft have attracted worldwide interest for their low cost and short development times. Limited mass and power budgets onboard small spacecraft require ADCS to be miniaturized too. With this need arising, the concept of reaction spheres raised people's attention again. Reaction spheres were already proposed around 1960 [2] but their development was limited by technologies at that time. From the functional aspect, reaction spheres are spherical momentum exchange devices. Different from conventional reaction/momentum wheels or CMGs, no shafts are fixing the sphere to the spacecraft body. Therefore, the spin axis of the spherical actuator is configurable. Rotations and output torques generated by accelerations of the reaction sphere could be about any desired axis in the 4π space. In this way, if redundancy is not considered, a single reaction sphere can sufficiently meet the need for three-axis attitude control. By reducing the number of required actuators, reaction spheres show great benefits in applications to small spacecraft where on-board budgets such as mass and power budgets are limited. Additionally, compared to conventional momentum exchange devices and even magnetically suspended reaction/momentum wheels, there are no fixed shafts connecting reaction spheres to the spacecraft. The influences of fixed shafts are illus-

trated through Euler's dynamic equation of the spacecraft. Involved symbols are given in Table 1.1.

- for spacecraft with conventional reaction wheels:

$$\vec{T}_d = \mathbf{J}_B \frac{\mathrm{d}\vec{\omega}^{B/N}}{\mathrm{d}t}|_B + \vec{\omega}^{B/N} \times \mathbf{J}_B \vec{\omega}^{B/N} + \frac{\mathrm{d}\vec{H}_{RW}}{\mathrm{d}t}|_B + \vec{\omega}^{B/N} \times \vec{H}_{RW}. \tag{1.1}$$

- for spacecraft with reaction spheres

$$\vec{T}_d = \mathbf{J}_{SC} \frac{\mathrm{d}\vec{\omega}^{B/N}}{\mathrm{d}t}|_B + \vec{\omega}^{B/N} \times \mathbf{J}_{SC} \vec{\omega}^{B/N} + \frac{\mathrm{d}\vec{H}_{RS}}{\mathrm{d}t}|_B. \tag{1.2}$$

Table 1.1: Symbols in Euler's dynamic equations

symbols	Meaning
$\vec{T}_d$	the external disturbance acting on the spacecraft
$\mathbf{J}_B$	inertia matrix of the spacecraft with reaction wheels on-board
$\mathbf{J}_{SC}$	inertia matrix of the spacecraft without reaction spheres
$\vec{\omega}^{B/N}$	angular velocity of the spacecraft with respect to the inertial frame
$\vec{H}_{RW}$	angular momentum of the reaction wheel
$\vec{H}_{RS}$	angular momentum of the reaction sphere
$\|_B$	in the spacecraft's body-fixed frame

As per Newton's third law, $\frac{\mathrm{d}\vec{H}_{RW}}{\mathrm{d}t}|_B$ and $\frac{\mathrm{d}\vec{H}_{RS}}{\mathrm{d}t}|_B$ are control torques provided by reaction wheels and reaction sphere onto the spacecraft. The item $\vec{\omega}^{B/N} \times \vec{H}_{RW}$ in (1.1) couples the reaction wheel's angular momentum into the spacecraft's dynamics and leads to gyroscopic torques. To achieve precise control or to minimize power consumption by making use of the gyroscopic torques, measurement of the wheel's angular momentum and an advanced control algorithm are required [3]. For reaction spheres, due to the absence of fixed shafts, no gyroscopic torques are coupled to the spacecraft body. And as a result, the control algorithm can be simplified.

1.2. THE STATE OF THE ART

In this section, a brief review of existing reaction sphere designs is provided. Since induction-based reaction spheres are focused through the work, available torque modeling methods and coupling analysis methods are introduced.

1.2.1. REACTION SPHERES

In past decades, due to the increasing interest in miniaturized ADCS and advanced technologies, a lot of research on reaction spheres has been conducted. Dozens of designs

have been proposed and some have been even manufactured and tested [4]. Basically, existing designs of reaction spheres are derived from electromagnetic motors or piezo/ ultrasonic motors, as illustrated in Fig. 1.1.

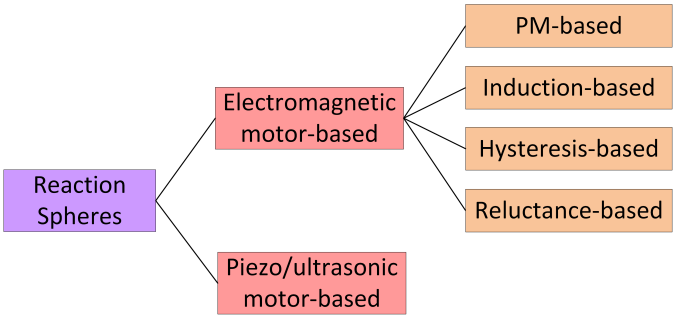

Figure 1.1: Categories of existing reaction spheres.

Fig. 1.2 illustrates a conceptual structure of reaction spheres. The rotor is, of course, spherical and shall be able to perform rotations about any desired axis. The stators, however, can be of any shape and be placed in any position. Even the number of stators within a reaction sphere is not restricted, as long as the stators can drive the rotor's omnidirectional rotation. In electromagnetic motor-based reaction spheres, magnets or alternating currents excite magnetic fields. Driving torques are generated by interactions between the rotor and stators within the electromagnetic field. On the contrary, the working principle of piezo/ultrasonic motors is based on the reverse piezoelectric effect of piezoelectric material. Driving torques are generated by friction forces between the rotor and stators.

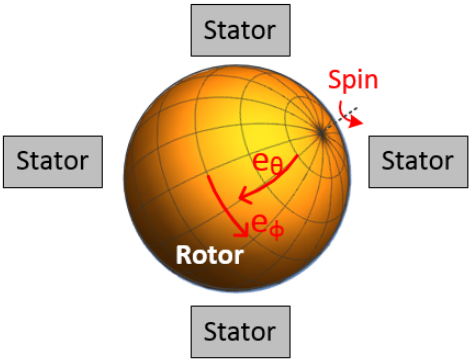

Figure 1.2: The conceptual structure of reaction spheres.

Among electromagnetic motor-based reaction spheres, designs based on permanent magnet (PM) motors and induction motors form the majority. PM motors generate driving torques through the interaction between PMs placed on the rotor and energized

electromagnetic coils placed on the stator. A reaction sphere based on that was proposed by researchers at the Swiss Center for Electronics and Microtechnology (CSEM) in 2006 [5] and a breadboard was manufactured [6]. In closed-loop experiments, the maximum rotational speed of 300 rpm about any desired axis with simultaneous levitation was achieved. Similar designs were presented by researchers at Northrop Grumman Systems Corp [7] in 2014 and China Academy of Space Technology [8] in 2015, respectively. In 2015, the prototype developed by Northrop Grumman went through a zero-gravity parabolic flight and validated its free rotation [9]. Since magnetic fields are excited by PMs and stator currents are only for torque generation, PM motors are more energy-efficient than other electromagnetic motors [10]. However, torques generated by the interaction between PMs and energized electromagnetic coils depend on their relative orientations. To enable 4π rotations, both PMs and electromagnetic coils shall be arranged specially to ensure that driving torques about three independent axes can be generated all the time, irrespective of the rotor orientation. Since coils are fixed on the stator, generated torques depend on the orientation of PMs placed on the rotor. To output required torques, the transient rotor orientation needs to be measured or estimated and specific coils shall be energized. Therefore, this type of reaction sphere requires field sensors, data processing, complicated coil switch strategies and control algorithms, which cause time delays in real-time operations. As a result, the achievable maximum rotational speed in closed-loop experiments is affected.

In induction motors, alternating stator currents excite revolving magnetic fields and induce eddy currents on the conductive rotor. As per Ampere's force law, the force exposed onto a wire of length $\vec{l}$, carrying a current I in the field with magnetic flux density $\vec{B}$ is $\vec{F} = I\vec{l} \times \vec{B}$. Such forces acting on rotor eddy currents result in driving torques. In contrast to PM motors, induction motors have a simple structure of the rotor which is required to be conductive. Therefore, the rotor of an induction motor-based reaction sphere can be made of a single piece of material, which simplifies manufacturing considerably. As per the superposition law of vector fields, when stator windings excite magnetic fields revolving about three independent axes, the resultant torque exerted on the rotor could be about any desired direction and 4π rotation is therefore possible. Since there are no fixed poles on the rotor, the challenge of measuring or estimating the rotor's transient orientation is avoided. Because of the simple rotor structure, a majority of existing reaction sphere designs is based on induction motors. It was first proposed in [11] for the stabilization of a space telescope. Owing to advances in electronics technology, this concept was implemented and tested by many research groups in recent years [12, 13]. In [14], the achieved maximum angular velocity during arbitrary-axis rotations was 18 Hz. Through finite element method (FEM) simulations, it was revealed by [15] that when the spin axis of the rotor is not aligned with that of the revolving magnetic field, a resistant torque will be generated in addition to the expected driving torque. This resistant torque explains the limited maximum speed achieved in arbitrary-axis rotations.

The operation of hysteresis motors is based on the hysteresis effect. The rotor is made of materials with high hysteresis losses and can have a simple structure. However, since the generated torque is proportional to the hysteresis loss, this kind of motor has a low efficiency [16]. A hysteresis motor-based reaction sphere was proposed in [17].

Currently, only one-axis hysteresis drive was implemented and achieved.

Theoretically, reaction spheres driven by reluctance motors are also possible. The operation of reluctance motors depends on salient poles on the ferromagnetic rotor. When stator coils are energized, the rotor salient poles will try to keep aligned with the stator poles such that magnetic flux between them travels through the shortest path. Therefore, reluctance motor-based reaction spheres shall be designed with a special configuration of salient poles in order to perform 4π rotations. Additionally, because torques generated by reluctance motors have a non-linear relation to input currents, the torque modeling is sophisticated.

In piezo/ultrasonic motors, output torques are provided by friction forces between the rotor and the stator. Since their working principle is based on the reverse piezoelectric effect of piezoelectric material, space-consuming windings used in electromagnetic motors are not necessary anymore. Therefore, ultrasonic/piezoelectric motors show distinct advantages in miniaturization. Such a reaction sphere was designed for attitude control of a single-unit CubeSat in [18]. The prototype achieved a rotational speed of 1.3 Hz in the laboratory. Another ultrasonic motor-based reactions sphere was developed in Japan and it achieved the angular speed of 1 Hz about its primary spin axis [19]. Compared to the speed requirement listed in Chapter 3, the angular speed of 1 Hz is too small and the resultant momentum storage capability of the reaction sphere will be extremely limited.

Since piezo/ultrasonic-based reaction spheres have a limited maximum speed while PM-based reaction spheres involve complicated orientation measurements and coil switching strategies, induction-based reaction spheres seem most promising. In the following, research will be therefore focused on induction-based reaction spheres. Its performances of single-axis rotations and arbitrary-axis rotations will be investigated.

1.2.2. TORQUE MODELING OF SPHERICAL INDUCTION MOTORS

Since a motor is designed to drive rotations, its output torque is the most concerning performance. Regarding torque modeling of spherical induction motors, current research mainly focuses on the case of single-axis rotations [13, 14, 20]. When multiple sets of stator windings are energized, couplings are involved and the case becomes complex. A few aspects of research on arbitrary-axis rotations [15, 21] will be discussed in subsection 1.2.3.

Modeling of torques generated by spherical induction motors is usually conducted in two ways. In the first way, the distribution of magnetic flux density within the actuator is modeled analytically. Based on the solved local flux density distribution, electromagnetic torques exerting on the rotor can be calculated through the Maxwell stress tensor. This method is only applicable to single-axis rotations and its accuracy depends on the field modeling. In [20], the magnetic field inside a spherical motor was modeled by converting the spherical structure to an equivalent 2D Cartesian structure. Due to adopted simplifications, considerable differences were noted in the comparison between calculated and experimentally obtained torque-speed curves during single-axis rotations. In cases where meridian shape stator windings [22] are employed for single-axis rotations, the excited magnetic field usually travels along with the $\vec{e}_\phi$ direction. Unit vectors of $\vec{e}_\phi$ and $\vec{e}_\theta$ in the rotor-fixed frame are illustrated in Fig. 1.2. By approximating stator

windings as surface currents composed of azimuthal harmonics and assuming the magnetic vector potential along $\vec{e}_\theta$, an analytical model presenting field distributions within a spherical actuator was given in [23]. This field model was adopted in the study of a spherical induction motor with zenithal traveling waves [24]. During single-axis rotations, calculated torques were close to the experimental results. However, in the model presented by [23], the distribution of magnetic flux along $\vec{e}_\theta$ (i.e., B_θ) is missing. Although B_θ plays a minor role in the torque generation during single-axis rotations, it enhances the understanding of transverse end effects and affects performances of arbitrary-axis rotations. When the geometry of stator windings is complex, the field modeling problem has to be simplified. Otherwise, the flux density distribution cannot be solved analytically. For instance, in designs presented by [14] and [13], magnetic fields were excited by concentrated stator coils. To simplify the torque modeling, the distribution of magnetic flux density was assumed uniform, which deviated from the actual situation greatly.

A generally applicable approach to study generated torques is through numerical simulations or experiments on prototypes. Compared to analytical analysis, this approach is significantly time and cost consuming. Since the rotation of a 3-dimensional rotor is a 3D time-dependent problem, the numerical simulation takes much time and memory resources [25]. However, it has no restrictions on the motor's geometry and can be applied to any complicated cases. Reference [26] analyzed how design parameters of a multiple-degree-of-freedom (DoF) induction motor influence its output torque during single-axis rotations through numerical simulations. When the actuator performs arbitrary-axis rotations where the rotor's spin axis is not aligned with that of the revolving magnetic field, analytical torque modeling becomes impracticable. In such cases, generated torques are usually studied through numerical simulations or experiments on prototypes.

1.2.3. COUPLINGS INVOLVED IN SPHERICAL INDUCTION MOTORS

To drive rotations about any desired axis, multiple sets of stator windings will be integrated into the spherical induction motor. In operations, two basic types of couplings are involved.

Firstly, magnetic fields excited by each winding set overlap. Due to end effects, even if a stator inductor only spans over a limited angle and does not overlap with other inductors, its magnetic field will extend to the area covered by other inductors. In cases where only one set of stator windings is energized with alternating currents, the excited magnetic field will induce voltages in other un-energized stator winding sets. Fortunately, when the winding sets are placed orthogonally, voltages induced in the un-energized winding sets will not lead to stable disturbance thrust forces or torques [27, 28].

Secondly, when more than one set of stator windings is energized, the rotor's spin axis will be unaligned with axes of excited revolving magnetic fields. The misalignment introduces motion couplings. For one energized winding set and its revolving magnetic field, the rotor's angular speed (Ω) can be separated into components parallel with ($\Omega_\parallel$) or orthogonal to ($\Omega_\perp$) the field's revolving axis. As per the working principle of induction motors, the difference between $\Omega_\parallel$ and the mechanical synchronous speed ω_m of the revolving magnetic field results in the driving torque. However, through numerical simulations, it is found that the magnitude of the generated driving torque is smaller than

expected [15, 29]. Additionally, a resistant torque is generated to prevent the relative movement $\Omega_{\perp}$ [15, 21].

Due to difficulties of torque measurements during arbitrary-axis rotations, few experiments were conducted to study the coupling effects. However, they do affect the performances of designed actuators greatly. Currently, in the control of spherical induction motors, thrust forces generated by each inductor are usually assumed decoupled and controlled independently [30, 31]. Since the strength of coupling effects depends on specific designs and their dependencies on design parameters such as the pole-pair number are unclear, sometimes the independent control of each inductor achieves acceptable control performances. However, in most cases, taking couplings into account by empirical equations obtained through analysis or numerical simulations [15, 32] is necessary and improves control performances significantly.

1.3. RESEARCH QUESTIONS

Currently, the development of reaction spheres is still at the technology readiness level 3-4. Although some prototypes are manufactured and tested, their performances are far from satisfactory. Dependencies of output performances on design parameters of reaction spheres have never been systematically analyzed. Additionally, couplings involved in arbitrary-axis rotations are rarely studied. A deeper understanding of the causes and mitigation of these couplings is missing. To fill these gaps, three research questions are posed. They will be addressed through the studies presented in this dissertation.

RQ1: How does a reaction sphere work and what restricts performances of existing reaction spheres?

This question aims at investigating the current research status and defining challenges involved in the development of reaction spheres. Since performances of existing reaction spheres are far from satisfactory, this question also concerns possible improvements of their performances. Restricting factors in achieving desirable performances need to be investigated. Therefore, the research objective corresponding to RQ1 includes a thorough investigation of reaction spheres, and identifying what prevents existing designs from achieving satisfactory performances.

RQ2: How to effectively model performances of an induction-based reaction sphere?

To facilitate real-time control, torques generated by a reaction sphere during rotations shall be modeled and formulated effectively. Besides, characterizing and evaluating the performances of designed reaction spheres before prototyping is of great importance for researchers. A good performance model helps to reduce development times and cost significantly, and also facilitates the optimization and modification process. Therefore, the research objective corresponding to RQ2 is to develop a time and cost-effective model which reveals how design parameters influence performances of an induction-based reaction sphere.

RQ3: What is the biggest challenge to control an induction-based reaction sphere?

The arbitrary-axis rotation of an induction-based reaction sphere is much more complex than its single-axis rotation and is rarely studied. During arbitrary-axis rotations, motion coupling introduces resistance torques and reduces expected driving torques. Control loops of rotations about different directions are coupled. This question concerns how to model driving torques and resistant torques affected by motion coupling. To fa-

cilitate the control of arbitrary-axis rotations, influences brought by motion coupling shall be mitigated. Possible mitigation methods will be proposed by analyzing how design parameters and input parameters of the reaction sphere affect the resistant torque. Therefore, the research objective corresponding to RQ3 includes a brief analysis of the arbitrary-axis rotation of induction-based reaction spheres and in-depth modeling of torques influenced by motion coupling.

1.4. RESEARCH METHODOLOGY

RQ1 is addressed through a literature review. Since driving units and bearings are essential to a reaction sphere, they are investigated extensively to identify what is restricting existing reaction spheres' performances. Different types of driving units and bearings are classified and compared. Through comparisons, the advantages and disadvantages of each type of driving unit or bearing are identified. Surely, these features influence the reaction sphere's overall performance when they are employed. In this way, restricting factors of reaction spheres and possible improvements can be found.

RQ2 is addressed by proposing a reaction sphere design and modeling its torque generation through the field distribution. The driving unit and bearings of the designed reaction sphere are selected from candidates through the analytic hierarchy process (AHP) [33]. Field distribution within the reaction sphere is calculated analytically by transforming Maxwell's equations into governing equations for each region of the reaction sphere. Energized stator windings are approximated as sinusoidally distributed surface currents. Solving governing equations with boundary conditions results in the flux density distribution. Torques generated in the case of blocked-rotor are calculated through Maxwell stress tensor. When the rotor is performing single-axis rotations where the rotor's spin axis is aligned with that of the revolving magnetic field, electromagnetic torques are calculated through the equivalent circuit approach. Involved circuit parameters are obtained through the analytically modeled field distribution. Both field models and torque models are validated through comparisons with corresponding numerical simulation results. Numerical simulations are conducted in COMSOL through the Rotating Machinery, Magnetic physics interface and are reviewed by professionals.

Regarding RQ3, motion coupling is identified as the biggest challenge in the control of an induction-based reaction sphere because it influences driving torques greatly and generates additional resistant torques. Modeling of driving torques and resistant torques is conducted in a hybrid FEM-analytical way. Equivalent circuit parameters corresponding to the movement along $\vec{e}_\phi$ are obtained analytically from the single-axis rotation case. Equivalent circuit parameters corresponding to the movement along $\vec{e}_\theta$ are obtained through a series of numerical simulations. Validation of the hybrid FEM-analytical torque model is conducted through comparisons with corresponding numerical simulation results. All numerical simulations are carried out in COMSOL and are reviewed by professionals.

1.5. THESIS OUTLINE

This thesis consists of seven chapters. Links between chapters and research questions are illustrated in Fig. 1.3.

Chapter 2 addresses RQ1. It presents an overview of driving units and bearings employed in existing reaction spheres. Since they are the two essential components of a reaction sphere, the benefits and drawbacks of each type of driving unit and bearing are discussed and compared in detail.

To facilitate performance analysis in the following, a reaction sphere design is presented in Chapter 3. Since the application to microsatellite attitude control is concerned, design requirements of the reaction sphere are derived from the general control requirements and on-board budgets of microsatellites. The driving unit and the bearing of the reaction sphere are selected through AHP.

To study the torque generation, information on the flux density distribution within the actuator is of high importance. In Chapter 4, electromagnetic fields excited within the reaction sphere are modeled analytically. The developed analytical field models are validated through comparisons with corresponding numerical simulations.

Chapter 5 is dedicated to the performance analysis of the induction-based reaction sphere in single-axis rotations. Dependencies of performances on design parameters are investigated and formulated analytically, which facilitates the optimization with respect to specific objectives greatly.

Chapter 6 addresses RQ3 and focuses on the motion coupling existing in the induction-based reaction sphere. Both the fluctuating driving torque and the fluctuating resistant torque are modeled in a Hybrid FEM-analytical approach. The developed torque model is applied to an electrodynamic reaction sphere prototype. Driving torques and resistant torques calculated from the developed torque model and those obtained from FEM simulations are compared and deviations are discussed.

Chapter 7 concludes this thesis. The main contributions of this dissertation and an outlook to future research are presented.

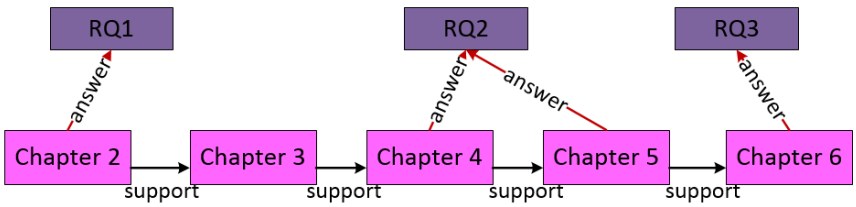

Figure 1.3: Links between chapters and research questions.

2

REVIEW OF REACTION SPHERES

The content of this chapter has been published in Progress in Aerospace Sciences **91**, 67 (2017) [34].

2.1. INTRODUCTION

Concerning spacecraft attitude control, reaction spheres are promising alternatives to conventional momentum exchange devices for the benefits brought by their 4π rotations. Since the first proposal in 1959 [2], many design concepts of reaction spheres have been proposed in past decades. However, they were seldom realized. Developments of the driving unit and the bearing, as well as their combination remain great challenges. To facilitate research and push developments in this field, this chapter provides a comprehensive review of the driving units and bearings of reaction spheres. Since reaction spheres are spherical motors with multiple DoFs, some multi-DoF actuators for different applications, such as robotic joints, are investigated too. Limits of current designs are identified and their causes are analyzed and discussed. Through an in-depth survey, different approaches to excite and support the free 4π rotation are considered, along with their advantages and disadvantages addressed.

2.2. DRIVING UNITS OF REACTION SPHERES

Based on the torque generation methods, driving mechanisms available for reaction spheres are classified into fives groups.

2.2.1. PERMANENT MAGNET-BASED DRIVING UNITS

PM-based driving units utilize interactions between PMs placed on the rotor and electromagnetic coils placed on the stator to generate rotational torques. PM-based driving units have distinct advantages such as high energy density and high efficiency. With the price of rare earth material decreases, PM motors are replacing more and more induction motors. During the past decades, the development of PM-based spherical multi-DoF actuators drew much attention in robotics and automation. However, to enable 4π rotations, the arrangement of PM poles and the activation of stator coils are complicated.

In conventional PM motors, stator coils can be energized with alternating currents (AC) or direct currents (DC). Nevertheless, in spherical PM-based actuators, energizing stator coils with AC is not preferred. This is due to the fixed PM poles. To drive 4π rotations by generating revolving magnetic fields, fixed PM poles shall be placed on the spherical rotor surface with a symmetrical pattern in all great circles [2], which is impossible in real designs and manufacture. Therefore, stator coils in PM-based spherical actuators are usually activated with DC impulses.

As per the arrangement of PM poles, PM-based spherical driving units usually fall into the following two types.

1. SEPARATED ROTATION AND INCLINATION

To avoid restrictions caused by fixed PM poles, the simplest solution is to separate the motion with each DoF.

In [35], a ball-joint-like rotor consisted of eight PM poles evenly distributed on its equatorial line. Electromagnets were mounted circumferentially on the stator's inner surface in two layers, with the total number of 24. Interactions between PMs and the 24 electromagnets actuated the rotor's 3-DoF motion. The rotor's inclination was realized by energizing opposite pairs of coils placed in the upper and lower layers, as shown in

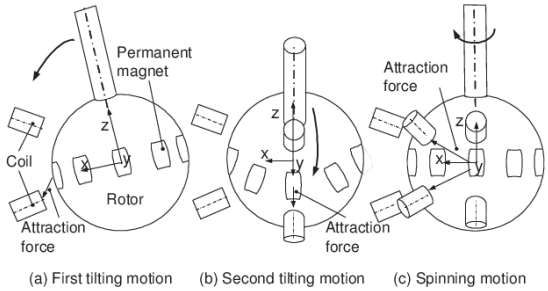

Figure 2.1: The 3-DoF spherical actuator developed in [35] performs tilting motions in (a) and (b) and the spinning motion in (c).

Fig. 2.1 (a) and (b). The maximum tilt angle was ±11° and the maximum torque during the tilt was 0.8 Nm. For spinning about the rotor's axial direction, all circumferential coils would be activated, as illustrated in Fig. 2.1 (c). Its achieved maximum rotational torque was 4 Nm. Depending on specific project requirements, researchers made various modifications to this design, such as increasing the number of coils to improve the tilt angle and achieve better resolution, or employing the rotor outside structure [36]. In [37–39], the alternative PM poles arranged on the sphere equator were replaced with a Halbach array. By comparison, the Halbach array generated a more sinusoidal distribution of magnetic flux density, to suppress higher harmonics and torque ripples.

The drawback of the magnetic configuration mentioned above is the limited inclination range. The maximum inclination angle is restricted by the effective interaction area of rotor poles with electromagnets. Except for adding coils, increasing the number of PMs also extends the inclination range. It is normally implemented by placing a large number of PM poles alternatively on the spherical rotor surface [40, 41]. Usually, polar areas are left blank because it is impossible to arrange PM poles alternatively there.

2. EVENLY DISTRIBUTED POLES

Except for decoupled rotation and inclination where PM poles are placed longitudinally and transversely, another approach to driving 4π rotations is by arranging them symmetrically on the rotor surface. In this way, rotations and inclinations are fully integrated. Correspondingly, stator coils are also distributed evenly with a different symmetrical pattern to avoid locking.

A reaction sphere with eight PM poles on the rotor was presented in [42]. As shown in Fig. 2.2 (a), 20 electromagnets were attached to the stator inner surface. Proper activation of the electromagnets could generate driving torques about any desired axis. Meanwhile, energized electromagnets provided stable levitation to the spherical rotor. A challenge in this design was the alternating magnetization of the sphere. In the original prototype, a mosaic of 728 cylindrical magnets was glued onto the rotor to approximate the eight PM poles [43]. In later optimizations, these magnets were replaced by eight truncated spherical shaped and parallel-magnetized poles [44] to generate a symmetric field. The reaction sphere's rotational velocity could be controlled with an open-loop or closed-loop method which, however, involves complex orientation measurements and velocity estimation [45]. A prototype was developed at the Swiss Center for Electronics

and Microtechnology (CSEM) with a total mass of about 6 kg. In the closed-loop experiments for simultaneous levitation and rotation, the breadboard achieved the angular velocity up to 300 rpm about an arbitrary axis [6].

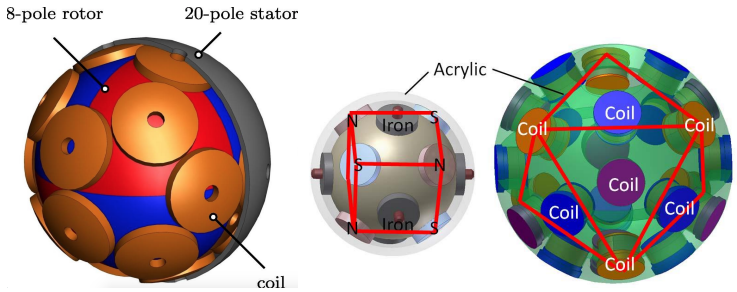

(a) (b)

Figure 2.2: PM-based spherical actuators with evenly distributed poles: (a) stator coils are energized with DC impulses [45]; (b) stator coils are energized with AC inputs [46].

A similar design was presented in [47]. Different from the alternating PM poles arrangement in [42], all 12 PMs inserted onto the rotor had like poles outward pointing. The stator consisted of eight electromagnets following the vertex of a cube. The rotor's rotation axis and angular velocity were controlled by energizing independent electromagnets with impulses in closed loops. Necessarily, parts of the electromagnets were surrounded by magnetic sensors to detect the presence of PM poles and to calculate the rotor's orientation and speed. Due to the fact that like poles point outwards, there shall be no more than one PM pole present in a sensor's sensing range at any time to avoid ambiguities.

Presently, most of the spherical PM motors are stepping-based, where the full rotation range is divided into a number of steps. Some exceptions work like classical synchronous motors but their topology is very special and they do not actually perform 4π rotations. In [46], the 3-DoF stepping motor consisted of a spherical rotor, six spherical ball bearings with air supply and a spherical shell stator. The rotor was attached with a mix of PM poles and iron poles. Their arrangements followed vertexes and face centers of a virtual polyhedron. The detailed configuration is shown in Fig. 2.2 (b). The stator had 25 coils mounted inside. Its driving mechanism was based on conventional three-phase AC motors. Firstly, the rotor's spin axes always cross an iron core's center. The attraction between the iron salient and the corresponding active electromagnet fixed the rotation axis. Secondly, taking advantage of the poles' and coils' topology, it was possible to find a set of coils to energize with three-phase alternating currents and to produce a revolving magnetic field about the specific rotation axis. The actuator's maximum output torque was 13 mNm. It could perform continuous rotations about different directions with a controllable speed from 0.05 rpm to 180 rpm (counter-clockwise) or 300 rpm (clockwise).

The pole and coil arrangement based on regular polyhedrons provides a symmetric magnetic field and eases motion controls. Nevertheless, since the number of regular polyhedrons is limited, how to place a large number of magnets on the sphere evenly

to get a symmetric distribution was a challenge. In [46, 48], a symmetric geometry is approximated by the combination of different polyhedrons. In [49], this problem was addressed by recursively subdividing the sphere using the projections of dual regular polyhedrons on it. The duality refers to the feature that connecting the adjacent face centers of a regular polyhedron forms another regular polyhedron. This approach was applied to the design of a spherical motor with 80 PM poles attached to [50, 51]. In [52], the almost even distribution of stator and rotor poles was obtained by solving the packing and covering problems.

SUMMARY OF PM-BASED DRIVING UNITS

Usually, PM-based driving units have high efficiency, good torque generation capability and a linear relation between input currents to output forces. These characteristics contribute to its wide applications. For reaction spheres, there are three issues to consider.

- The first issue is to avoid unwanted forces or torques brought by ferromagnetic materials. For instance, a coil with an iron core enhances the field density but introduces cogging torques which appear as ripples and jerks in the torque generation. It thus results in disturbances for satellite attitude control.
- The second issue is its sophisticated control. Since torques generated by excited coils depend on their relative positions with respect to the rotor where PMs are attached to, the measurement or estimation of the rotor's transient orientation is a necessity. Based on this information, specific coils will be excited according to the switching scheme. Determining the most effective coil switching strategy is difficult [52, 53]. Although in theory, magnet poles are not required to be placed evenly, an uneven arrangement would complicate the control algorithm [54].
- Another issue is the structural reliability. PMs attached on the surface limit the rotor's mechanical strength and the maximum spin rate.

2.2.2. ELECTROMAGNETIC INDUCTION-BASED DRIVING UNITS

The rotational torque of an induction motor is generated by eddy currents induced on the rotor. As per Faraday's law, a time-varying magnetic field produces a time-varying electric field

$$\nabla \times \vec{E} = -\frac{\partial \vec{B}}{\partial t}\,, \tag{2.1}$$

where $\vec{E}$ is the electric field intensity and $\vec{B}$ is the magnetic flux density. The current density $\vec{J}$ is connected to the electric field intensity by

$$\vec{J} = \sigma \vec{E}\,, \tag{2.2}$$

where σ is the electrical conductivity. Lorentz force acting on the induced eddy current generates the driving torque

$$\vec{T} = \int\int\int \vec{r} \times (\vec{J} \times \vec{B}) \mathrm{d}V\,, \tag{2.3}$$

where $\vec{r}$ is the position vector of the small piece of volume segment $\mathrm{d}V$.

Typically, the rotor of a spherical induction-based actuator is made of two layers. The outer layer is highly conductive for eddy currents' generation and circulation while the inner layer material is with high permeability to enhance the magnetic flux density within the actuator. The layered configuration helps to achieve better performances than a solid conductive rotor. Since there are no fixed poles on the rotor, three-dimensional rotations could be achieved by generating revolving magnetic fields about three principal axes. In [55, 56], three sets of stator windings were placed orthogonally to excite rotations. However, three sets of windings occupy much space and overlap in some areas. To solve this problem, several solutions have been proposed.

1. LINEAR INDUCTORS

The first solution is inspired by linear induction motors. An inductor is a piece of stator back iron wound with AC powered windings to generate traveling magnetic fields. It is different from the stator in conventional motors by its longitudinal ends. For consistency with the rotor geometry, inductors employed in spherical actuators have a curvature. To enable three-dimensional rotations, at least three inductors are needed. They can be arranged askew or orthogonally around the rotor. A prototype based on such an arrangement was developed for applications on mobile robots [30] (see Fig. 2.3 (a)). Four independent inductors were employed to drive 4π rotations. The rotor had an outer diameter of 246.2 mm and a mass of 8.2 kg. Experiments showed that the motor could rotate about an arbitrary axis with the speed up to 300 rpm. The maximum output torque was 4 Nm.

However, this kind of stator arrangement has a very limited torque generation capability. The 4 Nm maximum torque is generated at the cost of heavy electric loading. Although increasing the coverage area of each inductor improves the torque generation capability, interference between inductors is also enhanced and causes disturbances. Additionally, due to end effects, dynamic performances of the actuator would be a concern, especially when it is employed in applications where high precision is required.

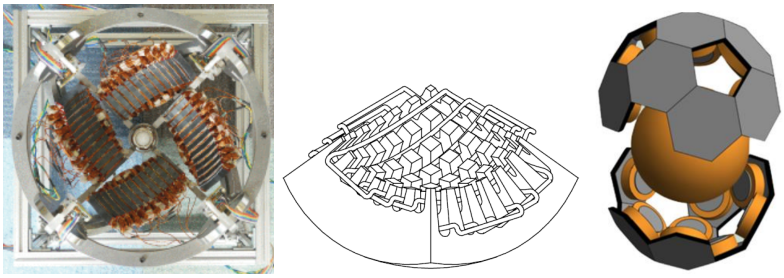

(a) (b) (c)

Figure 2.3: Three types of stators employed in induction-based spherical actuators: (a) linear inductors [30] (b) a meshed stator [22] (c) distributed electromagnets [12]

2. MESHED STATORS

The second solution is the integration of different winding sets in their overlapping area. This idea stems from the spherical induction motor proposed in [57]. Actually, in that design, the rotor only performed one-dimensional rotation, but the grid configuration inspired designs of multi-DoF induction motors. For instance, a 2-DoF spherical induction motor was presented in [22]. The stator was composed of four classical 1-DoF inductors and one 2-DoF inductor. The 2-DoF inductor below the rotor is shown in Fig. 2.3 (b). It was curved with longitudinal and latitudinal slots on its external and inner layers respectively for winding mounting. This configuration allowed the generation of revolving magnetic fields with 2-DoF. However, electromagnetic coupling between windings is the main concern and may result in disturbance torques.

3. DISTRIBUTED ELECTROMAGNETIC POLES

Another option is employing distributed electromagnetic poles to generate a revolving magnetic field. In this way, placing pairs of coils along three independent axes is the most common arrangement [13, 58]. For rotations about one specific axis, four coils placed on the plane orthogonal to the specific axis would be energized with two-phase AC. The generated revolving magnetic field drags the rotor's spinning. Rotations about arbitrary axes are achieved through independent and simultaneous control of coils. In the design proposed in [59], a DC electromagnet was placed above the rotor for Active Magnetic Bearing (AMB) control. In the experiment of one-axis rotation with magnetic levitation, the torque per power was 0.2 mNm/W [60]. Since it was found that the magnetic flux for suspension would introduce disturbance torques to the rotation, air bearings were employed in later experiments for three-dimensional rotations [58]. The rotor was a steel bearing sphere with a mass of 0.173 kg [14]. Its maximum angular velocity achieved in experiments was 18 Hz (about 1080 rpm) and the maximum torque was 1.77×10^{-5} Nm. Similar work was carried out in [13, 61] and a large prototype was developed. The rotor diameter was 100 mm with a mass of 3.45 kg. Although it was allowed to rotate about any direction in theory, only the one-axis rotation was tested. Experiments indicated a maximum speed of 13,500 rpm and a maximum torque of 0.7 Nm.

Based on the distributed stator poles, a more advanced arrangement was proposed in [12, 62]. The spherical actuator was intended for the attitude control of CubeSats. The rotor was a solid sphere made of copper while the stator consisted of 20 ferrite-core coils. Energizing selective coils with AC excites a revolving field and causes corresponding rotation of the rotor. Although a prototype was developed, no experimental performance was reported. Fig. 2.3 (c) illustrates the conceptual arrangement. As per the design, eddy currents induced on the rotor also provide electrodynamic suspension.

A major concern with the distributed pole configuration is the remarkable dimension of the stator. The PM-based reaction sphere presented in Fig. 2.2 (a) and the induction-based reaction sphere presented in Fig. 2.3 (c) have similar stator arrangements. However, their prototypes' dimensional ratios between the stator and the rotor are quite different. In the PM-based actuator, the magnetic field is generated by PMs. Suspensions and rotations of the rotor are provided by Lorentz forces acting on stator coils. However, in the induction-based actuator, the magnetic field is generated by stator coils and weakened by induced rotor currents. Lorentz forces experienced by rotor eddy currents in the

resultant magnetic field provide suspensions and rotations. Since only magnetic flux at the axial end of each coil is utilized and coils are placed in air separately, a large turn number or current input is required to generate a strong magnetic field. For instance, in the prototype demonstrated by [58], the dimensional ratio of the rotor to the whole actuator was almost 1:8.

SUMMARY OF INDUCTION-BASED DRIVING UNITS

Compared with other electromagnetic motors, induction motors have the benefits of simple rotor construction, low cost and high reliability [63]. For a long time, induction motors were the most commonly used motors in industries. Meanwhile, their weaknesses are low efficiency and unwanted eddy currents. A performance analysis of different spherical rotors was conducted in [22]. The layered rotor with ferromagnetic teeth (see Fig. 2.4 (a)) shows higher efficiency and output torques than both the layered rotor and the homogeneous conductive rotor. However, its best efficiency in tests was merely 1%. Unwanted eddy currents in conventional motors can be removed by employing a cage to guide their circulation. However, for a sphere performing 4π rotations, guiding induced currents is difficult. A 2-DoF spherical induction motor with eddy currents guiding was discussed and compared to its counterpart without guiding in [64]. The presented rotors had slotted (see Fig. 2.4 (b)) or smooth external surfaces. For the slotted-surface type, conductive and non-conductive material covered the rotor surface alternatively. In this way, the circulation of eddy currents would follow designed paths. For the smooth type, the rotor was covered by a thin layer of copper where the circulation of induced currents was uncontrolled. In both structures, the stator consisted of four inductors symmetrically surrounding the rotor with six slots on the inner surface. Through simulations conducted in OPERA-3D, it was found that the rotor with a slotted surface had a starting torque half that of the slotted one.

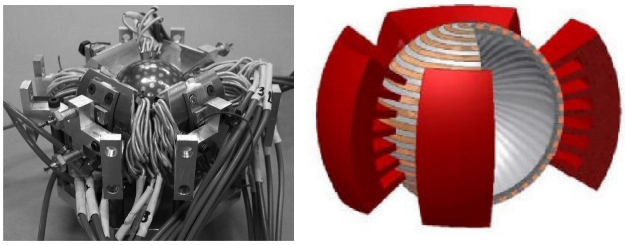

(a) (b)

Figure 2.4: Special rotor designs: (a) a layered rotor with ferromagnetic teeth [22] (b) a slotted rotor for eddy currents guiding [64]

Besides, eddy currents generate heat and could cause thermal issues. In tests of the next generation ultra-high-speed induction motor [65, 66], the temperature of the steel rotor (with a diameter of 4 mm) increased to 50°C when the revolving magnetic field's speed was 1.5 kHz. Additionally, unwanted eddy currents may induce vibrations [67].

2.2.3. HYSTERESIS-BASED DRIVING UNITS

Hysteresis motors are made of magnetic material with high hysteresis losses and their operation depends on the hysteresis effect. When a revolving magnetic field is generated, magnetization would be produced in the rotor and its axis always lags behind the stator poles. In this way, attractions between stator poles and rotor poles form the hysteresis torque, pushing the rotor to spin with the field synchronously. Different from PM motors and reluctance motors, hysteresis motors do not need salient poles. Magnetic locking between the stator and the rotor is ensured by the high retentivity. Besides, the hysteresis torque is constant, independent of the rotor speed.

The feasibility of applying a hysteresis-based driving unit to a reaction sphere was explored in [68]. The design and tests of a magnetically suspended reaction sphere with a one-axis hysteresis drive were discussed. Experiments on the prototype showed that 12,000 rpm could be reached under laboratory conditions and a starting torque of 8.15 mNm was achieved. The total mass including the rotor (with a diameter of 54 mm), the stator and electromagnets was 1.05 kg. Power consumption of steady-state was 3.44 W at 1800 rpm.

Hysteresis motors have simple rotor structures, self-starting capability, and quiet operations. It permits the rotor to be made of a single piece of steel, which greatly simplifies manufacturing and enhances structural strength. However, this kind of driving unit has low efficiency since the generated torque is proportional to the hysteresis loss. Additionally, their output torque per unit volume is low. For instance, with the same dimensions, the output of a hysteresis motor is only about one-quarter of that generated by an induction motor [69].

2.2.4. RELUCTANCE-BASED DRIVING UNITS

Reluctance motors require salient poles on the ferromagnetic rotor. When stator coils are energized, magnetic flux flows through the air gap between the stator and the rotor. The magnetic reluctance of the air gap can be calculated as

$$R_{mg} = l_g / \mu_0 A_g \,, \tag{2.4}$$

where μ_0 is the permeability of vacuum, l_g and A_g are the length and the cross-sectional area of the air gap respectively. The rotor poles always try to move to complete the magnetic flux path with the minimum reluctance. In this way, rotation torques are generated. Practically, there are two major difficulties involved in reluctance-based spherical actuators.

- Firstly, to prevent uncontrolled motions such as one active coil attracts more than one iron pole, sizes and arrangements of coils and iron poles shall be elaborately designed.
- Calculating input currents of coils to obtain the desired motion is a challenge. The difficulty stems from the nonlinear relation between input currents and output torques.

A spherical reluctance motor was presented in [70]. As shown in Fig. 2.5 (a), 104 salient poles were placed evenly on the rotor surface [71]. Each stator was wound with

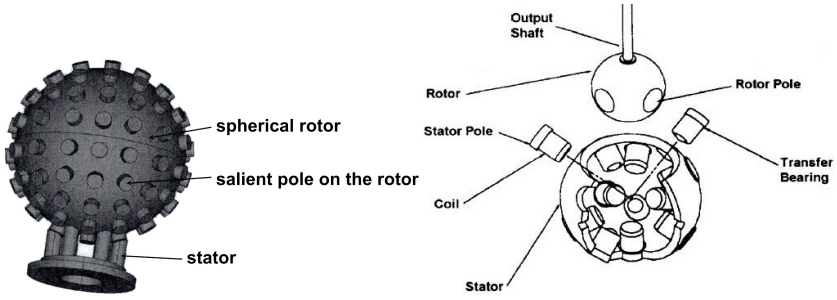

(a) (b)

Figure 2.5: Reluctance-based spherical actuators presented in (a) [70] and (b) [73]

AC windings to drive rotations about its axial axis. With five stators placed along three independent axes, the actuator was expected to perform 3-DoF rotations. Through further study, it was found that electromagnetic couplings between suspensions and rotations, and the complex control strategy result in a lack of precision [72].

A 3-DoF variable reluctance (VR) spherical motor was described in [54, 73]. As shown in Fig. 2.5 (b), the motor was composed of two concentric spheres. The rotor was with evenly distributed iron poles. Coils were distributed on the stator surface with a different arrangement to avoid locking. A real-time control strategy for the reluctance motor was developed in [74]. The control scheme was based on a look-up table which contained information for the rotor's 972 orientations. Based on the rotor's real-time orientation which was measured by encoders, information in the table was used for the computation of currents. A general torque model for the design was developed in [75] by the principle of virtual work. The torque-current relation had a quadratic form and it made the closed-loop motion control complicated [74]. Therefore, in the updated version of the reluctance motor, iron poles on the rotor were replaced by PMs which led to a linear torque-current relation. Since both PM-based and reluctance-based spherical driving units are stepping-based, hybrid PM-reluctance designs are quite common [76, 77].

Reluctance motors have distinct benefits of large torque density and simple structures. Their main drawback is the inherent nonlinear torque-current relation which complicates servo control. Additionally, large torque ripples might occur due to the rotor's saliency.

2.2.5. PIEZO/ULTRASONIC MOTOR-BASED DRIVING UNITS

In past decades, piezoelectric and ultrasonic motors have received much attention. Ultrasonic motors belong to piezoelectric motors and both of them are based on the reverse piezoelectric effect of piezoelectric material [78]. They transfer electrical energy into high frequency mechanical vibrations. Rotational torques are offered by frictional forces between the rotor and the stator. The difference between ultrasonic motors and piezoelectric motors is that ultrasonic motors use resonance to amplify the vibration and the vibration is normally at the ultrasonic frequency range [78]. Compared with electromagnetic motors, piezo/ultrasonic actuators have the advantages of simple ro-

tor structure, high torques at low speeds and a short response time [79]. They are easily miniaturized and can be very compact. Typically, there are two ways to realize a multi-DoF piezo/ultrasonic motor.

1. MULTIPLE STATOR UNITS

The first way to drive 4π rotations is by employing more than one stator unit. Each stator unit excites the rotor's rotation about one axis. For instance, [80] proposed an ultrasonic-based reaction sphere. The rotor was held by three stator units placed along three orthogonal axes respectively. Each stator unit provided driving torques about one axis. Rotations about arbitrary axes were implemented by activating the three stator units simultaneously. In this design, the rotor radius was 50 mm [81]. When working at the resonance frequency of 14 kHz, the actuator could achieve the speed of 6.28 rad/s about one independent axis. However, the maximum speed about arbitrary axes was only 0.889 rad/s. The poor performance resulted from cross-couplings involved in the combination of driving torques generated by two or more stator units. Besides, the high power consumption was a problem, which was 45 W at the rotational speed of 6.28 rad/s. To minimize interference between rotations about different axes, torque generation and transfer for each axis were separated in the improved design [81]. Six ultrasonic motors replaced the three stator units and each of them was equipped with a rotor kicker. The kickers held and transferred rotational torques to the spherical rotor at the contact point. Two opposite kickers formed a pair, providing torques about one independent axis. Driving torques about an arbitrary axis were obtained by superposition of three orthogonal components. The original and updated designs are compared in Fig. 2.6 (a). Due to the decoupled torque generation and transfer, the maximum rotational velocity about arbitrary axes increased to 5.66 rad/s. At the angular velocity of 6.28 rad/s, the power consumption decreased to 6.4 W [19]. Although employing multiple stator units to realize multi-DoF driving is straightforward and relatively easy to implement, it has the drawback that unused stator units generate additional loads and heat to the rotor when other stator units are activated.

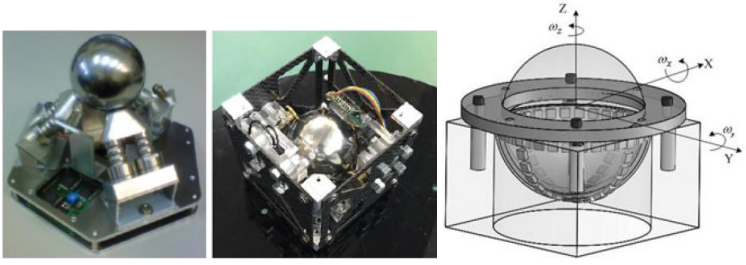

(a) (b)

Figure 2.6: Piezo/ultrasonic motors with multiple stator units: (a) the original (left) and updated (right) reaction spheres presented in [81] (b) the spherical actuator presented in [82].

Inspired by the idea of employing multiple stator units, an innovative design was presented in [82]. It utilized distributed actuators to form a linear stator unit. As illus-

trated in Fig. 2.6 (b), many piezoelectric actuators were placed along three independent curves around the spherical rotor. When actuators along one curve were energized with a phase difference between adjacent actuators, traveling waves would be formed and the rotation about one axis would be excited.

2

2. COMBINATION OF VIBRATION MODES

Another approach to realizing 3-DoF rotations of a spherical piezo/ultrasonic motor is through combining a single vibrator's different vibration modes. In [18, 83], a piezoelectric reaction sphere suitable for CubeSats was developed. The actuator comprised a ferromagnetic sphere, a PM, a piezoelectric element and the intermediate element. The attraction between the ferromagnetic sphere and the PM provided the pressure for torque transfer and ensured their contact in space. The novelty in this design was the symmetrically sectioned electrodes of the piezoelectric element which was a cylinder or hemisphere (see Fig. 2.7 (a)). They were energized independently with respective input controls. The sphere's 3-dimensional rotations were driven by activating the three electrodes in different modes. With a diameter of 25 mm, the steel sphere could generate a torque of 2.33x10^{-4} Nm by accelerating up to 8.3 rad/s.

The same approach was adopted in the design presented in [84]. As illustrated in Fig. 2.7 (b), three layers of piezoelectric ceramic plates were integrated into the stator. Two of them were activated in bending modes and the third one in the longitudinal mode. Exciting two out of the three modes drove the rotation about one independent axis.

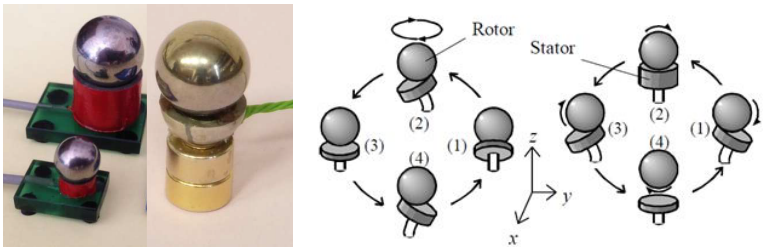

(a) (b)

Figure 2.7: Piezoelectric-based actuators driven by (a) a single piezoelectric element with sectioned electrodes [18] (b) a single stator unit integrated with multiple piezoelectric plates [84].

SUMMARY OF PIZEO/ULTRASONIC-BASED DRIVING UNITS

In most cases, piezo/ultrasonic motors have a solid contact between the stator and the rotor for high torque transfer capability [85]. However, the sliding friction leads to wear, heating, limited spin rates and a short lifetime. After a long time of continuous operation, damages can happen to the piezoelectric material, degrading the motor's performances greatly. In contrast to electromagnetic motors, contact piezo/ultrasonic motors have much lower rotational speeds and efficiency. The maximum spin rate of a contact ultrasonic motor is only several hundred rpm [79]. To overcome the drawbacks of wear and low speed, the direct contact in piezo/ultrasonic motors could be replaced by

a non-direct contact. In such cases, the ultrasonic motor transfers the torque through liquid or air existing in the gap. Meanwhile, support of the rotor comes from nonlinear acoustic phenomena, such as acoustic radiation pressure [85]. Without restrictions from the stator, the rotor can reach a much higher speed, up to almost ten thousand rpm [86]. The operation time can be extended at the price of much lower output torque than its contact type counterpart.

A non-contact spherical ultrasonic motor was presented in [87]. The stator had a hollow bowl shape configuration. Utilizing near-field acoustic levitation, the rotor was suspended by acoustic radiation pressure in the gap. Traveling waves at the stator's inner surface excited rotations, with a speed of 1071 rpm. Heating was noticed to be an issue during experiments and was supposed to limit the rotary velocity. Presently, no multi-DoF non-contact ultrasonic motor has been developed yet.

For space applications, a distinct advantage of ultrasonic motors is that no electromagnetic interference is introduced. Magnetic field sensing would not be interfered. Besides, their compact structures show great benefits for small and miniature spacecraft. However, their drawback is the limited speed. Neither designs proposed in [18] or [81] exceeded 10 rad/s. Although non-direct contact ultrasonic motors achieve higher velocities than the direct contact type, their maximum speed is limited by the amplitude of vibrations [88]. Restricted by current technologies, the achievable speed about 10,000 rpm [86] is far behind the speed limit of commercial electromagnetic motors. Additionally, the sealing requirement of non-contact ultrasonic motors renders their implementation in space missions limited. Furthermore, for both contact type and non-contact type, the pressure between the rotor and the stator is necessary to ensure torques transfer. Therefore, additional elements are needed to provide the preload when they are used in micro-gravity environments.

2.2.6. SUMMARY OF DRIVING MECHANISMS

In Table 2.1, characteristics of each driving mechanism are listed, with corresponding approaches to realizing multi-DoF motions, advantages, and disadvantages. Hysteresis-based driving units shall be able to drive omnidirectional rotations in theory but the feasibility has not been proven yet. Reluctance-based driving units share many features with the PM-based type. However, the nonlinear torque-current relation makes people much prefer PM-based driving units. The speed limit of piezo/ultrasonic-based driving units is a big weakness. For the attitude control of spacecraft, the limited maximum speed will lead to a limited momentum storage capability. Therefore, PM-based and induction-based driving units seem most promising among the listed candidates.

2.3. BEARINGS OF REACTION SPHERES

The function of bearings is to support the rotor, keeping its position and spin axis during rotations. For a reaction sphere, the challenge is how to integrate bearings into the freely rotating actuator. As presented in section 2.2, several reaction sphere prototypes based on induction, PM or piezo/ultrasonic driving units have achieved arbitrary-axis rotations, but their performances are far behind that of commercial reaction wheels. Problems lie in the inefficient driving of 4π rotations and the negative effects produced by

Table 2.1: Characteristics of driving units of multi-DoF spherical actuators.

Types	Approaches	Advantages	Disadvantages
PM	• decoupled DoFs • evenly distributed PMs	+ high efficiency + linear torque-current relation	- fixed poles - cogging torque - complex coil switching strategy - low reliability
Induction	• multiple linear inductors • meshed stators • distributed stator poles	+ simple rotor structure + low cost + high reliability	- low efficiency - unwanted eddy currents
Hysteresis	• multiple linear inductors • meshed stators • distributed stator poles	+ simple rotor structure + high reliability	- low efficiency -low output torque per unit volume
Reluctance	• decoupled DoFs • evenly distributed iron poles	+ large torque density	- fixed poles - torque ripples - nonlinear torque-current relation - complex coil switching strategy
Piezo/ ultrasonic	• multiple stator unites • combination of vibration modes	+ simple rotor structure + easy miniaturization	- limited speed

bearings. For example, the reaction sphere proposed in [59] was designed with AMBs, but suspension magnetic flux introduced disturbance torques to rotations. Therefore, air bearings were employed in the experiment of three-dimensional rotations [14].

In the 1960s, potential bearings for reaction spheres were compared in [89] and electrostatic suspension got some superiority in contrast to air bearings, fluid bearings, and magnetic bearings. However, due to technology advancements in past decades, a different conclusion may be drawn today. Below, commonly used bearings in reaction spheres and multi-DoF spherical actuators are investigated.

2.3.1. ELECTROMAGNETIC BEARINGS

In the evaluation given in [89], magnetic bearings were discarded for lowered motor efficiency caused by the relatively large air gap, couplings between the bearing and the driving unit, as well as its instability with the absence of active feedback controls.

It was mathematically shown that both gravity and magnetism are harmonic potential fields without a minimum [90]. Hence, stable passive levitation of paramagnetic or ferromagnetic material is impossible. However, there are several known exceptions:

- Diamagnetic materials and superconductors for their negative susceptibility;

- Levitron for the changing field direction seen by the rotor [91];
- Electrodynamic bearings (referred to as induction bearings in some literature) for induced eddy currents;
- Ferrofluids for the automatic equilibrium seeking [92];
- Feedback controls, including AMBs and tuned LC circuit bearings [93].

Among these exceptions, only electrodynamic bearings and feedback control are often employed in reaction sphere designs. This is because repulsion forces provided by normal diamagnetic materials are too weak [94, 95]. Superconductive materials require specific temperature conditions and Levitron's precession would introduce disturbances in the spacecraft's attitude control [91]. Ferrofluid suspension is a promising support method. It is passively stable [92] and can reduce permeability variation which leads to cogging torques [96]. The idea of filling in the gap of spherical induction motors with ferrofluid was proposed in [97]. Since maximizing the permeability in the gap would reduce magnetic reluctance in the circuit, this solution could lead to increased efficiency and decreased magnetizing currents [98]. However, considerable drag exists because of the ferrofluid's high viscosity [99]. This characteristic forbids its application in high-speed devices. There is no implementation or test known for ferrofluid bearings in multi-DoF spherical actuators.

ELECTRODYNAMIC BEARINGS

Eddy currents in electrodynamic bearings can be excited by relative motions or AC powered electromagnets. In the first case, levitation becomes stable when the object moves at speeds higher than a threshold. It has been successfully applied to high-speed trains. Electrodynamic bearings, which are referred to as induction bearings, are excited by AC electromagnets and are statically stable. In the designs proposed in [12, 62, 100], AC coils placed around the rotor provided both induction-based driving and suspension. Different from the typical rotor structure described in section 2.2.2, the rotor in such designs is without a ferromagnetic core. This is to avoid attractive forces generated between the rotor core and the stator back iron, which has a negative stiffness and complicates the bearing control. The absence of the ferromagnetic core reduces the magnetic flux density within the actuator, as well as the resultant torque generation capability. Besides, with usual conductive materials, electrodynamic bearings cost a lot of energy and have heating issues [101]. Furthermore, a rotating conductive object suspended with such bearings has poor damping [102, 103]. So far, simultaneous suspension and one-axis rotation has been realized and reported [100].

ACTIVE MAGNETIC BEARINGS

AMB with feedback control is the most common electromagnetic bearings. Despite the disadvantages mentioned in [89], it has been more and more commonly employed in space projects. AMBs eliminate noises and instabilities in mechanical contact bearings [104] and aero/hydrodynamic bearings, avoid the high resource requirement of aero/hydrostatic bearings and the difficult implementation of electrostatic bearings in

space. In theory, through feedback controls, AMBs could provide adjustable and unlimited stiffness. Furthermore, the contact-less support and the relatively large air gap of AMBs lowers the requirement for manufacturing tolerance. Depending on specific applications, the degree of freedom of AMBs can be designed from 1 to 6. A flywheel with 5-DoF AMBs was developed in [105] and it could tilt at a high rate. Its bandwidth was much higher than that of conventional flywheels and was very suitable to counteract high-frequency disturbances.

Six-DoF AMBs integrate driving and supporting functions, such as the reaction spheres proposed in [42, 47]. Forces generated by stator coils provide normal support and tangential driving simultaneously. In most cases, even if both driving and support are electromagnetic-based, their controls and activation are separated to minimize coupling and complexity [106].

The control bandwidth of an AMB is limited by switching of coils, measurements of sensors and the processing capability of controllers [107], especially when they are fully integrated with the driving units [47]. Furthermore, adjustable forces and stiffness are obtained at the cost of high power consumption. The reaction wheel with 5-DoF AMBs described in [105] consumed 560 W for the levitation while the total mass of the whole system was only 4 kg. To reduce the power consumption, a possible solution is employing PMs to provide base flux [108].

2.3.2. BALL BEARINGS

Ball bearings use rolling elements to support the rotor and to minimize rotational frictions. Advantages of ball bearings are the high robustness and low cost. Although the maximum speed is limited by friction and temperature, speeds of 100,000 rpm have been achieved by special ball bearings [109]. Additionally, since ball transfer bearings do not interfere with the driving unit, they have been employed in many spherical actuators, including ultrasonic-based[81], induction-based [30], PM-based [46, 48, 49] and reluctance-based [54, 74] actuators. In the induction motor presented in [30], the ball bearing transfer unit consisted of a rolling ball encapsulated in a hemispherical cup. The cup end was screwed onto the stator. The rolling ball supported the rotor's omnidirectional rotations.

The rolling friction generated by ball bearings is generally lower than sliding friction. However, because the friction acts on the rotor's surface, its force arm cannot be neglected. The frictional torque results in reduced efficiency [110]. Besides, achieving a total mechanical balance of the reaction sphere supported by ball bearings is challenging. When performing arbitrary-axis rotations, an unbalanced reaction sphere would introduce vibrations [111]. Furthermore, the rotor's surface may deflect or be damaged by large payloads [54, 74]. For spacecraft attitude control, instabilities occurring in ball bearings may cause transient disturbances, impairing the pointing performance of observation satellites [104]. Moreover, lubrication in space is inconvenient. The lifetime of a ball bearing is limited by wear and heating caused by friction.

2.3.3. AERO/HYDROSTATIC BEARINGS

Aero/hydrostatic bearings utilize continuously escaped air or fluid (normally oil) flow to support the rotor. Therefore, clean air or liquid and additional pumps are required.

Aerostatic bearings are commonly referred to as air bearings. In contrast to other contactless bearings, aero/hydrostatic bearings have relatively high stiffness [112]. Moreover, they eliminate structural constraints, allowing the rotor to perform 4π rotations. Without dynamic instabilities occurring in aero/hydrodynamic bearings [107], or wear in mechanical contact bearings, aero/hydrostatic bearings provide stable support irrespective of the rotor's speed. An additional benefit brought by air bearings is the cooling effect [113].

Air bearings minimize frictional effects greatly. In the multi-DoF spherical actuator presented in [46], the rotor was supported by six spherical bearings with air supply. The spherical bearing produced a friction torque of 18 mNm. With compressed air supply, the friction torque was reduced to 2 mNm. Compared with air, oil has higher viscosity and large friction but provides enhanced damping and stiffness [22, 113]. Nevertheless, the drawback of aero/hydrostatic bearings is that the continuous air or liquid supply complicates the bearing system. Especially, the seal of the bearing would be a problem when they are applied to space missions. In ground tests of reaction spheres, air bearings are commonly employed to eliminate friction or to decouple interference brought by electromagnetic bearings [14, 15].

2.3.4. OTHER TYPES OF BEARINGS

ELECTROSTATIC BEARINGS

Electrostatic forces levitate charged objects in the electric field. Without friction or lubrication, electrostatic bearings show great potential for applications in space vehicles. Moreover, compared with electromagnetic suspensions, electrostatic bearings are applicable to a wider range of materials such as conductive materials, semiconductors, as well as dielectric materials. Since the magnitude of currents flowing through electrodes is only in the order of sub-microampere, the power consumption is low [114]. According to the evaluation in [89], the electrostatic suspension was the best option for space actuators. In fact, it was adopted in many reaction sphere concepts proposed in the 1960s [55, 56]. However, its major drawback is the required high voltages and strong electric fields. Practically, the maximum attainable force of the electrostatic bearing is limited by the break-down voltage and usually is very weak. For example, the breakdown field strength for air is approximately 3 kV/mm and it means a maximum force density of 40 N/m^2 which results from $w = 0.5\varepsilon E^2$ [115], where w, ε and E denote energy density, permittivity and the electric field strength in the gap, respectively. For a wafer with the mass density of 2.225 g/cm^3 to be suspended in air, the maximum allowable thickness is only 1.834 mm [116]. Therefore, the dimensions and mass of the levitated objects are severely restricted.

In space or vacuum environments, the breakdown field strength increases (Schwinger limit gives the value about 1.3x10^{15} V/mm), but high voltages will be needed to provide the high force density, which renders its application in space difficult.

DIRECT CONTACT

In this approach, the rotor is supported by the stator directly and sliding friction exists. This kind of bearing is commonly used in contact type ultrasonic motors [80, 117], because frictions between the stator and the rotor transfer driving torques. Sometimes, it

is also employed in electromagnetic motors, such as the PM-based actuator proposed in [118], where the rotor was housed within the stator with a low friction surface coating.

Nevertheless, the sliding friction existing between moving parts restricts the rotor's speed [80] and causes wear and heating issues. Furthermore, this kind of bearings has high requirements for the manufacturing tolerance and clearance. Otherwise, the sliding friction may cause undesired effects [110]. For instance, in the 3-DoF actuator prototype presented in [119], due to manufacturing tolerances and imperfect spheres, nonuniformly distributed stick-slip friction torque appeared and was significant.

SPHERICAL JOINTS

Different from ball bearings and direct contacts, where the rotor is supported by the outside surface, spherical joints support the rotor at its center. Although spherical joints still belong to mechanical contacts and there are wear, heating and friction problems, frictions generated by the joint have a very short arm length [110]. However, concerning reaction spheres, the main problem of spherical joints is the structural constraint. The flang stem from the rotor center forbids the rotor's omnidirectional rotations [110, 117, 120, 121]. Furthermore, with the decreased contact area, their rotational stability is also a concern.

SHAFT AND GIMBAL FRAMES

Shafts and gimbal frames are often used in CMGs. Some multi-DoF spherical motors also employed them for their simplicity and reliability. However, the drawback is that they are not compatible with the 4π rotation requirement [40, 122].

AERO/HYDRODYNAMIC BEARINGS

In hydrodynamic bearings, the fluid in the gap between the stator and the rotor forms a lubricant wedge. The bearing's load carrying capability depends on the relative motion. Frictions at high speed are much lower than those at a low speed [107]. Therefore, its performance at the start or stop stages is very poor. Nevertheless, due to the squeeze film damping, this kind of bearing has good damping properties [107]. Except for the dead zone at low speed, fluid bearings also have problems of temperature dependence and are susceptible to radiative erosion. Actually, because of the self-excited instability, the rotational speed range of hydrodynamic bearings is very limited [123].

Aerodynamic bearings are similar to hydrodynamic bearings. Since air has a lower viscosity, it has a smaller frictional resistance than liquids and allows higher rotation speeds [124]. However, aerodynamic bearings provide low stability. Moreover, with similar sizes, they have a much lower load carrying capability than hydrodynamic bearings.

Due to the dynamic instability at high speeds and the poor load-carrying capability at low speeds, no aero/hydrostatic bearing has been utilized in spherical actuators yet. Nevertheless, with the growing interest in applying multi-DoF spherical actuators to robot joints, modeling of spherical hydrodynamic bearings has received more and more attention in recent years [125, 126].

ACOUSTIC BEARINGS

Acoustic levitation is often used in non-contact ultrasonic-based machines. They utilize liquid or air as the medium, transferring acoustic pressure to support the rotor. For instance, this kind of levitation was employed in the spherical ultrasonic motors presented

in [87, 127]. Concerning electromagnetic motors, acoustic bearings do not induce electromagnetic interference and would not couple with driving torque generations. However, the drawback is that the bearing must be sealed when it is employed in spacecraft.

TUNED LC CIRCUIT BEARINGS

Another type of magnetic bearing with feedback is called tuned LC circuit bearing [93]. This kind of bearing is passively stable since displacements are sensed by the circuit itself and input currents are adjusted automatically. Its working principle is explained in [111]. Contact-less support and centering of the reaction sphere were ensured by the automatic currents regulation in three pairs of centering windings. These windings were energized with AC at a certain frequency. They were connected with capacitors, forming LC circuits operating near their resonance. Once the rotor deviated from its centering position, the inductance of the winding circuits changed. The winding circuit with an increasing air gap would approach its resonance. The resultant increased input current would generate larger attractive forces. Correspondingly, currents in the winding circuit with a decreased air gap would reduce and result in a reduced attractive force. The rotor would be pulled back to its original position by the total force. This bearing type does not show damping [93]. Therefore it has been more or less abandoned by researchers and designers.

2.3.5. SUMMARY OF BEARINGS FOR SPHERICAL ACTUATORS

In Table 2.2, bearings commonly used in multi-DoF actuators are listed and compared. In theory, acoustic bearings, tuned LC circuit bearings, aero/hydrodynamic bearings, as well as magnetic levitations caused by diamagnetic and superconductive properties, Levitrons and ferrofluids are also possible for multi-DoF spherical actuators. Since there are no existing applications yet, these bearings are not included in the table.

2.4. DISCUSSIONS ON THE IMPLEMENTATION OF 4π ROTATIONS

Multi-DoF spherical actuators driven by different mechanisms have been presented in section 2.2. For each driving method, there is a wide variety of configurations. Consequently, their control strategies determined by the specific magnetic arrangement are different. Here, irrespective of the torque generation, the ways to integrate multi-DoF rotations into a single actuator are grouped into two principle approaches: through linear stator segments or distributed poles. Their difference is that multiple distributed poles have to be energized together to generate torques while a single linear stator segment can be energized separately to generate driving torques about a specific axis.

2.4.1. LINEAR STATOR SEGMENTS

The first approach is based on the combination of linear stators. The linear stator could be a complete winding set or an inductor. It generates torques about a specific direction. For instance, the inductor employed in [30] excited thrust forces along its longitudinal direction. Hence, in this approach, the rotation about each principal axis is implemented with independent stator segments. To output torques about any desired directions, at least three stator segments are needed and some of them shall be activated simultaneously [128].

Table 2.2: Common bearings of multi-DoF spherical actuators

Types	Feature	Advantages	Weaknesses
Electrodynamic bearings	induced eddy currents	+ contactless support + easy integration with induction motors + passively stable	- power consumption - heating - poor damping - low stiffness
AMBs	active feedback control	+ contactless support + adjustable force and stiffness + precise position control	- power consumption
Ball bearings	rolling friction	+ robust + low cost	- lubrication - damage by large payloads
Aero/hydrostatic bearings	continuous air /fluid flow	+ contactless support + high stiffness + cooling effect	- equipments and resources - seal
Electrostatic bearings	charged objects	+ contactless support +little power consumption	- high voltages
Direct contact	sliding friction	+ simple structure	- wear - heating - strict tolerance requirement
Spherical joints	support at the rotor′s center	+ short arm length of frictional forces	- forbid free rotations - poor stability
Shaft and gimbal frames	mechanical stuctures	+ simplicity + reliability	- forbid free rotations

This method is preferred by actuators without fixed rotor poles, such as piezo/ultrasonic-based, induction-based, and hysteresis-based actuators. For rotors with fixed poles, the fixed poles keep changing their orientations with respect to each stator segment during 4π rotations. As a result, the torque excited by each stator segment depends on the rotor's transient orientation. Hence, almost all PM or reluctance-based actuators are stepping-based.

The integration approach of employing multiple linear stator segments is simple and straightforward in theory. Nevertheless, there are several issues to concern:

1. The first issue is the balance between the torque generation capability and electromagnetic couplings. For a spherical induction motor actuated by linear segments, the driving torque is related to the coverage area of the segments [129]. Increasing the number of stator segments or extending each one's coverage area helps to improve the output torque generation capability, however, enhances electromagnetic couplings between windings. When one stator segment is energized, it would induce voltages in windings on another stator segment and results in disturbance torques.

2. When the rotor performs 4π rotations, its movement is not always aligned with the

traveling direction of excited magnetic fields. For instance, if the stator segment driving rotations about the x-axis is energized while the rotor is rotating about the y-axis, the generated driving torque about the x-axis will be affected and could be different from expectation. Additionally, a resistance torque about the y-axis will be generated.

2.4.2. DISTRIBUTED POLES

An alternative is to utilize interactions between distributed rotor poles and stator poles. Its configuration is more versatile and is applicable to all electromagnetic driving units and even piezo/ultrasonic-based driving units, although specific implementations could be different. For cases where traveling waves are required, such as induction or hysteresis-based actuators, or the spherical ultrasonic motor presented in [82], several stator poles are controlled cooperatively to form a rotary field. Hence, this configuration does not show a distinct advantage for induction or hysteresis-based actuators. Besides, as explained in section 2.2.2, to obtain a decent output torque, induction or hysteresis motors with distributed stator poles usually has a huge dimensional ratio between the stator and the rotor.

Advantages of distributed stator poles become obvious when they are applied to actuators with determined poles on the rotor, such as PM or reluctance-based actuators. Since interactions between rotor poles and the active stator electromagnet depend on the rotor orientation, the generated force could be along any direction in 4π space. Independent activation of stator electromagnets gives great flexibility in the control of resultant torques or forces.

This excitation method is versatile but its drawbacks lay in two aspects.

1. Firstly, the number and arrangements of rotor and stator poles shall be designed elaborately to avoid locking or uncontrolled motions. In theory, fixed poles are not required to be placed evenly on the sphere. However, evenly distributed poles and coils provide the advantage of a symmetric magnetic field and facilitate the rotor's motion control [54].

2. Secondly, robust and flexible control comes at the price of complexity. Since generated torques and forces depend on the rotor's transient orientation, the orientation measurement or estimation is necessary. Besides, since the number of output (torques and forces) DoFs is usually lower than the number of input (currents of coils) DoFs, solving the underdetermined problem and finding the most effective solution is challenging [113]. Furthermore, involving a large number of coils, sensors and constrained by the controller's processing capability, the entire system's control bandwidth is limited [2].

2.5. SUMMARY

This chapter provides an extensive investigation into the excitation and support methods of reaction spheres. It is shown that developments of the driving unit and bearings, as well as their integration, remain great challenges. Although some prototypes based on induction, PM or piezo/ultrasonic motors have performed rotations about arbitrary

axes, massive improvements are still necessary to allow practical applications. Improving driving efficiency and minimizing negative impacts brought by bearings are important.

In chapter 3, a reaction sphere suitable for microsatellites attitude control will be designed. Its driving unit and bearing will be selected from candidates surveyed in this chapter through AHP.

3

DESIGN ASPECTS OF REACTION SPHERES

3.1. INTRODUCTION AND REQUIREMENTS

In chapter 2, an extensive review of possible driving and supporting mechanisms of a freely rotating sphere is presented. Based on that, a reaction sphere design will be proposed to facilitate in-depth studies. Initially, the motivation of developing reaction spheres is to reduce the number of required actuators for attitude control of small spacecraft which have very limited mass, volume and power budget. However, since the TRL of reaction spheres is low, the research presented here will focus on the functional analysis and leave the improvement of performances as future work. Here, the reaction sphere is designed for applications on microsatellites (mass < 100 kg).

To guide the design of the reaction sphere, characteristics of three commercial reaction wheels (i.e., Dynacon Micro Wheel 200[1], 10SP-M[2] and RW90[3]) flying on microsatellites with the mass ranging from 50 - 100 kg are listed in Table 3.1.

Considering general working environments of microsatellites, two operational requirements are posed to the designed reaction sphere:

- O1 The reaction sphere shall be able to withstand the launch loads.
- O2 The reaction sphere shall be able to withstand the temperature range of -20°C to $+50^{\circ}$ C for at least two years.

Typically, the mass of a microsatellite is within 10∼100kg. As per the mass distribution within a spacecraft, ADCS contributes 8% of the whole satellite [1]. Therefore, the ADCS's mass ranges from 0.8 - 8 kg. Assuming only a single reaction sphere is employed

[1] http://microsat.sm.bmstu.ru/e-library/Algorithms/Hardware/wheels/productpdf_6.pdf
[2] https://www.sstl.co.uk/getattachment/f31aaa67-3750-4a8a-9742-c1cd800c0a5b/Microwheels-Reaction-Wheel
[3] http://www.astrofein.com/2728/dwnld/admin/Datenblatt_RW90.pdf

Table 3.1: Characteristics of commercial reaction wheels flying on microsatellites

Alternatives	Dynacon Micro Wheel 200	10SP-M	Reaction wheel RW 90
Flight experiences	MOST (53 kg) FEDSAT (58 kg) CHIPSAT (64 kg)	UK-DMC-2 (96 kg) Deimos-1 (88 kg) ExactView-1 (100 kg)	BIRD(94 kg)
Mass	0.77∼0.93 kg (configurable)	0.96 kg	≤ 0.9 kg
Size	102 × 94 × 89 mm	ϕ109 × 101 mm	103 × 101 × 80 mm
Temperature range	−20°C to +60°C	−20°C to +50°C	−20°C to +50°C
Speed range	± 10000 rpm	± 5000 rpm	± 7800 rpm
Angular momentum capability	0.05∼0.18 Nms (configurable)	0.42 Nms	0.34 Nms
Torque capability	20 mNm	11 mNm	15 mNm
Speed control resolution	0.2 rpm	<0.1 rpm	< 1 rpm [130]
Power consumption	5000 RPM: < 2.1 W 9000 RPM: < 3.2 W	∼ 2.8 W (nom) ∼10 W (max)	< 3.5 W (nom) < 15 W (max)

on-board and it will be a major component of ADCS (assuming 65%), the mass of the reaction sphere will be about 0.5 - 5 kg. Here, the mass limit for the reaction sphere is set as 3 kg, which means the designed product would be suitable for microsatellites with a mass of about 60 kg. Meanwhile, the volume requirement is estimated by referring dimensions of reaction wheels used on microsatellites with a mass about 50∼100 kg, such as CHIPSat, BIRD and Tsinghua-1. Since a single reaction sphere replaces a set of three wheels, the following constraint requirements are derived:

- C1 The reaction sphere's total mass (including electronics) shall be less than 3 kg.
- C2 The reaction sphere's total dimensions (including electronics) shall be less than 300 mm× 100 mm× 100 mm.

Since performance improvements are left as future work, requirements of the reaction sphere's power consumption remain open during the design.

Regarding expected performances, a rough order of magnitude is considered rather than specific requirements. This is because the TRL of reaction spheres is low and far from practical applications. Following requirements are set by referring performances of reaction wheels listed in Table 3.1.

- P1 The reaction sphere shall be able to perform 4π rotations.
- P2 The maximum control torque about the spin axis shall be no less than 15 mNm.
- P3 The spin rate varies within ±8,000 rpm.

- P4 Resolution for speed control shall be less than 1 rpm.

The designed reaction sphere will be speed controlled rather than torque controlled. This is because, in the speed control loop, internal disturbances such as frictional torques generated by ball bearings can be counteracted.

Since the mass and the maximum velocity of the reaction sphere have been required, there is no need to set an extra requirement for its angular momentum storage capability. With the same mass or the same volume, a cylinder could provide a larger moment inertia than a sphere, due to the mass distribution. Therefore, if the maximum spinning velocities are the same, reaction spheres do not show advantages over reaction wheels regarding the momentum storage capability. The main benefit of a reaction sphere is its re-configurable rotation axis.

The primary objective of this study is functionality analysis. To simplify the prototyping and to mitigate the risk of rotor unbalance, the rotor is designed to be a solid sphere. Optimization of the moment inertia with a hollow sphere is future work.

3.2. SELECTION STRATEGY

The selection of the most suitable driving unit and bearing is carried out through AHP [33]. It is done with the help of AHP-TOv2.8 tool. The first step of AHP is to decompose the problem into a hierarchy of criteria which affect the final decision. Pairwise comparisons between criteria concerning their importance result in numerical weight factors for each criterion. Then, for each criterion, pairwise comparisons between options generate a numerical score for every option. This score is local, representing the candidate's possibility to meet this criterion. For each candidate, the total score is obtained by summing products of local scores and their corresponding criterion's weight factors. The total score of a candidate represents its possibility to be the most suitable solution for the decision-making problem.

3.2.1. DRIVING UNIT

Before the trade-off, the five types of driving units listed in section 2.1 are re-evaluated. To enable 4π rotations, driving units based on PMs or reluctance shall have evenly distributed poles on the rotor. Compared to the reluctance-based candidate, the PM-based driving unit is distinctly superior. Advantages that are offered by reluctance-based spherical driving units rather than PM-based spherical driving units are analyzed below:

- Due to the absence of PMs, the financial cost of a reluctance-based driving unit is much lower. However, since this project focuses on functionality, the financial cost is not considered as a criterion.
- In a reluctance-based driving unit, the rotor with evenly distributed salients can be made of a single piece of ferromagnetic material. In this way, its mechanical strength is larger than that of a PM-based driving unit. However, compared to induction or piezo/ultrasonic-based driving units where the rotor has a simple structure, reluctance-based driving units do not seem superior.

Therefore, based on these considerations, the reluctance-based driving unit is excluded

from further trade-off. Similarly, by comparing the strengths and weaknesses of induction motors and hysteresis motors, the hysteresis-based driving unit is discarded.

For the remaining three candidates, i.e., driving units based on PM, induction and piezo/ultrasonic, six criteria are employed in the trade-off (see Fig. 3.1). Since each type of driving unit could have different designs and these design options may affect the comparison greatly, only typical designs of each candidate are considered:

- The PM-based driving unit has evenly distributed PMs on the rotor surface. Multiple electromagnets are evenly placed around the rotor. To avoid strong cogging torques, the stator electromagnets are air-cored.
- In the induction-based driving unit, the rotor is composed of a ferromagnetic core and an external conductive layer. To minimize the total size, the rotor is driven by multiple linear stator segments.
- There are no additional restrictions to the design of piezo/ultrasonic-based driving units.

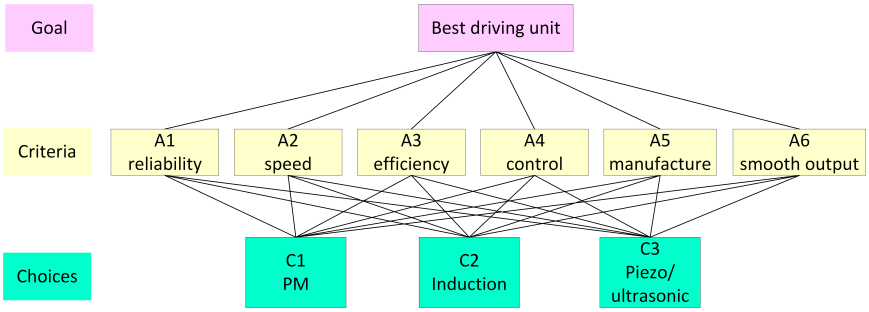

Figure 3.1: Hierarchy of the driving unit selection problem.

In order of importance, the first criterion is reliability. Mechanical and functional failures of the driving unit are concerned. In PM-based spherical driving units, brittle PMs are attached to the rotor and restrict the rotor's mechanical strength. Additionally, the remanence of PMs might change if the operating temperature is too high and results in control errors.

A high maximum velocity is important because it determines the momentum storage capability of the reaction sphere. As presented in section 2.2, the achievable maximum speed of piezo/ultrasonic-based driving units is far behind that of electromagnetic-based driving units.

The third criterion is efficiency. Because of the limited power budget onboard spacecraft, a driving unit with high efficiency is preferred. Since electromagnets in PM-based spherical driving units will be energized with DC, the efficiency of conventional Brushless direct current (BLDC) motors is used for reference. The typical efficiency of BLDC is about 70%$\sim$ 95% and a smaller motor has a lower efficiency [131]. Conventional induction motors have an efficiency between 60% (smaller size) and 90% (larger size) [131].

Considering the size of the reaction sphere and the degraded performances by modifying a conventional motor to a spherical driving unit, the expected efficiencies for PM-based and induction-based driving units are 70% and 60%, respectively. In contrast, the efficiency of traveling wave ultrasonic motor is merely 30% [85].

The fourth criterion is controllability. Due to the measurement of transient rotor orientation and switching of multiple electromagnets, the control of PM-based spherical driving units is tougher than that of the other two candidates.

The fifth criterion is manufacturability. Since great flexibility is allowed in the construction of the stator while the rotor structure is kind of certain, this criterion concerns the difficulty of manufacturing the rotor. As presented in section 2.2, the rotor of a piezo/ultrasonic motor can be made of a single piece of material. In induction-based driving units, to enhance the magnetic flux density within the actuator, the rotor is composed of a ferromagnetic core and an external conductive layer which is usually assembled by two hollow hemispheres. This structure requires strict machining tolerances and assembly tolerances. In a PM-based spherical actuator, the rotor will be attached with multiple PM poles. To obtain a rotor with balanced mass distribution and a smooth spherical surface, the difficulty of manufacturing a PM-based driving unit is highest while that of a piezo/ultrasonic-based actuator is the lowest among the three candidates.

The last criterion concerns the smooth torque generation. Since air-core coils are employed, no cogging torques are involved in the PM-based driving unit. However, in induction-based or piezo/ultrasonic-based driving units, couplings exist in the generation of torques about different axes and excite unwanted eddy currents or friction, resulting in disturbance torques.

Table 3.2: Local and global priorities of each driving unit

	A1 (0.32)	A2 (0.21)	A3 (0.18)	A4 (0.12)	A5 (0.09)	A6 (0.07)	Global score
PM	0.19	0.47	0.42	0.16	0.19	0.52	0.31
Induction	0.47	0.47	0.38	0.42	0.31	0.24	0.42
Piezo/ultrasonic	0.34	0.05	0.2	0.42	0.51	0.24	0.27

Table 3.2 presents the local and global scores of each candidate. The induction-based driving unit is the best option.

3.2.2. BEARING

Before the trade-off, the eight types of bearings listed in 2.2 are re-evaluated.

- To enable 4π rotations, spherical joints, shaft and gimbal frames are discarded.
- Because the driving unit of the reaction sphere will be induction-based, eddy currents circulate in the conductive rotor during rotations, the electrostatic suspension becomes infeasible in this case.

- Since additional mass typically increases the launch cost greatly, air bearings are preferred to hydrostatic bearings. So hydrostatic bearings are excluded from the trade-off.
- In piezo/ultrasonic-based driving units, direct contact between the rotor and the stator transfers frictional torques and excites rotations. However, since the driving unit of the reaction sphere is induction-based, friction between the rotor and the stator is expected to be small. Compared to ball bearings, direct contact requires strict manufacturing and assembly tolerances and does not show extra benefits. Besides, direct contact forbids the mounting of emergency bearings. During the launch phase, the smooth support surface might be affected or even destroyed by the rotor's vibrations. Therefore, direct contact bearings are excluded from comparisons.
- Since lubrication is inconvenient in space, ball bearings here refer to ceramic (silicon nitride) bearings which require no grease lubrication.
- To prevent damages caused by vibrations during the launch phase or touch down at high speeds, an emergency ball bearing is required in contact-less bearings (i.e., electrodynamic bearings, AMBs and air bearings).

For the remaining four candidates, i.e., electrodynamic bearings, AMBs, ball bearings and air bearings, six criteria are employed in the trade-off (see Fig. 3.2). Since all these candidate bearings have speed limits (>2,000,000 rpm [132]) much higher than the expected maximum speed of the reaction sphere (8,000 rpm) and have load-carrying capabilities [133] larger than the weight of the rotor, speed limit and load-carrying capability are not considered as criteria.

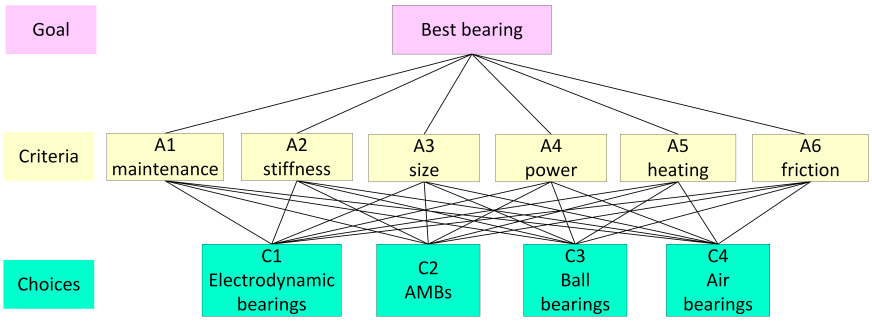

Figure 3.2: Hierarchy of the bearing selection problem.

In order of importance, the first criterion concerns the risk of maintenance. Except for the case of electronics failures, electrodynamic bearings and AMBs need no maintenance. Compared to general steel bearings, ceramic bearings produce little friction and have a prolonged lubricant life. Therefore, the risk of requiring lubrication within two years is low. Regarding air bearings, their performance is greatly affected by the air cleanliness which shall be monitored regularly. Considering possible contamination

from emergency bearings, an inspection of the air supply system is likely required within the designed lifetime.

Stiffness is the second criterion. The stiffness of ceramic bearings depends on the rotating speed and the preload. At the designed speed range with a light preload, the radial stiffness of ceramic ball bearings is about 100 $N/\mu m$ [134]. The stiffness of air bearings depends on the size of the bearing. Larger air bearings have a higher stiffness. Usually, the stiffness of small air bearings can easily achieve 100 $N/\mu m$. Ideally, the stiffness of electromagnetic bearings depends on the control system and can be infinite in theory. The stiffness of active magnetic bearings employed in the reaction sphere presented in [135] was about 500 $N/\mu m$. Since input currents of electrodynamic bearings are restricted by the thermal limit, their stiffness is much lower than that of active magnetic bearings and seldom achieves the range of 1 $N/\mu m$ [136–138].

The third criterion is size. According to [132], magnetic bearings take 2∼10 times the space of ball bearings. Here, the ratio is assumed 5. Since the driving unit of the reaction sphere is induction-based, driving windings can be used for electrodynamic bearings at the same time. Taking the emergency bearing into account, the size of the electrodynamic bearing is almost the same as ball bearings. Due to the external pump, air bearings take much more volume than the other candidates.

The fourth criterion concerns power consumption. Air bearings consume little power for electronics while electromagnetic bearings consume a lot. Concerning small actuators, to achieve the same stiffness, the power consumption of electrodynamic bearings is much larger than that of AMBs. This is because PMs or magnetized steels provide the magnetic field in AMBs and stator currents are only used for force generation. However, in electrodynamic bearings, both the field and the force are generated by stator currents.

Heating is the fifth criterion and it concerns the thermal performance. Because of the smooth finish, ceramic ball bearings generate little friction and heat. Besides, silicon nitride is tolerant to high temperatures [139]. Regarding air bearings, the cooling effect far outweighs its viscous heating. Electromagnetic bearings produce a large amount of heat through copper loss on stator coils. In small actuators, since AMBs utilize PMs or magnetized steels on the rotor to build the magnetic field, the turn number or input current, and corresponding copper loss are reduced, compared to those of electrodynamic bearings. Additionally, because of the separate driving and bearing windings in AMBs, its heat dissipation capability is increased. In electrodynamic bearings, driving torques are generated by rotor eddy currents while the heat generated by the copper loss on the rotor is mainly dissipated through radiation in space. Therefore, electrodynamic bearings have a worse thermal performance than other candidates.

Among the four candidates, only ball bearings generate friction and lead to disturbances in output torques. Nevertheless, the friction caused by ceramic ball bearings is very small.

Table 3.3 presents the local and global scores of each candidate. Since there are no distinct advantages of AMBs over ceramic ball bearings, further study will consider both of them.

Table 3.3: Local and global priorities of each type of bearing

	A1 (0.33)	A2 (0.22)	A3 (0.17)	A4 (0.13)	A5 (0.08)	A6 (0.07)	Global score
Electrodynamic bearings	0.34	0.03	0.43	0.04	0.05	0.29	0.22
AMBs	0.34	0.61	0.11	0.06	0.08	0.29	0.3
Ball bearings	0.24	0.18	0.43	0.5	0.26	0.13	0.28
Air bearings	0.09	0.18	0.04	0.39	0.6	0.29	0.20

3.3. INDUCTION-BASED REACTION SPHERES WITH AMBS

Based on the trade-off results presented in subsections 3.2.1 and 3.2.2, an induction-based reaction sphere with AMBs will be proposed. To maximize the performances of induction-based rotations, the rotor is made of a ferromagnetic core with an external copper layer. Driving windings cover the rotor circumference with the pole-pair number of one. In this design, AMBs can be implemented in two ways.

In the first way, the ferromagnetic core of the rotor is magnetized and attracted by stator electromagnets [13, 59]. The attractive force's direction depends on the orientation of the energized electromagnet, which is fixed. However, the reaction sphere is designed to perform 4π rotations. When the direction of the suspension force is not aligned with the rotor's spin axis, performances of the induction-based rotation will deteriorate seriously since suspension electromagnets introduce an additional resistant torque. Therefore, this way is discarded in the further design.

In the second way, PMs are placed on the rotor surface. Depending on their relative orientations, PMs and energized DC electromagnets interact and generate suspension forces or driving torques. Since PMs provide bias flux, dimensions and the power consumption of DC electromagnets can be reduced greatly. Therefore, this approach is adopted in the reaction sphere design.

To minimize the influences of AMBs on the induction-based rotation, the rotor structure is specially designed. As illustrated in Fig. 3.3, a pair of PMs is placed on the rotor surface. Normally, rotations of the reaction sphere are about the axis of symmetry and are driven by induced eddy currents. Interactions between PMs and activated DC electromagnets provide contactless support to the rotor. Additionally, the spin axis of the rotor inclines when specific DC electromagnets are energized. To mitigate the coupling between electromagnetic induction and PMs, the PMs are mounted with like-poles outward pointing.

To ensure that the rotor's orientation, speed, and position are always under control, three sets of windings are placed on the stator orthogonally (not all involved coils are illustrated in Fig. 3.3). Each set is arranged about a principal axis, consisting of three pairs of driving coils and six pairs of bearing coils. To reduce the axial length, stator windings are wound toroidally around the stator back iron. One set of driving windings is placed about the z-axis, as illustrated in Fig. 3.4. The arrangement of driving windings is similar to that of a 3-phase AC machine. Bearing coils are placed co-axially with the driving

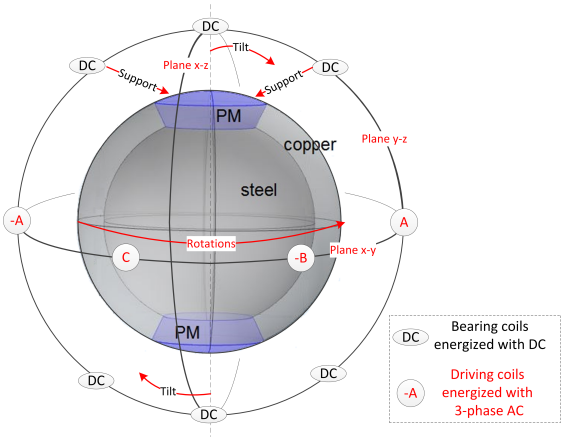

Figure 3.3: Working principle of the proposed reaction sphere.

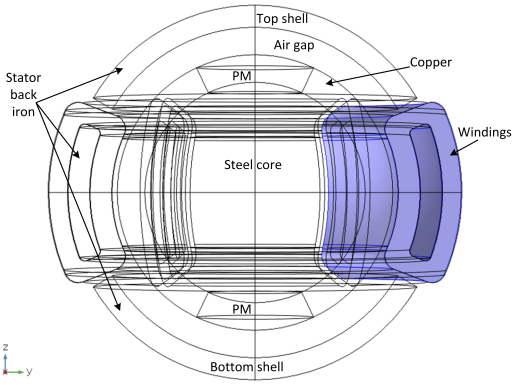

Figure 3.4: The numerical model with one driving coil highlighted.

coils and they are controlled in pairs to drive tilts or translational displacements. Fig. 3.5 shows how windings about three principal axes are wound and assembled together. For clarity, one piece of the stator segment is removed in the figure. Please note that slots on the inner surface of the stator back iron do not physically exist. They are drawn here to illustrate the direction of stator currents carried by wires. At the joint of two winding sets, windings overlap and are wound around the same stator iron segment. It is important to note that the dimensional ratio between driving coils and bearing coils in Fig. 3.5 does not indicate the real ratio. Besides, to facilitate the feasibility study, effects caused by breaks in the stator back iron are neglected in the conceptual design. Although the employed toroidal coils [140, 141] shorten the axial length of stator windings, the electrical conductor length is not reduced. Consequently, the stator resistance and copper loss on stator windings are not decreased.

Fig. 3.6 shows the magnetic suspension and orientation control loops when the sym-

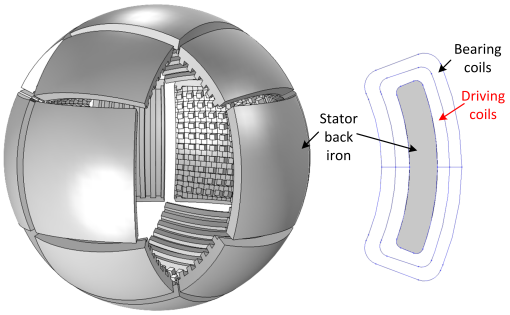

Figure 3.5: The conceptual design of the assembled stator back iron where driving coils and bearing coils are wound around.

metry axis is along the z-axis. Energizing one pair of bearing coils (oppositely placed) with opposite DC inputs results in a translational force. Therefore, with at least three pairs of bearing coils interacting with the PMs, translational displacements of the rotor can be controlled. When the pair of bearing coils are provided with the same DC input current, electromagnetic torques are generated. For orientation control, several bearing coils will be activated subsequently. Actually, detailed control of bearing coils depends on the rotor orientation and torque/force calculations are complicated. Although tilt through the 4π range is allowed by the design, the bearing control efficiency is not isotropic. It depends on the relative orientation of the rotor with respect to energized bearing coils. In operations, the transient rotor orientation will be estimated through mounted 2D Hall sensors. Sensors are inserted into the reaction sphere through gaps between stator segments (see Fig. 3.5).

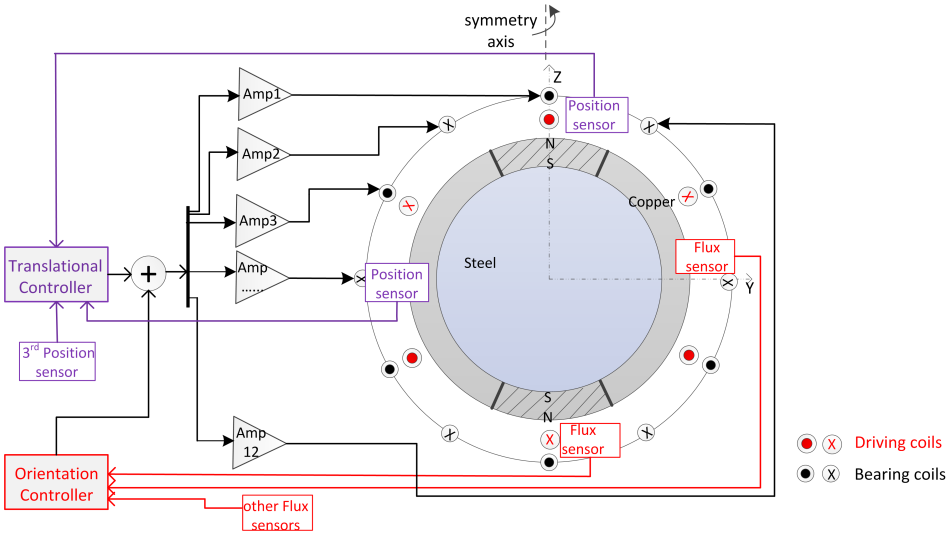

Figure 3.6: Position and orientation control of the rotor.

When the symmetry axis is along one of the principal axes (the x, y, or z axis), rotations excited by the electromagnetic induction are the same as conventional asynchronous machines. If the symmetry axis deviates from these principle axes through orientation control, rotations about the symmetry axis will be realized by energizing more than one set of AC windings.

3.4. INDUCTION-BASED REACTION SPHERES WITH BALL BEARINGS

Considering the risk that AMBs introduce disturbances to the induction-based rotation, an induction-based reaction sphere with ball bearings is proposed as an alternative. Employing ball bearings greatly simplifies the rotor structure. It is made of a ferromagnetic core with an external copper layer. To enable 4π rotations, three sets of stator windings are employed and their arrangements are the same as those of the driving windings presented in Fig. 3.5. Breaks in the stator back iron are not considered in the feasibility study. The rotor is supported by direct contact with eight ball plungers which are placed at gaps of stator windings.

3.5. SUMMARY

In this chapter, an innovative reaction sphere design is proposed. Its design requirements are derived based on the application to attitude control for microsatellites. Its driving unit and bearings are selected from possible candidates through AHP. It is shown that the induction-based driving unit is the most promising driving method in space applications. Although its efficiency is lower than that of PM-based driving units, it has higher reliability and relatively easier control in the space. Considering bearings, both AMBs and ball bearings will be investigated as they are the top two choices in the selection. Based on the trade-off results, an induction-based reaction sphere with AMBs and another design with ball bearings are presented and an extensive study will be conducted.

4

MAGNETIC FIELD MODEL

4.1. INTRODUCTION

In chapter 3, possible driving units are compared at a general level where their advantages and disadvantages are described qualitatively. Through AHP, the induction-based driving unit is selected as the most promising candidate for applications to the attitude control of spacecraft. In this chapter, to conduct deeper studies and to facilitate dynamics modeling, magnetic fields excited within the reaction sphere are modeled. Based on the modeled distribution of magnetic flux density $\vec{B}$, electromagnetic forces and torques acting on the rotor can be calculated fast and accurately. In contrast to numerical analysis, analytical analysis offers a deep insight into the mechanism. Especially for 3-dimensional problems, a numerical simulation may take hours while the analytical model will give a result within minutes.

The essence of analytical magnetic field modeling is solving Maxwell's equations. Generally, the quasi-static approximation can be applied to the electromagnetic fields of electric machines [143]. It assumes that capacitive effects in the machine are negligible, which in turn simplifies Maxwell's equations. A basic way to model magnetic fields is to calculate and integrate the magnetic flux density produced by each charge or each small segment of currents. However, boundary conditions are not considered in this method [144]. In real machines, boundaries exist and the magnetic field is affected by PMs, changing electric fields and magnetized ferrimagnets. In special cases, boundaries can be removed via the image method [145]. Nevertheless, it is not always possible. A more general approach is introducing variables, e.g. magnetic potentials, transforming Maxwell's equations to Laplace's or Poisson's equations for separated regions. Unknowns in the general solutions can be solved by boundary conditions.

Since the reaction sphere is designed to perform 4π rotations, modeling the magnetic field is a 3-dimensional problem. Fortunately, the spherical geometry facilitates the analysis in a spherical frame, where the general solution to Laplace's equations is

The content of this chapter has been published in IEEE Transactions on Magnetics **54**, 1 (2018) [142].

known. Therefore, the approach of transforming Maxwell's equations to Laplace's /Poisson's equations is adopted.

4.2. MODELING OF MAGNETIC FIELDS OF REACTION SPHERES

Field modeling of the reaction sphere is based on the following assumptions:

1. The stator back iron is slot-less, without openings;
2. No eddy currents in the stator back iron;
3. Input stator currents are sinusoidal;
4. High order space harmonics caused by non-sinusoidal winding distributions are neglected;
5. The relative permeability of iron is infinite;
6. No iron saturation;
7. Only one set of driving windings is excited at a certain time;
8. End effects are neglected;
9. PMs have a linear demagnetization characteristic and are fully magnetized in the direction of magnetization;
10. The actuator is in a mechanical and electrical steady state;
11. Electromagnetic couplings between stator windings are negligible.

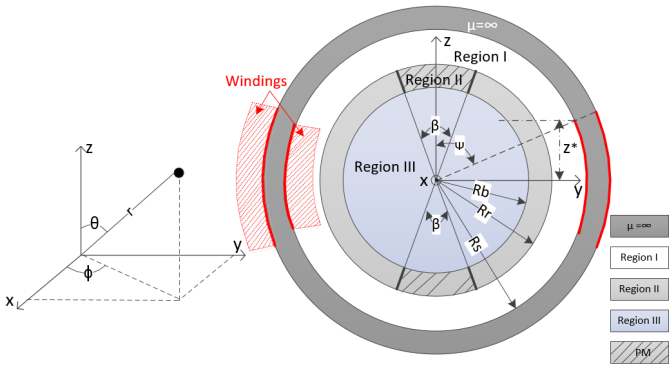

Figure 4.1: Geometry of the reaction sphere.

The simplified geometry of the reaction sphere is shown in Fig. 4.1. The whole actuator is axially symmetric. For convenience, a spherical coordinate frame is employed with its origin at the rotor core. On the rotor, PMs (in grey with the slash) and the copper domain (in grey) form Region II. Region III is the steel core. The air domain (including

Table 4.1: Basic preliminary parameters of the actuator

Parameters	Value	Meaning
R_b	20 mm	Radius of the solid rotor core (steel)
R_r	25 mm	External radius of the copper layer
β	$2 \times 25°$	Cone angle of one PM pole
R_s	30 mm	Inner radius of the stator back iron
ψ	65°	Angular area without stator currents
B_r	0.23 T	Remanence of PMs

stator windings) between the rotor and the stator is referred to as Region I. Stator windings are modeled as surface currents $\vec{J}_f = J_0 \cos(\omega t - \phi)/\sin\theta \cdot \vec{e}_\theta$ which are sinusoidally distributed on the inner surface of the stator shell within the region of $\theta \in [\psi, \pi - \psi]$. ω is the angular frequency of input currents.

The design of the reaction sphere starts with a dimensional ratio of 1:9 between the rotor and the whole actuator (excluding electronics) [34]. As per the size requirement, the external radius of the rotor R_r is determined. Table 4.1 lists the dimensional parameters and basic inputs of the reaction sphere. Many parameters in the table are results of conflicting preferences. For instance, a large space between the stator and the rotor accommodates more winding turns and higher input currents. However, space occupied by the stator windings extends the effective air gap width and weakens the coupling between the rotor and the stator. Therefore, the geometrical parameters listed here are used for the preliminary design only and will be optimized later.

The spherical actuator is designed with a maximum rotational speed of 8000 rpm. For a 1-pole-pair induction machine, the speed of 8000 rpm requires an input frequency of no less than 140 Hz. However, with the nominal phase voltage, if the input frequency is high, the stator and rotor reactance will be high. Consequently, the achievable maximum torque will be low. Besides, an adjustable rotational speed is required for the actuator. Therefore, the reaction sphere will be inverter-fed operated with variable frequencies. Another benefit of the inverter-fed machine is that the rotor always runs at a small slip, which means that high starting currents can be avoided. Here, it is assumed that the actuator will start with an input frequency of 10 Hz.

4.3. ANALYTICAL FIELD MODELS

In the designed reaction sphere, both PMs and AC driving windings are involved. PMs generate a static field while AC driving windings generate a time-harmonic field. To simplify the analysis, the composite magnetic field is separated into three time harmonics: e^{0*t}, $e^{j\omega t}$ and $e^{-j\omega t}$.

4.3.1. STATIC FIELD EXCITED BY PMS

The constitutive equations for Region I, II, and III are as follows:

For Region I, the magnetic property of air (or vacuum in space) is described as

$$\vec{B}_I = \mu_0 \vec{H}_I \,, \tag{4.1}$$

$\vec{H}$ is magnetic field strength and μ_0 is the vacuum permeability.

For Region II, PMs are modeled as [146]

$$\vec{B}_{II} = \mu_0 \mu_m \vec{H}_{II} + \mu_0 \vec{M} \,, \tag{4.2}$$

where μ_m is the relative recoil permeability and $\vec{M} = \vec{B}_r / \mu_0$ is the residual magnetization. For hard ferrites, the typical value of μ_m is 1.03-1.3 [147]. In this study, the value is set to 1.05. On the rotor, there are two pole pairs. Each pair is composed of one PM pole and one consequent pole. The copper area between PMs is assumed to be occupied by unmagnetized PM material ($\vec{M} = \vec{0}$) [148]. Indeed, pure copper is diamagnetic and its relative permeability is 0.999994 [149]. Nevertheless, compared to the relative recoil permeability of 1.05 for PMs, the influence of the approximation is negligible.

For Region III, the magnetic property of steel is described by

$$\vec{B}_{III} = \mu_0 \mu_r \vec{H}_{III} \,. \tag{4.3}$$

The relative permeability μ_r is set to 30 since AISI4340 [150] is employed in the corresponding numerical simulation.

Since the magnetic field generated by PMs is constant, no eddy currents are induced in the conductive domain. To minimize the number of variables and simplify calculations, the scalar magnetic potential Φ is introduced and it is related to $\vec{H}$ by

$$\vec{H} = -\nabla \Phi \,. \tag{4.4}$$

Transforming Maxwell's equations to Laplace's and Poisson's equations, we obtain governing equations for each domain:

$$\nabla^2 \Phi_I = 0 \,, \tag{4.5a}$$

$$\nabla^2 \Phi_{II} = \frac{\nabla \cdot \vec{M}}{\mu_m} \,, \tag{4.5b}$$

$$\nabla^2 \Phi_{III} = 0 \,. \tag{4.5c}$$

These governing equations are solved in spherical coordinates. For Region I and III (i=I, III), the general solution to Laplace's equation is obtained through separation of variables [151]:

$$\Phi_i(r,\theta,\phi) = \sum_{n=0}^{\infty} \sum_{m=-n}^{\infty} [\kappa_{ni}^m \cdot r^n + \xi_{ni}^m \cdot r^{-(n+1)}] Y_n^m(\theta,\phi) \,, \tag{4.6}$$

where $Y_n^m(\theta,\phi)$ is the spherical harmonic function, κ_{ni}^m and ξ_{ni}^m are unknown constants.

Since the actuator geometry is axial symmetric, the magnetic scalar potential is independent on ϕ, which means m=0 in (4.6). Hence, the general solution to Laplace's equation can be simplified:

$$\Phi_i(r,\theta) = \sum_{n=0}^{\infty} [\kappa_{ni} \cdot r^n + \xi_{ni} \cdot r^{-(n+1)}] P_n(\cos\theta) \,, \tag{4.7}$$

where $P_n(\cos\theta)$ is Legendre polynomial.

For Region II, the general solution to the Poisson's equation is obtained by adding a particular solution which is satisfying the excitation item in (4.5b) to (4.7).

It is assumed that PMs are radially magnetized. Therefore, $M_\theta = M_\phi = 0$ and

$$M_r = \begin{cases} M, & \text{if } \theta \in [0, \frac{\beta}{2}] \text{ or} [\pi - \frac{\beta}{2}, \pi] \\ 0, & \text{if } \theta \in [\frac{\beta}{2}, \pi - \frac{\beta}{2}] \end{cases} . \tag{4.8}$$

M_r is a piecewise function of θ and sectionally continuous in $[0, \pi]$. It can be expanded in Fourier-Legendre series [152]

$$M_r(\theta) = \sum_{n=0}^{\infty} C_{rn} P_n(\cos\theta) , \tag{4.9}$$

with the coefficients

$$C_{rn} = \begin{cases} (2n+1) \int_0^{\frac{\beta}{2}} M P_n(\cos\theta) \sin\theta \, \mathrm{d}\theta, & \text{if } n = \text{even}; \\ 0, & \text{if } n = \text{odd}. \end{cases} \tag{4.10}$$

Assume that a particular solution for Region II can be written as

$$\Phi_{II}^p = \sum_{n=0,2,4\cdots}^{\infty} C_1 r P_n(\cos\theta) + \sum_{n=1,3,5\cdots}^{\infty} C_2 r P_n(\cos\theta) \tag{4.11}$$

to meet the Poisson's equation

$$\nabla^2 \Phi_{II}^p = \frac{\nabla \cdot \vec{M}}{\mu_m} .$$

Comparing respective items on both sides results in $C_1 = 2C_{rn} / \left[\mu_m (2 - n^2 - n)\right]$ and $C_2 = 0$.

To solve unknowns in the general solution, the following boundary conditions [153] are applied:

1. Finite field condition at r=0:

$$B_{III,r}|_{r=0} \neq \infty \Rightarrow \xi_{nIII} = 0 . \tag{4.12}$$

2. Continuous radial component of $\vec{B}$ at r=R_b:

$$\begin{aligned} & B_{III,r}|_{r=R_b} = B_{II,r}|_{r=R_b} \\ \Rightarrow \; & \mu_r n \kappa_{nIII} R_b^{2n+1} = \mu_m \left[n \kappa_{nII} R_b^{2n+1} - (n+1) \xi_{nII} \right] + \frac{n(n+1) C_{rn}}{2 - n^2 - n} R_b^{n+2} . \end{aligned} \tag{4.13}$$

3. Continuous radial component of $\vec{B}$ at r=R_r:

$$\begin{aligned} & B_{I,r}|_{r=R_r} = B_{II,r}|_{r=R_r} \\ \Rightarrow \; & n \kappa_{nI} R_r^{2n+1} - (n+1) \xi_{nI} = \mu_m \left[n \kappa_{nII} R_r^{2n+1} - (n+1) \xi_{nII} \right] + \frac{n(n+1) C_{rn}}{2 - n^2 - n} R_r^{n+2} . \end{aligned} \tag{4.14}$$

4. Continuous tangential components of $\vec{H}$ at r=R_b:

$$\begin{aligned} & H_{III,\theta}|_{r=R_b} = H_{II,\theta}|_{r=R_b} \\ \Rightarrow\ & \kappa_{nIII} R_b^{2n+1} = \kappa_{nII} R_b^{2n+1} + \xi_{nII} + \frac{2C_{rn}}{\mu_m(2-n^2-n)} R_b^{n+2} . \end{aligned} \tag{4.15}$$

5. Continuous tangential components of $\vec{H}$ at r=R_r:

$$\begin{aligned} & H_{I,\theta}|_{r=R_r} = H_{II,\theta}|_{r=R_r} \\ \Rightarrow\ & \kappa_{nI} R_r^{2n+1} + \xi_{nI} = \kappa_{nII} R_r^{2n+1} + \xi_{nII} + \frac{2C_{rn}}{\mu_m(2-n^2-n)} R_r^{n+2} . \end{aligned} \tag{4.16}$$

6. $\vec{H} = \vec{0}$ inside the stator shell:

$$H_{I,\theta}|_{r=R_s} = 0 \Rightarrow \kappa_{nI} R_s^{2n+1} + \xi_{nI} = 0 . \tag{4.17}$$

Resultant magnetic flux density distribution within each region is:

- Region I

$$B_{I,r} = -\mu_0 \sum_{n=0,2,4\cdots}^{\infty} \left[n\kappa_{nI} \cdot R_r^{n-1} - (n+1)\xi_{nI} r^{-(n+2)} \right] P_n(\cos\theta) , \tag{4.18a}$$

$$B_{I,\theta} = -\mu_0 \sum_{n=0,2,4\cdots}^{\infty} \left[\kappa_{nI} r^{n-1} + \xi_{nI} r^{-(n+2)} \right] \frac{n}{\sin\theta} \left[\cos\theta P_n(\cos\theta) - P_{n-1}(\cos\theta) \right] . \tag{4.18b}$$

- Region II

$$\begin{aligned} B_{II,r} = & -\mu_0\mu_m \sum_{n=0,2,4\cdots}^{\infty} \left[n\kappa_{nII} r^{n-1} - (n+1)\xi_{nII} r^{-(n+2)} \right] P_n(\cos\theta) \\ & - \mu_0 \sum_{n=0,2,4\cdots}^{\infty} \frac{2C_{rn}}{2-n^2-n} P_n(\cos\theta) + \mu_0 \sum_{n=0,2,4\cdots}^{\infty} C_{rn} P_n(\cos\theta) , \end{aligned} \tag{4.19a}$$

$$\begin{aligned} B_{II,\theta} = & -\mu_0\mu_m \sum_{n=0,2,4\cdots}^{\infty} \left[\kappa_{nII} r^{n-1} + \xi_{nII} r^{-(n+2)} \right] \frac{n}{\sin\theta} \left[\cos\theta P_n(\cos\theta) - P_{n-1}(\cos\theta) \right] \\ & - \mu_0 \sum_{n=0,2,4\cdots}^{\infty} \frac{2C_{rn}}{2-n^2-n} \frac{n}{\sin\theta} \left[\cos\theta P_n(\cos\theta) - P_{n-1}(\cos\theta) \right] . \end{aligned} \tag{4.19b}$$

- Region III

$$B_{III,r} = -\mu_0\mu_r \sum_{n=0,2,4\cdots}^{\infty} n\kappa_{nIII} r^{n-1} P_n(\cos\theta) , \tag{4.20a}$$

$$B_{III\theta} = -\mu_0 \sum_{n=0,2,4\cdots}^{\infty} \kappa_{nIII} \cdot r^{n-1} \frac{n}{\sin\theta} \left[\cos\theta P_n(\cos\theta) - P_{n-1}(\cos\theta) \right] . \tag{4.20b}$$

4.3.2. REVOLVING MAGNETIC FIELD EXCITED BY DRIVING WINDINGS

In this subsection, we focus on the dynamic field with components of $e^{j\omega t}$ and $e^{-j\omega t}$. When the stator winding set is energized with alternating currents, eddy currents are induced in region II and concentrate in the low latitude area covered by the energized stator windings. The polar areas where PMs are placed are with a low flux density excited by stator windings. Even if PMs have the same conductivity (σ) as copper, little eddy currents are induced in the polar areas. Hence, we simplify the modeling by assuming that PMs have the same conductivity as copper and this assumption will not cause significant errors.

The constitutive relation for the three domains are the same as those listed for the static field except that the residual magnetization is absent. Due to the currents, the magnetic vector potential $\vec{A}$ is introduced rather than a scalar potential. Using $\vec{A}$, Maxwell's equations are transformed to Laplace's equations for Region I and III, and the diffusion equation for Region II:

$$\nabla^2 \vec{A}_I = 0\,, \tag{4.21a}$$

$$\nabla^2 \vec{A}_{II} = \mu_0 \mu_m \sigma \frac{\partial \vec{A}_{II}}{\partial t}\,, \tag{4.21b}$$

$$\nabla^2 \vec{A}_{III} = 0\,. \tag{4.21c}$$

Considering $\vec{A}$ is a vector function of r, θ, ϕ, and t, two approaches can be used to solve the governing equations. The first one is to solve the three scalar components of $\vec{A}$ separately and connect them by $\nabla \cdot \vec{A} = 0$. Another alternative is to introduce a second-order potential $\vec{W}$ and change $\nabla^2 \vec{A}$ to $\nabla^2 \vec{W}$ [154] .

To minimize the number of variables, the second approach is adopted. The definition of the second-order magnetic potential is provided in (4.22) [154]:

$$\vec{A} = \nabla \times \vec{G}\,, \tag{4.22a}$$

$$\vec{G} = W\vec{r} + \vec{r} \times \nabla K\,. \tag{4.22b}$$

It is demonstrated in [155] that $K \equiv 0$ for eddy current problems. Therefore, K will be omitted in the following. The second-order potential will be written as $\vec{G} = W\vec{r}$. Based on the derivation in [154] (equation 7.04(3) and (4)), the governing equations with $\vec{A}$ can be converted to

$$\nabla^2 \vec{A} = \nabla \times \left(\vec{r} \nabla^2 W\right)\,, \tag{4.23a}$$

$$\frac{\partial \vec{A}}{\partial t} = \frac{\partial}{\partial t}\left[\nabla \times (\vec{r} W)\right] = \nabla \times \left(\vec{r} \frac{\partial W}{\partial t}\right)\,. \tag{4.23b}$$

To distinguish the second-order potentials for the three domains, subscripts are added.

$$\nabla^2 \vec{A}_I = 0 \;\Rightarrow\; \nabla^2 W_I = 0\,, \tag{4.24a}$$

$$\nabla^2 \vec{A}_{II} = \mu_0 \mu_m \sigma \frac{\partial \vec{A}_{II}}{\partial t} \;\Rightarrow\; \nabla^2 W_{II} = \mu_0 \mu_m \sigma \frac{\partial W_{II}}{\partial t}\,, \tag{4.24b}$$

$$\nabla^2 \vec{A}_{III} = 0 \;\Rightarrow\; \nabla^2 W_{III} = 0\,. \tag{4.24c}$$

The magnetic flux density is formulated as:

$$\vec{B} = \nabla \times \vec{A} = -\vec{r}\nabla^2 W + \nabla W + \nabla(\vec{r} \cdot \nabla W) \,. \tag{4.25}$$

In this study, a revolving magnetic field is generated. If the input currents and the winding distribution are perfectly sinusoidal, the magnetic flux density distribution shall just contain the fundamental component. This means both $\vec{B}$ and W can be expressed as functions of r, θ, and $\cos(\omega t - \phi)$. To facilitate the analysis, the electric and magnetic fields are written in complex form, e.g. $e^{j\omega t}$. In fact, these fields only have the real part. Hence, the $e^{-j\omega t}$ element is additionally introduced to remove the imaginary part through Euler's equation. In the following, the subscript + and - indicates the $e^{j\omega t}$ and $e^{-j\omega t}$ elements, respectively.

- Region I:

$$\begin{aligned} W_I &= W_{I+} + W_{I-} \,, \\ &\begin{cases} \nabla^2 W_{I+} = 0 \\ \nabla^2 W_{I-} = 0 \end{cases} . \end{aligned} \tag{4.26}$$

- Region II:

$$\begin{aligned} W_{II} &= W_{II+} + W_{II-} \,, \\ &\begin{cases} \nabla^2 W_{II+} = \mu_0 \mu_m \sigma \frac{\partial W_{II+}}{\partial t} \\ \nabla^2 W_{II-} = \mu_0 \mu_m \sigma \frac{\partial W_{II+}}{\partial t} \end{cases} . \end{aligned} \tag{4.27}$$

- Region III:

$$\begin{aligned} W_{III} &= W_{III+} + W_{III-} \,, \\ &\begin{cases} \nabla^2 W_{III+} = 0 \\ \nabla^2 W_{III-} = 0 \end{cases} . \end{aligned} \tag{4.28}$$

General solutions to Laplace's equations in spherical coordinates have been provided in the previous section. For Region I and III (i=I, III):

$$W_{i+} = \sum_{n=0}^{\infty} \sum_{m=-n}^{n} \left[A_{ni}^m r^n + B_{ni}^m r^{-(n+1)} \right] Y_n^m(\theta, \phi) e^{j\omega t} \,, \tag{4.29a}$$

$$W_{i-} = \sum_{n=0}^{\infty} \sum_{m=-n}^{n} \left[C_{ni}^m r^n + D_{ni}^m r^{-(n+1)} \right] Y_n^m(\theta, \phi) e^{-j\omega t} \,. \tag{4.29b}$$

For Region II, the diffusion equations will be changed to the modified Helmholtz equations by defining the complex coefficients $a^2 = j\omega\mu_0\mu_m\sigma$ and $b^2 = -j\omega\mu_0\mu_m\sigma$:

$$\nabla^2 W_{II+} = j\omega\mu_0\mu_m\sigma W_{II+} = a^2 W_{II+} \,, \tag{4.30a}$$

$$\nabla^2 W_{II-} = -j\omega\mu_0\mu_m\sigma W_{II-} = b^2 W_{II-} \,. \tag{4.30b}$$

General solutions to modified Helmholtz equations in a spherical frame are [156]:

$$W_{II+} = \sum_{n=0}^{\infty} \sum_{m=-n}^{n} \left[A_{n2}^{m} i_n(ar) + B_{n2}^{m} k_n(ar) \right] Y_n^m(\theta,\phi) e^{j\omega t} , \tag{4.31a}$$

$$W_{II-} = \sum_{n=0}^{\infty} \sum_{m=-n}^{n} \left[C_{n2}^{m} i_n(br) + D_{n2}^{m} k_n(br) \right] Y_n^m(\theta,\phi) e^{-j\omega t} , \tag{4.31b}$$

where $i_n(ar)$ and $k_n(ar)$ are modified spherical Bessel functions.

Unknowns in the general solution are solved through boundary conditions:

1. Finite field condition at r=0:

$$B_{III,r}|_{r=0} \neq \infty \Rightarrow \begin{cases} B_{n3}^{m} = 0 \\ D_{n3}^{m} = 0 \end{cases} . \tag{4.32}$$

2. Continuous radial component of $\vec{B}$ at r=R_b:

$$B_{III,r}|_{r=R_b} = B_{II,r}|_{r=R_b} \Rightarrow$$

$$\begin{aligned} &\sum_{n=0}^{\infty} \sum_{m=-n}^{n} n(n+1) A_{n3}^{m} R_b^{n-1} Y_n^m(\theta,\phi) e^{j\omega t} + \sum_{n=0}^{\infty} \sum_{m=-n}^{n} n(n+1) C_{n3}^{m} R_b^{n-1} Y_n^m(\theta,\phi) e^{-j\omega t} \\ &= \sum_{n=0}^{\infty} \sum_{m=-n}^{n} \left[A_{n2}^{m} i_n(aR_b) + B_{n2}^{m} k_n(aR_b) \right] \frac{n(n+1)}{R_b} Y_n^m(\theta,\phi) e^{j\omega t} \\ &\quad + \sum_{n=0}^{\infty} \sum_{m=-n}^{n} \left[C_{n2}^{m} i_n(bR_b) + D_{n2}^{m} k_n(bR_b) \right] \frac{n(n+1)}{R_b} Y_n^m(\theta,\phi) e^{-j\omega t} . \end{aligned} \tag{4.33}$$

3. Continuous radial component of $\vec{B}$ at r=R_r:

$$B_{I,r}|_{r=R_r} = B_{II,r}|_{r=R_r} \Rightarrow$$

$$\begin{aligned} &\sum_{n=0}^{\infty} \sum_{m=-n}^{n} \left[n(n+1) A_{n1}^{m} R_r^{n-1} + n(n+1) B_{n1}^{m} R_r^{-(n+2)} \right] Y_n^m(\theta,\phi) e^{j\omega t} \\ &\quad + \sum_{n=0}^{\infty} \sum_{m=-n}^{n} \left[n(n+1) C_{n1}^{m} R_r^{n-1} + n(n+1) D_{n1}^{m} R_r^{-(n+2)} \right] Y_n^m(\theta,\phi) e^{-j\omega t} \\ &= \sum_{n=0}^{\infty} \sum_{m=-n}^{n} \left[A_{n2}^{m} i_n(aR_r) + B_{n2}^{m} k_n(aR_r) \right] \frac{n(n+1)}{R_r} Y_n^m(\theta,\phi) e^{j\omega t} \\ &\quad + \sum_{n=0}^{\infty} \sum_{m=-n}^{n} \left[C_{n2}^{m} i_n(bR_r) + D_{n2}^{m} k_n(bR_r) \right] \frac{n(n+1)}{R_r} Y_n^m(\theta,\phi) e^{-j\omega t} . \end{aligned} \tag{4.34}$$

4. Continuous tangential components of $\vec{H}$ at r=R_b:

$$H_{III,\phi}|_{r=R_b} = H_{II,\phi}|_{r=R_b} \Rightarrow$$

$$\begin{aligned}
&\frac{1}{\mu_0\mu_r}\left\{\sum_{n=0}^{\infty}\sum_{m=-n}^{n}(n+1)A_{n3}^{m}R_b^{n-1}\frac{jmY_n^m(\theta,\phi)}{\sin\theta}e^{j\omega t}\right.\\
&\left.+\sum_{n=0}^{\infty}\sum_{m=-n}^{n}(n+1)C_{n3}^{m}R_b^{n-1}\frac{jmY_n^m(\theta,\phi)}{\sin\theta}e^{-j\omega t}\right\}\\
=&\frac{1}{\mu_0\mu_m}\left\{\sum_{n=0}^{\infty}\sum_{m=-n}^{n}\left[A_{n2}^{m}\frac{X_n(aR_b)}{R_b}-B_{n2}^{m}\frac{Y_n(aR_b)}{R_b}\right]\frac{jmY_n^m(\theta,\phi)}{\sin\theta}e^{j\omega t}\right.\\
&\left.+\sum_{n=0}^{\infty}\sum_{m=-n}^{n}\left[C_{n2}^{m}\frac{X_n(bR_b)}{R_b}-D_{n2}^{m}\frac{Y_n(bR_b)}{R_b}\right]\frac{jmY_n^m(\theta,\phi)}{\sin\theta}e^{-j\omega t}\right\},
\end{aligned}\tag{4.35}$$

where $X_n(ar)$ and $Y_n(ar)$ are functions of $i_n(ar)$ and $k_n(ar)$:

$$X_n(ar)=\frac{ar}{2n+1}\left[(n+1)i_{n-1}(ar)+ni_{n+1}(ar)\right],\tag{4.36}$$

$$Y_n(ar)=\frac{ar}{2n+1}\left[(n+1)k_{n-1}(ar)+nk_{n+1}(ar)\right].\tag{4.37}$$

5. Continuous tangential components of $\vec{H}$ at r=R_r:

$$H_{I,\phi}|_{r=R_r}=H_{II,\phi}|_{r=R_r}\Rightarrow$$

$$\begin{aligned}
&\frac{1}{\mu_0}\left\{\sum_{n=0}^{\infty}\sum_{m=-n}^{n}\left[(n+1)A_{n1}^{m}R_r^{n-1}-nB_{n1}^{m}R_r^{-(n+2)}\right]\frac{jmY_n^m(\theta,\phi)}{\sin\theta}e^{j\omega t}\right.\\
&\left.+\sum_{n=0}^{\infty}\sum_{m=-n}^{n}\left[(n+1)C_{n1}^{m}R_r^{n-1}-nD_{n1}^{m}R_r^{-(n+2)}\right]\frac{jmY_n^m(\theta,\phi)}{\sin\theta}e^{-j\omega t}\right\}\\
=&\frac{1}{\mu_0\mu_m}\left\{\sum_{n=0}^{\infty}\sum_{m=-n}^{n}\left[A_{n2}^{m}\frac{X_n(aR_r)}{R_r}-B_{n2}^{m}\frac{Y_n(aR_r)}{R_r}\right]\frac{jmY_n^m(\theta,\phi)}{\sin\theta}e^{j\omega t}\right.\\
&\left.+\sum_{n=0}^{\infty}\sum_{m=-n}^{n}\left[C_{n2}^{m}\frac{X_n(bR_r)}{R_r}-D_{n2}^{m}\frac{Y_n(bR_r)}{R_r}\right]\frac{jmY_n^m(\theta,\phi)}{\sin\theta}e^{-j\omega t}\right\}.
\end{aligned}\tag{4.38}$$

6. At $r=R_s$, the tangential component of $\vec{H}$ is discontinuous due to the surface currents within $\theta\in[\psi,\pi-\psi]$:

$$H_{I,\phi}|_{r=R_s}=\frac{J_0}{\sin\theta}\cos(\omega t-\phi)\Rightarrow$$

$$\begin{aligned}
&\frac{1}{\mu_0}\left\{\sum_{n=0}^{\infty}\sum_{m=-n}^{n}\left[(n+1)A_{n1}^{m}R_s^{n-1}-nB_{n1}^{m}R_s^{-(n+2)}\right]\frac{jmY_n^m(\theta,\phi)}{\sin\theta}e^{j\omega t}\right.\\
&\left.+\sum_{n=0}^{\infty}\sum_{m=-n}^{n}\left[(n+1)C_{n1}^{m}R_s^{n-1}-nD_{n1}^{m}R_s^{-(n+2)}\right]\frac{jmY_n^m(\theta,\phi)}{\sin\theta}e^{-j\omega t}\right\}\\
=&\frac{J_0}{\sin\theta}\frac{e^{j(\omega t-\phi)}+e^{j(-\omega+\phi)}}{2}.
\end{aligned}\tag{4.39}$$

Since high order space harmonics are neglected and the input alternating currents are perfectly sinusoidal, $\vec{B}$ and W are functions of r, θ, and $\cos(\omega t-\phi)$. Resultantly, the item $e^{j\omega t}$ only has the component of m=-1 while the item $e^{-j\omega t}$ only has the component

of m=1. Through further derivations, two sets of equations are derived to determine unknowns in the general solutions.

$$B_{n3}^{-1} = 0\,, \tag{4.40a}$$

$$n(n+1)A_{n3}^{-1}R_b^{n-1} = \left[A_{n2}^{-1}i_n(aR_b) + B_{n2}^{-1}k_n(aR_b)\right]\frac{n(n+1)}{R_b}\,, \tag{4.40b}$$

$$\frac{1}{\mu_r}(n+1)A_{n3}^{-1}R_b^{n-1} = \frac{1}{\mu_m}\left[A_{n2}^{-1}\frac{X_n(aR_b)}{R_b} - B_{n2}^{-1}\frac{Y_n(aR_b)}{R_b}\right]\,, \tag{4.40c}$$

$$n(n+1)A_{n1}^{-1}R_r^{n-1} + n(n+1)B_{n1}^{-1}R_r^{-(n+2)} = \left[A_{n2}^{-1}i_n(aR_r) + B_{n2}^{-1}k_n(aR_r)\right]\frac{n(n+1)}{R_r}\,, \tag{4.40d}$$

$$(n+1)A_{n1}^{-1}R_r^{n-1} - nB_{n1}^{-1}R_r^{-(n+2)} = \frac{1}{\mu_m}\left[A_{n2}^{-1}\frac{X_n(aR_r)}{R_r} - B_{n2}^{-1}\frac{Y_n(aR_r)}{R_r}\right]\,, \tag{4.40e}$$

$$\sum_{n=0}^{\infty}\left[(n+1)A_{n1}^{-1}R_s^{n-1} - nB_{n1}^{-1}R_s^{-(n+2)}\right]\frac{Y_n^1(\theta,\phi)}{\mu_0} = \frac{e^{j\phi}J_0}{2j}\,, \tag{4.40f}$$

$$D_{n3}^{1} = 0\,, \tag{4.41a}$$

$$n(n+1)C_{n3}^{1}R_b^{n-1} = \left[C_{n2}^{1}i_n(bR_b) + D_{n2}^{1}k_n(bR_b)\right]\frac{n(n+1)}{R_b}\,, \tag{4.41b}$$

$$\frac{1}{\mu_r}(n+1)C_{n3}^{1}R_b^{n-1} = \frac{1}{\mu_m}\left[C_{n2}^{1}\frac{X_n(bR_b)}{R_b} - D_{n2}^{1}\frac{Y_n(bR_b)}{R_b}\right]\,, \tag{4.41c}$$

$$n(n+1)C_{n1}^{1}R_r^{n-1} + n(n+1)D_{n1}^{1}R_r^{-(n+2)} = \left[C_{n2}^{1}i_n(bR_r) + D_{n2}^{1}k_n(bR_r)\right]\frac{n(n+1)}{R_r}\,, \tag{4.41d}$$

$$(n+1)C_{n1}^{1}R_r^{n-1} - nD_{n1}^{1}R_r^{-(n+2)} = \frac{1}{\mu_m}\left[C_{n2}^{1}\frac{X_n(bR_r)}{R_r} - D_{n2}^{1}\frac{Y_n(bR_r)}{R_r}\right]\,, \tag{4.41e}$$

$$\sum_{n=0}^{\infty}\left[(n+1)C_{n1}^{1}R_s^{n-1} - nD_{n1}^{1}R_s^{-(n+2)}\right]\frac{Y_n^1(\theta,\phi)}{\mu_0} = \frac{e^{j\phi}J_0}{2j}\,. \tag{4.41f}$$

To help solve unknowns, the right sides of (4.40) and (4.41) are expanded through spherical harmonics. For (4.40f) within the range of $\theta \in [\psi, \pi-\psi]$, we set

$$f(\theta,\phi) = \frac{\mu_0 J_0 e^{j\phi}}{2j} = \sum_{n=0}^{\infty} N_n^{-1} Y_n^1(\theta,\phi)\,, \tag{4.42}$$

where

$$\begin{aligned} N_n^{-1} &= \int_0^{\pi}\int_0^{2\pi} f(\theta,\phi)Y_n^{1*}(\theta,\phi)\sin\theta\,\mathrm{d}\phi\mathrm{d}\theta \\ &= \frac{\mu_0 J_0}{2j}\sqrt{\frac{(2n+1)\pi}{n(n+1)}}\cdot \\ &\quad \left[\sin\theta P_n(\cos\theta)\big|_{\psi}^{\pi-\psi} - \int_{\psi}^{\pi-\psi} P_n(\cos\theta)\cos\theta\,\mathrm{d}\theta\right]\,. \end{aligned} \tag{4.43}$$

4

For each order n, the right sides of (4.44a) and (4.44b) are known.

$$(n+1)A_{n1}^{-1}R_s^{n-1} - nB_{n1}^{-1}R_s^{-n-2} = N_n^{-1}\,, \tag{4.44a}$$
$$(n+1)C_{n1}^{1}R_s^{n-1} - nD_{n1}^{1}R_s^{-n-2} = N_n^{1}\,. \tag{4.44b}$$

Substituting (4.44a) and (4.44b) for (4.40f) and (4.41f), all unknowns in the general solutions can be solved. Magnetic flux density distribution within each region is:

- Region I:

$$\begin{aligned} B_{I,r} = &\sum_{n=1}^{\infty}\left[n(n+1)A_{n1}^{-1}r^{n-1} + n(n+1)B_{n1}^{-1}r^{-(n+2)}\right]Y_n^{-1}(\theta,\phi)e^{j\omega t} \\ &+ \sum_{n=1}^{\infty}\left[n(n+1)C_{n1}^{1}r^{n-1} + n(n+1)D_{n1}^{1}r^{-(n+2)}\right]Y_n^{1}(\theta,\phi)e^{j\omega t}\,, \end{aligned} \tag{4.45a}$$

$$\begin{aligned} B_{I,\theta} = &\sum_{n=1}^{\infty}\left[(n+1)A_{n1}^{-1}r^{n-1} - nB_{n1}^{-1}r^{-(n+2)}\right]\frac{\partial Y_n^{-1}(\theta,\phi)}{\partial\theta}e^{j\omega t} \\ &+ \sum_{n=1}^{\infty}\left[(n+1)C_{n1}^{1}r^{n-1} - nD_{n1}^{1}r^{-(n+2)}\right]\frac{\partial Y_n^{1}(\theta,\phi)}{\partial\theta}e^{-j\omega t}\,, \end{aligned} \tag{4.45b}$$

$$\begin{aligned} B_{I,\phi} = &-\sum_{n=1}^{\infty}\left[(n+1)A_{n1}^{-1}r^{n-1} - nB_{n1}^{-1}r^{-(n+2)}\right]\frac{jY_n^{-1}(\theta,\phi)}{\sin\theta}e^{j\omega t} \\ &+ \sum_{n=1}^{\infty}\left[(n+1)C_{n1}^{1}r^{n-1} - nD_{n1}^{1}r^{-(n+2)}\right]\frac{jY_n^{1}(\theta,\phi)}{\sin\theta}e^{-j\omega t}\,. \end{aligned} \tag{4.45c}$$

- Region II:

$$\begin{aligned} B_{II,r} = &\sum_{n=1}^{\infty}\left[A_{n2}^{-1}i_n(ar) + B_{n2}^{-1}k_n(ar)\right]\left[\frac{n(n+1)}{r}\right]Y_n^{-1}(\theta,\phi)e^{j\omega t} \\ &+ \sum_{n=1}^{\infty}\left[C_{n2}^{1}i_n(br) + D_{n2}^{1}k_n(br)\right]\left[\frac{n(n+1)}{r}\right]Y_n^{1}(\theta,\phi)e^{j\omega t}\,, \end{aligned} \tag{4.46a}$$

$$\begin{aligned} B_{II,\theta} = &\sum_{n=1}^{\infty}\left[A_{n2}^{-1}\frac{X_n(ar)}{r} - B_{n2}^{-1}\frac{Y_n(ar)}{r}\right]\frac{\partial Y_n^{-1}(\theta,\phi)}{\partial\theta}e^{j\omega t} \\ &+ \sum_{n=0}^{\infty}\left[C_{n2}^{1}\frac{X_n(br)}{r} - D_{n2}^{1}\frac{Y_n(br)}{r}\right]\frac{\partial Y_n^{1}(\theta,\phi)}{\partial\theta}e^{-j\omega t}\,, \end{aligned} \tag{4.46b}$$

$$\begin{aligned} B_{II,\phi} = &-\sum_{n=1}^{\infty}\left[A_{n2}^{-1}\frac{X_n(ar)}{r} - B_{n2}^{-1}\frac{Y_n(ar)}{r}\right]\frac{jY_n^{-1}(\theta,\phi)}{\sin\theta}e^{j\omega t} \\ &+ \sum_{n=1}^{\infty}\left[C_{n2}^{1}\frac{X_n(br)}{r} - D_{n2}^{1}\frac{Y_n(br)}{r}\right]\frac{jY_n^{1}(\theta,\phi)}{\sin\theta}e^{-j\omega t}\,. \end{aligned} \tag{4.46c}$$

- Region III:

$$B_{III,r} = \sum_{n=1}^{\infty} n(n+1)A_{n3}^{-1} r^{n-1} Y_n^{-1}(\theta,\phi) e^{j\omega t} + \sum_{n=1}^{\infty} n(n+1)C_{n3}^{1} r^{n-1} Y_n^{1}(\theta,\phi) e^{-j\omega t}, \tag{4.47a}$$

$$B_{III,\theta} = \sum_{n=1}^{\infty} (n+1)A_{n3}^{-1} r^{n-1} \frac{\partial Y_n^{-1}(\theta,\phi)}{\partial\theta} e^{j\omega t} + \sum_{n=1}^{\infty} (n+1)C_{n3}^{1} r^{n-1} \frac{\partial Y_n^{1}(\theta,\phi)}{\partial\theta} e^{-j\omega t}, \tag{4.47b}$$

$$B_{III,\phi} = -\sum_{n=1}^{\infty} (n+1)A_{n3}^{-1} r^{n-1} \frac{jY_n^{-1}(\theta,\phi)}{\sin\theta} e^{j\omega t} + \sum_{n=1}^{\infty} (n+1)C_{n3}^{1} r^{n-1} \frac{jY_n^{1}(\theta,\phi)}{\sin\theta} e^{-j\omega t}. \tag{4.47c}$$

4

4.4. VERIFICATION THROUGH FEM SIMULATIONS

To validate the analytical solutions, numerical models are built in COMSOL. Corresponding to Fig. 4.1, the geometry of the numerical model is presented in Fig. 3.4. This section compares the analytical and numerical results of the magnetic flux density distribution in the air gap. To enable the comparison, several half-circular curves are selected randomly to check the magnetic flux density distribution on the curves.

4.4.1. STATIC FIELD EXCITED BY PMS

As per results presented in subsection 4.3.1, the magnetic field excited by PMs is axially symmetric. Therefore, curves with different azimuth angles ϕ shall have the same magnetic flux density distribution.

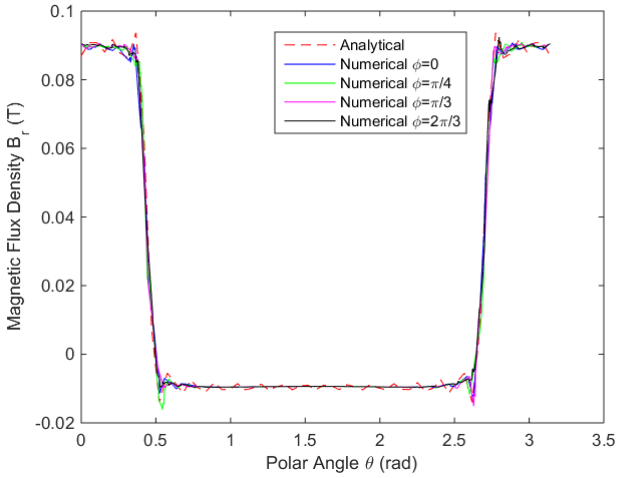

Figure 4.2: Comparison of B_r on curves with various ϕ angles ($r = 25.2$ mm, $\theta \in [0,\pi]$).

The comparison of B_r is shown in Fig. 4.2 and B_θ in Fig. 4.3. The analytical result indicates $B_\phi = 0$ while the numerical results on the selected curves show an average

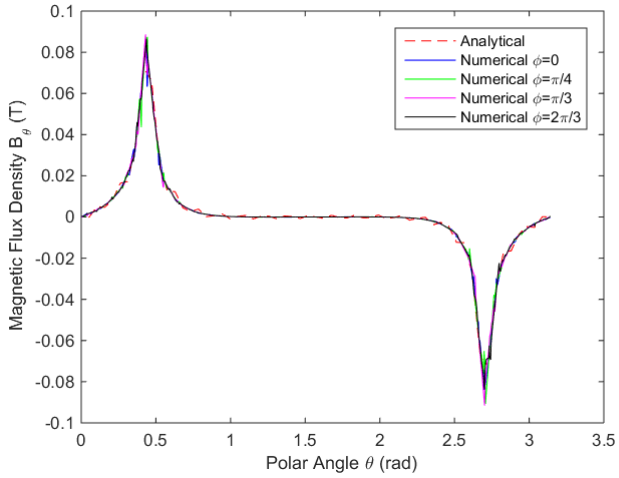

Figure 4.3: Comparison of B_θ on curves with various ϕ angles ($r = 25.2$ mm, $\theta \in [0, \pi]$).

standard deviation of 3.7×10^{-4} T, which is two orders smaller than the magnitudes of B_r and B_θ. In FEM-based simulations, the accuracy of results depends on the element order, size, and the truncation error. Since PMs have a different remanence with the adjacent domains, the first derivative of the magnetic flux density is discontinuous and causes glitches in the graphs. For this reason, the comparison is conducted on the curve with $r = 25.2$ mm. On the rotor surface of $r = 25$ mm, the glitches are more notable. In analytical simulations, the accuracy of this study depends on the number of orders (n) employed in the Fourier-Legendre expansion for M_r. Given above differences, the comparison validates that the static field generated by the PMs is axially symmetrical.

4.4.2. REVOLVING MAGNETIC FIELD EXCITED BY DRIVING WINDINGS

Parameters used in the numerical simulation are listed in Table 4.2. To activate the electromagnetic induction, AC windings placed about the z-axis are energized. As mentioned previously, energized stator windings are approximated by surface currents with the density of $\vec{J}_f = J_0 \cos(\omega t - \phi)/\sin\theta \cdot \vec{e}_\theta$ distributed within the region of $\theta \in [\psi, \pi - \psi]$. The magnitude J_0 is derived from

$$\vec{J}_f = (I_A N_A + I_B N_B + I_C N_C) \cdot \vec{e}_\theta \,, \tag{4.48}$$

where $I_A = I_0 \cos(\omega t)$, $I_B = I_0 \cos(\omega t - 2\pi/3)$ and $I_C = I_0 \cos(\omega t - 4\pi/3)$ are input currents for the three-phase windings. With high order space harmonics neglected, N_A, N_B and N_C are fundamental elements in the Fourier expansion of each phase winding distribution.

For example, the winding distribution of phase A within the region of $\theta \in [\psi, \pi - \psi]$ is described in the stator frame as:

$$N'_a(\phi) = \begin{cases} -N'/\sin\theta, \text{ if } \phi \in [-\zeta/2, \zeta/2] \\ N'/\sin\theta, \text{ if } \phi \in [\pi - \zeta/2, \pi + \zeta/2] \end{cases} , \tag{4.49}$$

Table 4.2: Parameters for the numerical simulation

Parameters	Value
Pole-pair number	p=1
Turn number per phase per pole	N=270
Input AC current magnitude	I_0=2 A
Input AC current angular frequency	ω=20π rad/s
Thickness of the stator back iron	4 mm
The mechanical angle a driving coil spans	ζ=56π/180
Stator wire	AWG 23
Location of stator windings (within R_s)	r$\in$ [26,30] mm
Physical air-gap width	1.0 mm
Relative permeability of Region II	$\mu_m \approx 1$
Relative permeability of Region III	μ_r=30
Relative permeability of stator back iron	4000
Electrical conductivity of Region II	σ=5.998×10^7 S/m
Electrical conductivity of Region III	4.02×10^6 S/m
Electrical conductivity of stator back iron	1.12×10^6 S/m

where $N' = N/(\zeta R_s)$. The minus sign means when the winding is energized with I_0, the carried currents flow along the negative $\vec{e}_\theta$ direction within Region I. $N'_a(\phi)$ is approximated by Fourier series

$$N'_a(\phi) = \sum_{n=1}^{\infty} a_n \cos(n\phi)/\sin\theta \,, \tag{4.50}$$

where

$$\begin{aligned} a_n &= \frac{1}{\pi}\int_{-\pi}^{\pi} N'_a(\phi)\cos(n\phi)\,d\phi \\ &= -\frac{2N'}{n\pi}\sin(\zeta/2) - \frac{2N'}{n\pi}\sin(\pi-\zeta/2)\,. \end{aligned} \tag{4.51}$$

Therefore, the fundamental element is $N_A = a_1\cos(\phi)/\sin\theta$. In the same way, $N_B = a_1\cos(\phi - 2\pi/3)/\sin\theta$ and $N_C = a_1\cos(\phi - 4\pi/3)/\sin\theta$. With the balance three-phase input currents, the magnitude of $\vec{J}_f$ is derived to be $J_0 = 1.5 I_0 a_1 \approx -16513\ A/m$.

Similar to the previous subsection, several curves are picked up to study the magnetic flux density distribution in the air gap. Since the remanence of PMs is set to zero in this simulation case, glitches caused by the discontinuous first derivative of the flux density disappear. The comparison of results is conducted on the rotor surface $r = 25$ mm for the finner mesh there. Comparisons for B_r and B_ϕ on the first curve ($r = 25$ mm, $\theta = \pi/2$, $\phi \in [0, 2\pi]$) are shown in Fig. 4.4 and Fig. 4.5. The analytical result indicates $B_\theta = 0$ on the selected curve while the numerical result gives a standard deviation of 1.98×10^{-4} T (two

orders smaller than the magnitudes of B_r and B_ϕ). Comparisons for $\vec{B}$ on the second curve ($r = 25$ mm, $\phi = \pi/4$, $\theta \in [0, \pi]$) are presented in Fig. 4.6, Fig. 4.7 and Fig. 4.8. Since the electromagnetic field is revolving, the magnetic flux density distribution at the time instant of $t = 0.1$ s is analysed.

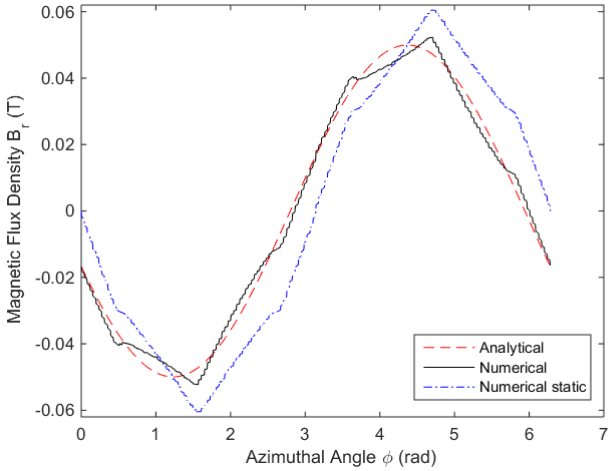

Figure 4.4: Comparison of B_r on the 1^{st} curve ($r = 25$ mm, $\theta = \pi/2$, $\phi \in [0, 2\pi]$) at t=0.1 s.

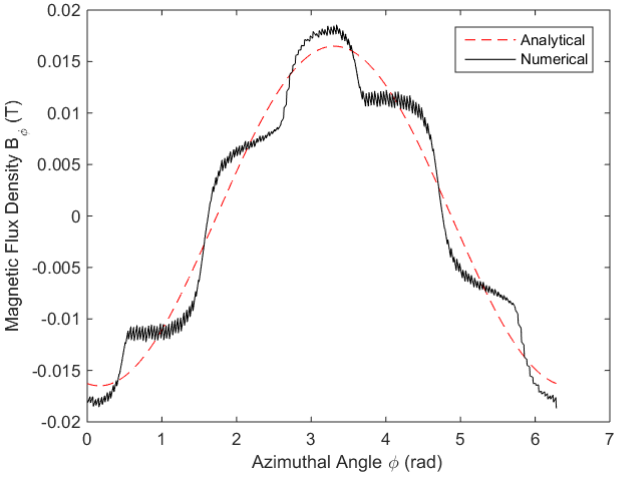

Figure 4.5: Comparison of B_ϕ on the 1^{st} curve ($r = 25$ mm, $\theta = \pi/2$, $\phi \in [0, 2\pi]$) at t=0.1 s.

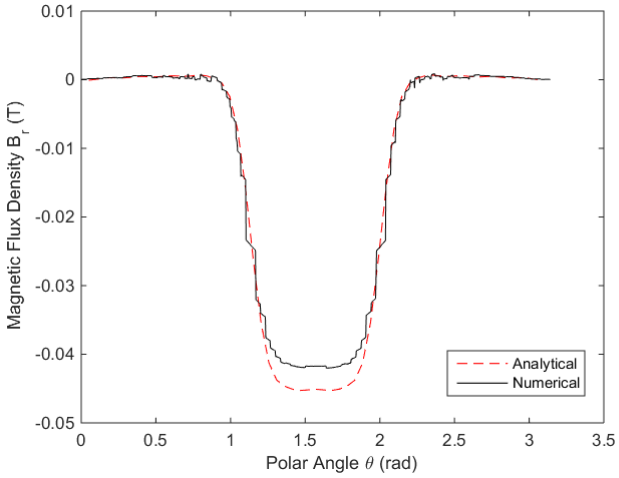

Figure 4.6: Comparison of B_r on the 2^{nd} curve ($r = 25$ mm, $\phi = \pi/4$, $\theta \in [0, \pi]$) at t=0.1 s.

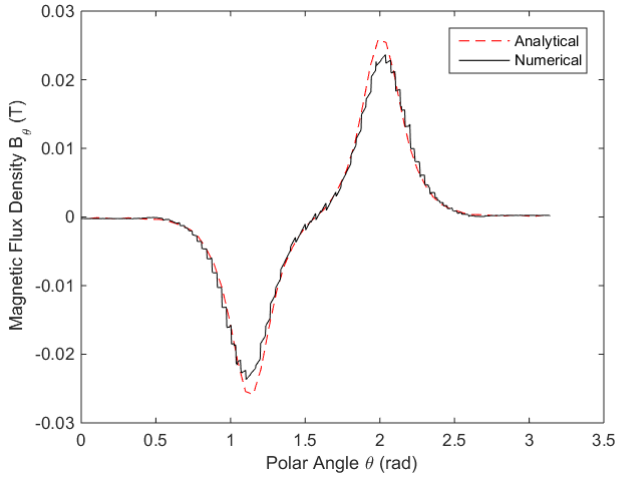

Figure 4.7: Comparison of B_θ on the 2^{nd} curve ($r = 25$ mm, $\phi = \pi/4$, $\theta \in [0, \pi]$) at t=0.1 s.

4.4.3. DISCUSSIONS ON DYNAMIC FIELDS

Through comparisons of the analytical and numerical results, it is validated that modeling the stator currents as AC surface current is principally reasonable. However, there are slight differences between the analytical and numerical results.

In Fig. 4.4, the numerical results for B_r do not exactly follow a sinusoidal function. Instead, deformations are observed around the maximum and the minimum. To explain this phenomenon, the B_r distribution in the static field generated by DC inputs ($I_B = I_C = -I_A/2 = -1$ A, equivalent to the inputs of AC windings at t=0.1 s) is presented in the

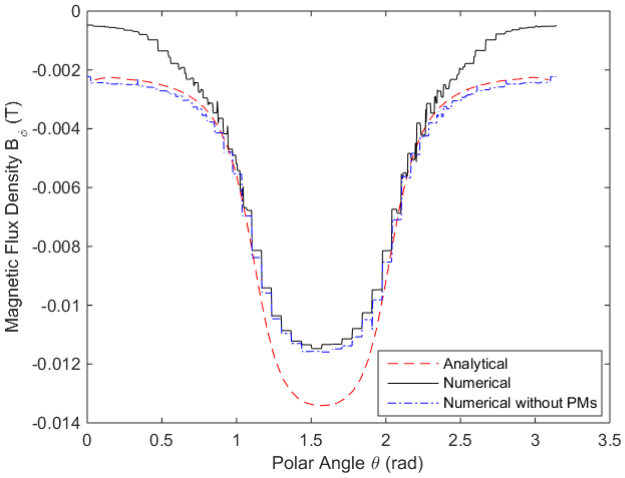

Figure 4.8: Comparison of B_ϕ on the 2^{nd} curve ($r = 25$ mm, $\phi = \pi/4$, $\theta \in [0, \pi]$) at t=0.1 s.

figure too. It is notable that B_r in the dynamic field is ahead of the static field in phase. Besides, its distribution is out of shape at the top parts. Actually, both deviations are caused by eddy currents.

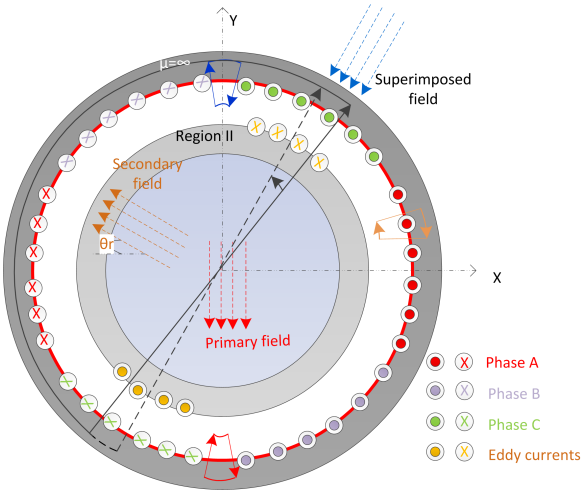

Figure 4.9: Superposition of the primary and secondary fields due to eddy currents.

At t=0.1 s, the direction of the primary magnetic field (excited by stator currents) is along the negative y-axis (see Fig. 4.9). As per Lentz's law, eddy currents will be induced in the copper with the axis broadly opposite to that of stator currents. The angular displacement θ_r is determined by the rotor time-constant. As a result, the secondary field

generated by eddy currents changes the primary field. It makes the maximum B_r direction to be ahead of that in the primary field.

To explain deformations of the B_r distribution, a semicircle contour is used (see Fig. 4.9). As per Ampere's law, $\oint_C \vec{H} \cdot \vec{\tau} dC = i_{\text{inc}}$. Since $\vec{H}$ is zero inside the stator back iron, the integration of H_r along the straight line is determined by the inclosed currents. However, when the straight line of the contour sweeps through the area where eddy currents and stator currents have opposite directions, the increase /decrease of inclosed stator currents is partially canceled out by eddy currents. Therefore, in such areas (for instance $0.9 - \pi/2$ rad), the magnitude of B_r in the dynamic field is smaller than that in the static field. In the analytical model, both stator currents and eddy currents are sinusoidally distributed. However, in the numerical model, higher space harmonics exist in the winding distribution. Therefore, when the straight line of the contour sweeps, the change of enclosed currents is not sinusoidal. This reason contributes to the deformation around the maximum and the minimum. This deformation is also presented in Fig. 4.6.

For the B_ϕ distribution in Fig. 4.5, the numerical result exhibits an imperfect sinusoidal curve due to the non-sinusoidally distributed windings. A small contour above the positive x-axis is drawn in Fig. 4.9 for illustration. The angle of the contour is so small that we assume the integration of $\vec{H}$ along the two straight sides cancels each other and H_ϕ in the air gap solely depends on the inclosed stator currents. Therefore, step changes of the B_ϕ distribution occur at the interfaces of different winding phases. Sparks in Fig. 4.5 are due to the different mesh sizes used for winding domains and gaps between winding domains. In addition, both the analytical and numerical results in Fig. 4.5 show a slight phase lag from a negative cosine wave. Actually, although the angle of the contour is very small, the integrations of $\vec{H}$ along the two straight sides do no counteract each other completely. For instance, at $\phi = \pi/2$, H_r is negative and its magnitude at the right side (in Fig. 4.9) is larger than the left side due to the shafted B_r distribution in the superposed field (This is better illustrated by the analytical results in Fig. 4.4). Hence, the integration of $\vec{H}$ along the two sides results in a positive value and H_ϕ in the air gap is negative. Similarly, H_ϕ in the air gap is positive at $\phi = -\pi/2$. Hence, a slight phase shift is generated.

The B_θ component in Fig. 4.7 is mainly caused by stator leakages. In the numerical model, the stator back iron is not a complete shell. Gaps exist between the top/bottom shells and the iron wound with windings (see Fig. 3.4). At the axial ends of the stator windings, the magnetic flux path to the top/bottom shells is shorter than that to the rotor core, which leads to stator leakages between stator windings and the top/bottom shells. However, in the analytical model, the gaps are not taken into account. Therefore, the analytical result gives a larger peak value of B_θ than the numerical result.

With respect to the B_ϕ distribution in the polar areas of Fig. 4.8, deviations from the numerical results are due to the assumption that PMs have the same conductivity with copper. Eddy currents flow through there in the analytical model and generate B_ϕ in the polar area. This explanation is validated by the B_ϕ distribution got from the numerical simulation without PMs on the rotor (where the copper layer is a complete spherical shell).

In sections 4.2 and 4.3, the dynamic field model is developed for the case where only one set of driving windings is energized and the orientation of the energized winding

set is specific (about the z-axis). However, the field model is also applicable to cases where more than one set of windings are energized wherever their orientations. Due to the linearity of Laplace equations and heat diffusion equations, as well as the principle of vector superposition, flux density distributions or eddy current distributions excited by two or more windings can be obtained by summing up solutions of cases where each set of windings is energized respectively. In the case where the energized winding set is not about the z-axis, flux density distribution in the field can be obtained through the coordinate conversion of the results presented above. Furthermore, if only a few coils are energized rather than the whole winding set, the developed field model is still applicable. In that case, only the equation of the approximated surface current needs to be changed.

4.5. ELECTROMAGNETIC TORQUES AND FORCES

Once AC windings are activated, driving torques will be generated. They can be calculated through the Maxwell stress tensor (MST) or Lorentz forces acting on the eddy currents.

- The rotor core (Region III) is made of laminated steel. Although some eddy currents are induced there, the arm length of the generated Lorentz force is short. Consequently, the electromagnetic torque arising from these eddy currents is negligible. In the numerical model, the driving torque provided by the steel domain is only 3.5% of that generated in the copper area. Therefore, eddy currents are assumed to be induced only in the copper area

$$T_{eL} = -\int_0^{2\pi}\int_{R_b}^{R_r}\int_{\beta/2}^{\pi-\beta/2} J_\theta B_r r^3 \sin^2\theta \, \mathrm{d}\theta \mathrm{d}r \mathrm{d}\phi \,. \tag{4.52}$$

- The MST method is based on the idea of calculating electromagnetic forces on charges in a certain volume. Through tensor arithmetic, the volume integral is converted to a surface integral of local tangential stress on the boundary surface. This approach is usually applied in finite element solutions, since it only requires knowledge of the local flux density distribution at the boundaries [23, 157].

$$T_{eM} = \int_0^{2\pi}\int_0^{\pi} H_\phi B_r r^3 \sin^2\theta \, \mathrm{d}\theta \mathrm{d}\phi \,. \tag{4.53}$$

When the rotor is blocked and driving windings on the equatorial plane are energized, the generated electromagnetic torque is calculated in two different ways. Torque calculations based on the analytical field model and those based on the numerical field distribution are compared in Table 4.3, with the errors never exceeding 4%. Since the existence of PMs within region II is not taken into account for the dynamic field modeling, the driving torques result from the analytical model are close to those obtained from the numerical model without PMs (where the copper layer is a complete spherical shell). The small deviation (<2%) is caused by the neglected stator eddy currents, which weaken the flux density in the air gap. Compared to the driving torques result from the numerical model where PMs exist (whether the remanence is set to zero or 0.23 T listed in Table 4.1), the deviation of the analytical results increases. This deviation is contributed by the existence of PMs which disturbs the circulation of eddy currents on the rotor.

Table 4.3: Comparison of generated electromagnetic torques

Torques	Analytical	Numerical without PMs	Numerical with PMs
T_{eM} [mNm]	12.18	12.17 (<1%)	11.75 (3.6%)
T_{eL} [mNm]	12.18	12.028 (1.3%)	11.70 (4%)

4.6. DISTURBANCES INTRODUCED BY PMS

As analyzed in previous sections, the static field of PMs displaces the revolving magnetic field excited by AC currents. For instance, on the equatorial plane, the magnetic flux density on one side is stronger than that on the other side. Since eddy currents in the copper region are induced by the revolving magnetic field, the resultant Lorentz force on one side is larger than that of the opposite side. Consequently, except for driving torques, a resulting force is generated. Besides, since the flux density on one gap side is larger than on the other side, a non-linear sticking force will be generated between the ferromagnetic rotor core and the stator back iron. These two factors form a radial force that is revolving at the same frequency as the input frequency of the driving windings. If this disturbance force is not handled properly, it could contribute to the pointing error and be transferred to the payload, causing imaging distortion for observation missions. If the disturbance force causes resonance with on-board elements such as telescope mirrors, it could cause damages. To mitigate this disturbance force, the approach of a bearing-less induction machine [158] can be adopted. Bearing coils placed co-axially with the driving coils are changed to AC fed and work as 2-pol-pair 3-phase windings (the frequency is double that of the driving windings). The phase angle of bearing input currents will be adjusted to make the bearing windings electrically orthogonal to the driving windings. By adjusting the AC input currents of the bearing windings, the unbalanced flux density in the opposite gap sides can be compensated.

4.7. SUMMARY

Analytical models have been developed to predict the magnetic flux density distribution within the reaction sphere, where both PMs and alternating stator currents are involved. Compared to models presented in the literature, the component of B_θ is maintained in the developed field model. The distribution of B_θ excited by stator windings reveals non-negligible flux leakage in spherical actuators. Based on the obtained field information, models of the generated torques were built up subsequently. Comparisons with the numerical results validated that the developed analytical models allow to predict the magnetic flux density distribution and driving torques precisely. In addition, the presented analytical models are generally applicable to static and dynamic fields in spherical machines.

5

PERFORMANCE ANALYSIS OF INDUCTION-BASED REACTION SPHERES

5.1. INTRODUCTION

In induction-based reaction spheres, multiple sets of AC windings are placed around the conductive rotor and are controlled independently. As per vector superposition, the generated driving torque can be about any desired direction [31, 160, 161]. This concept was first proposed in [11] for the stabilizability of space telescopes. Its feasibility was studied through experiments of single-axis rotations in [60] and multi-axis rotations in [14]. Regarding performance analysis, current research normally focuses on the case of single-axis rotations to minimize the effects of cross-couplings. In [13], torque-speed characteristics of a single-axis spinning reaction sphere were investigated through experiments on a prototype. To save development cost and allow researchers to evaluate designs before prototyping, [162] and [26] employed numerical simulations to examine performance characteristics as well as their dependencies on design variables. However, dynamic simulations of a 3-dimensional finite element model are time-consuming and require a large amount of memory [25]. Besides, the required time and memory amount increase rapidly when finer meshes or smaller time-step sizes are adopted [163]. To solve this problem, this chapter presents an analytical way to model the influences of design variables on the actuator's performance characteristics.

5.2. DETERMINATION OF EQUIVALENT CIRCUIT PARAMETERS

Due to the resemblance between the single-axis rotation of induction-based reaction spheres and that of conventional induction machines, the equivalent circuit approach is

The content of section 5.1 to section 5.3 has been published in IEEE Transactions on Industrial Electronics **67**, 7746 (2019) [159].

employed to predict driving performances. Circuit parameters are determined through the magnetic flux density distribution which is an analytical function of design variables. Based on this, performance characteristics such as the achievable maximum torque T^* can be calculated within seconds.

Normally, an induction-based reaction sphere incorporates ball bearings or magnetic bearings if additional stator coils/windings are mounted. The challenge of employing magnetic bearings is the cross-coupling between the suspension and the driving functions, and consequent disturbance forces/torques. In such cases, control of the reaction sphere becomes complicated. The cross-coupling and disturbances brought by magnetic bearings can be avoided by employing air bearings or ball bearings. Air bearings are popular in ground experiments and they facilitate functional tests of the driving unit. However, employing air bearings in space is difficult. Therefore, ball bearing is the preferred choice in this research. Although ball bearings introduce friction and require lubrication, these drawbacks can be overcome by properly selected ball material and lubricants.

In chapter 4, the dynamic magnetic field excited by 3-phase stator windings is modeled analytically. When the rotor is stationary (i.e., the slip s=1), Region II is governed by a heat diffusion equation. Distributions of magnetic flux density in region II are given in (4.45) and are rewritten as:

$$B_{II,r}(r,\theta,\phi) = -2\sum_{n=1}^{\infty} Re\left[(\zeta_n i_n(ar) + \nu_n k_n(ar))\frac{n(n+1)}{r}Q_n^1(\theta)e^{j(\omega t-\phi)}\right], \tag{5.1a}$$

$$B_{II,\phi}(r,\theta,\phi) = 2\sum_{n=1}^{\infty} Re\left[(\zeta_n X_n(ar) - \nu_n Y_n(ar))\frac{jQ_n^1(\theta)}{r\sin\theta}e^{j(\omega t-\phi)}\right], \tag{5.1b}$$

where $\zeta_n = A_{n2}^{-1}$ and $\nu_n = B_{n2}^{-1}$. And $Q_n^1(\theta)$ is the θ-related part of spherical harmonics $Y_n^1(\theta,\phi)$ and it is defined in the Appendix. The analytical model developed in chapter 4 also allows the calculation of magnetic flux density distribution at the slip s=0. In that case, the governing equation of Region II degrades to a Laplace equation since no eddy currents are induced. All the boundary conditions keep unchanged.

Additionally, the analytical field model can be extended to take high order space harmonics into account. This is done by replacing $\cos(\omega t-\phi)$ in the equation of the approximated surface current density with Fourier series, which are obtained from the Fourier expansion of the 3-phase winding distribution function. Although the extended field model describes the flux density distribution in the numerical model better, the model without high order harmonics is adopted here, for two reasons. Firstly, compared to the fundamental element, high order harmonics contribute little to the overall performance of the actuator [164]. Secondly, in this study, performances of the single-axis spinning reaction sphere are predicted through the equivalent circuit approach. The determination and validation of circuit parameters corresponding to high order space harmonics are challenging. Therefore, high order space harmonics are not considered.

Based on the solved magnetic flux density distribution, electromagnetic torques acting on the rotor can be calculated through the Maxwell stress tensor. However, the field model in chapter 4 is only for cases of blocked-rotor (s=1) or synchronous rotations (s=0). If the reaction sphere is spinning at a velocity $\vec{v}$ (a non-synchronous speed), the

governing equation of Region II will become [23]:

$$\nabla^2 \vec{A} = \mu_0 \mu_{r,c} \sigma \left(\frac{\partial \vec{A}}{\partial t} - \vec{v} \times (\nabla \times \vec{A}) \right) . \tag{5.2}$$

Since the magnetic vector potential $\vec{A}$ has three components, the vector $\vec{v} \times (\nabla \times \vec{A})$ is not necessarily aligned with the vector $\partial \vec{A}/\partial t = j\omega \vec{A}$. From the mathematical aspect, it is not correct to simplify $\partial \vec{A}/\partial t - \vec{v} \times (\nabla \times \vec{A})$ to $j(\omega - \omega_m)\vec{A}$, where $\omega_m = v/r$ is the mechanical angular speed. The formula $\partial \vec{A}/\partial t - \vec{v} \times (\nabla \times \vec{A})$ involves many items. Without specific values, it is difficult to determine which item is significant and which item is negligible from the mathematical aspect. Therefore, simplifying (5.2) and calculating driving torques at a random slip analytically is difficult.

Due to the resemblance between the single-axis rotating reaction sphere and conventional induction machines, the equivalent circuit approach is adopted to predict generated torques. Typically, parameters involved in the equivalent circuit are derived from no-load (s=0) and blocked-rotor (s=1) experiments with the assumption of identical inductances of the stator leakage $L_{s\sigma}$ and referred rotor leakage $L'_{R\sigma}$ [165]. However, due to toroidal windings, $L_{s\sigma}$ is expected to be much larger than $L'_{R\sigma}$ and the typical method becomes inapplicable. To help researchers determine circuit parameters of a newly designed reaction sphere quickly, an analytical way is presented here.

5.2.1. PARAMETER DETERMINATION BASED ON THE FIELD MODEL

To facilitate the calculation of flux linkage, we assume the copper layer on the rotor is replaced by short-circuit windings. In this study, high order space harmonics are neglected in both the stator and rotor winding distributions. The flux linkage of rotor windings is calculated by [166] (with the magnitude-invariant Clarke transformation):

$$|\vec{\lambda}_r^s| = \lambda_{rp} = \pi/4 \cdot N_{re} \cdot \Phi_{rp} . \tag{5.3}$$

The superscript s refers to the stator frame. Φ_{rp} is the maximum flux per pole flowing through rotor windings and N_{re} is the effective turn number per phase per pole, corresponding to the fundamental element in the winding distribution. Since rotor windings are virtual, N_{re} is unknown. However, when $\vec{\lambda}_r^s$ is referred to the stator side by $\vec{\lambda}_R^{s\prime} = (N_{se}/N_{re})\vec{\lambda}_r^s$ [166], the referred rotor flux linkage becomes $|\vec{\lambda}_R^{s\prime}| = \pi/4 \cdot N_{se}\Phi_{rp}$. N_{se} is the effective turn number of stator windings and is calculated by $N_{se} = 4/\pi \cdot k_w N$. Hence, the referred rotor flux linkage becomes $|\vec{\lambda}_R^{s\prime}| = k_w N \Phi_{rp}$.

k_w is the fundamental distribution factor of phase windings. In chapter 4, the fundamental element of phase windings are expressed as $N_A = a_1 \cos(\phi)/\sin\theta$, $N_B = a_1 \cos(\phi - 2\pi/3)/\sin\theta$ and $N_C = a_1 \cos(\phi - 4\pi/3)/\sin\theta$ within the region of $\theta \in [\psi, \pi - \psi]$. The effective turn number N_{se} corresponds to the fundamental wave in the Fourier expansion in the winding distribution. On the equatorial plane where $\theta = \pi/2$, N_{se} can be calculated through

$$N_{se} = R_s |a_1| \int_{-\pi/2}^{\pi/2} \cos(\alpha) \mathrm{d}\alpha = 2R_s |a_1| . \tag{5.4}$$

Meanwhile, from the engineering aspect, N_{se} can be expressed as

$$N_{se} = 4/\pi k_w N . \tag{5.5}$$

Therefore, with a_1 available from (4.51), k_w can be derived from (5.4) and (5.5):

$$k_w = \frac{\pi}{2}\frac{R_s}{N}\cdot|a_1| = \frac{\pi}{2}\frac{R_s}{N}\frac{4N\sin(\zeta/2)}{\pi\zeta R_s} = \frac{2}{\zeta}\sin(\zeta/2) \approx 0.96 \tag{5.6}$$

Given the filed distribution, Φ_{rp} can be obtained by integrating B_r on the surface at r=R_w (the radial center of rotor windings or eddy currents). However, due to the skin effect, to determine the location of r=R_w is challenging. Therefore, B_r is integrated on the external and internal surfaces of Region II, respectively, and the average is taken: Φ_{rp}= $(\Phi_{rp,Rb}$+$\Phi_{rp,Rr})/2$. Since azimuthal currents (flowing along $\vec{e}_\phi$) are induced on the rotor, integrations of B_r are executed within specific ranges of θ. The center of azimuthal eddy currents is assumed to be parallel to the center of stator end windings (see Fig. 4.1, at the height z^*=$R_s\cos(\psi)$). Therefore, integration ranges are $\theta \in [\theta_b, \pi$-$\theta_b]$ (where θ_b=$\cos^{-1}(z^*/R_b)$) on the surface at r=R_b and $\theta \in [\theta_r, \pi$-$\theta_r]$ (where θ_r=$\cos^{-1}(z^*/R_r)$) at r=R_r respectively:

$$\Phi_{rp,R_b} = \int_{\phi_b}^{\phi_b+\pi}\int_{\theta_b}^{\pi-\theta_b} B_r(R_b,\theta,\phi)R_b^2\sin\theta\,\mathrm{d}\theta\,\mathrm{d}\phi\,, \tag{5.7a}$$

$$\Phi_{rp,R_r} = \int_{\phi_r}^{\phi_r+\pi}\int_{\theta_r}^{\pi-\theta_r} B_r(R_r,\theta,\phi)R_r^2\sin\theta\,\mathrm{d}\theta\,\mathrm{d}\phi\,. \tag{5.7b}$$

ϕ_b and ϕ_r are angles which maximize Φ_{rp,R_b} and Φ_{rp,R_r}.

Meanwhile, the expression of $\vec{\lambda}_R^{s\prime}$ in the equivalent circuit (see Fig. 5.1) is

$$\vec{\lambda}_R^{s\prime} = L'_{R\sigma}\vec{i}_R^{s\prime} + L_{sm}\left(\vec{i}_s^{s} + \vec{i}_R^{s\prime}\right)\,, \tag{5.8}$$

where L_{sm} is the magnetization inductance, $\vec{i}_s^{s}$ and $\vec{i}_R^{s\prime}$ are vectors of the stator current and the referred rotor current.

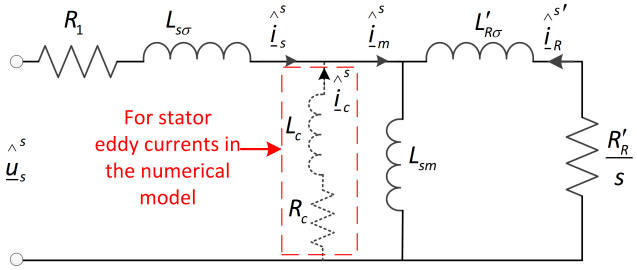

Figure 5.1: The equivalent circuit of induction machines for the steady state.

In steady states of s=0, there are no rotor currents. With the known stator current, L_{sm} can be calculated through

$$L_{sm} = \left|\frac{\hat{\underline{\lambda}}_{R,s=0}^{s\prime}}{\hat{\underline{i}}_{s,s=0}^{s}}\right| = \frac{k_w N\Phi_{rp,s=0}}{|\hat{\underline{i}}_{s,s=0}^{s}|}\,. \tag{5.9}$$

Symbols with a hat refer to phasors (complex quantities) and variables in steady states are underlined.

In the steady state of s=1, the electromagnetic torque is [164, 165]:

$$T_{s=1} = 1.5R'_R|\hat{\underline{i}}^{s\prime}_{R,s=1}|^2/\omega_{syn}\ , \tag{5.10}$$

where R'_R is the referred rotor resistance and $\omega_{syn} = \omega/p$ is the mechanical synchronous speed. With the solved magnetic flux density distribution, $T_{s=1}$ can be obtained by the Maxwell stress tensor. Additionally, the rotor voltage equation in steady states is

$$0 = R'_R\hat{\underline{i}}^{s\prime}_R/s + j\omega\hat{\underline{\lambda}}^{s\prime}_R\ . \tag{5.11}$$

With the known angular frequency ω, and analytically calculated $T_{s=1}$ and $|\hat{\underline{\lambda}}^{s\prime}_{R,s=1}|$, the magnitude of $\hat{\underline{i}}^{s\prime}_{R,s=1}$ and R'_R can be solved through the equation set of (5.10) and (5.11).

As per (5.11), $\hat{\underline{i}}^{s\prime}_R$ is orthogonal to $\hat{\underline{\lambda}}^{s\prime}_R$ in the phasor diagram. Based on this relation and the Pythagorean theorem, $L'_{R\sigma}$ can be calculated by transforming (5.8) to

$$L'_{R\sigma} = \sqrt{L^2_{sm}|\hat{\underline{i}}^{s}_{s,s=1}|^2 - |\hat{\underline{\lambda}}^{s\prime}_{R,s=1}|^2}\Big/|\hat{\underline{i}}^{s\prime}_{R,s=1}| - L_{sm}\ . \tag{5.12}$$

Related data and derived parameters are listed in Table 5.1. Since the actuator will be fed with controlled stator currents, only L_{sm}, $L'_{R\sigma}$ and R'_R are concerned in the equivalent circuit.

For comparison, the presented determination method is applied to the numerical model developed in COMSOL. Φ_{rp,R_b} and Φ_{rp,R_r} in (5.7) are obtained by integration of the local B_r distribution on the internal and external surfaces of Region II in the numerical model. Referred rotor flux linkages $|\hat{\underline{\lambda}}^{s\prime}_{R,s=0}|$ and $|\hat{\underline{\lambda}}^{s\prime}_{R,s=1}|$ are obtained through $|\hat{\underline{\lambda}}^{s\prime}_R|$=$0.5k_wN(\Phi_{rp,R_b}+\Phi_{rp,R_r})$ in no-load and blocked-rotor simulations respectively. The torque $T_{s=1}$ is provided by the Maxwell Stress Tensor feature in the blocked-rotor simulation.

In the numerical model, since eddy currents are induced in the stator back iron, the current virtually flowing to the air gap and the rotor side in the equivalent circuit becomes $\hat{\underline{i}}^{s}_m$ (see Fig. 5.1 where the resistance R_c and inductance L_c of the stator iron are included). The stator eddy current $\hat{\underline{i}}^{s}_c$ is identified from the numerical model by two steps. Firstly, integrating the volume density of stator eddy currents on the equatorial plane within per pole area results in I_{is}. Next, stator eddy currents are approximated as sinusoidally distributed surface currents at r=R_s+δ (where δ is very small as compared to R_s). The magnitude of approximated surface current density is $J_{is}/\sin\theta \approx (I_{is}/2R_s)/\sin\theta$. Due to the high permeability of the stator iron, the distribution of H_ϕ at r=R_{s+} (the side within the stator iron, i.e., $R_{s+} > R_s$) is analyzed through the image method which results in $H_\phi|_{r=R_{s+}} \approx 2J_{is}\cos(\omega t$+$\alpha$-$\phi)/\sin\theta$. The angle α is the phase difference between distributions of stator eddy current density and input stator current density on the equatorial plane. To reveal the influence of stator eddy currents, the boundary condition at r=R_s in the analytical field model is recalled. Due to J_{is}, it becomes

$$H_{I\phi}|_{r=R_s} = \frac{J_s}{\sin\theta}\cos(\omega t-\phi) + \frac{2J_{is}}{\sin\theta}\cos(\omega t+\alpha-\phi)\ . \tag{5.13}$$

Table 5.1: Results and Comparison of Parameter Determination Based on the Field Distribution

	Param	Analytical model	Numerical model
$s=0$	$\lvert\hat{\underline{i}}^{s}_{s,s=0}\rvert$	2 A	2 A
	$\lvert\hat{\underline{i}}^{s}_{c,s=0}\rvert$	0 A	0.0238 A (α=π-1.45)
	$\lvert\hat{\underline{\lambda}}^{s\prime}_{R,s=0}\rvert$	$k_w N \cdot 5.635 \times 10^{-5}$ Wb	$k_w N \cdot 5.628 \times 10^{-5}$ Wb
$s=1$	$\lvert\hat{\underline{i}}^{s}_{s,s=1}\rvert$	2 A	2 A
	$\lvert\hat{\underline{i}}^{s}_{c,s=1}\rvert$	0 A	0.0226 A (α=π-1.45)
	$\lvert\hat{\underline{\lambda}}^{s\prime}_{R,s=1}\rvert$	$k_w N \cdot 4.83 \times 10^{-5}$ Wb	$k_w N \cdot 4.75 \times 10^{-5}$ Wb
	$T_{s=1}$	12.18 mNm	12.16 mNm
Outputs	L_{sm}	7.30 mH	7.29 mH
	$L'_{R\sigma}$	4.29 mH	4.53 mH
	R'_R	1.214 Ω	1.175 Ω

5

Inverting the calculation of J_s from $|\hat{\underline{i}}^{s}_{s}|$, $|\hat{\underline{i}}^{s}_{c}|$ is obtained from $2J_{is}$. The phase angle is $\arg\hat{\underline{i}}^{s}_{c}$=$\arg\hat{\underline{i}}^{s}_{s}$+$\alpha$.

With known input stator currents and quantified stator eddy currents for both the no-load and the blocked-rotor simulations, obtained $|\hat{\underline{\lambda}}^{s\prime}_{R,s=0}|$, $|\hat{\underline{\lambda}}^{s\prime}_{R,s=1}|$ and $T_{s=1}$, circuit parameters (i.e. L_{sm}, $L'_{R\sigma}$ and R'_R) corresponding to the numerical field model are derived from (5.9)-(5.12).

As illustrated in Table 5.1, differences between circuit parameters derived from the analytical field model and those derived from the numerical field model are within 6%.

5.2.2. PARTIAL VALIDATION OF THE PARAMETER DETERMINATION METHOD

In this part, the no-load and blocked-rotor method is applied with the assumption of L_{sm}=7.3 mH, to partially validate parameters determined in section 5.2.1. Since prototypes are not available, required electrical measurements are obtained from dynamic simulations of the 3D numerical model. The numerical model is built in COMSOL through the Rotating Machinery, Magnetic physics interface. It is the same numerical model that has been mentioned in chapter 4 and section 5.2.1. Electrical data such as the stator current, resistance and voltage of each winding phase, as well as the 3-phase power are available. Simulations for the case of no-load and the case of blocked-rotor were run respectively. Electrical measurements obtained from the dynamic simulations are listed in Table 5.2.

In the numerical model, since stator windings are non-sinusoidally distributed, high order space harmonics exist. The extended equivalent circuit considering space harmonics [167, 168] is presented in Fig. 5.2. Except for parameters corresponding to the fundamental space harmonic (i.e., R_c, L_{sm}, R'_R and $L'_{R\sigma}$), circuit parameters corresponding to high order harmonics are also involved. Compared to Fig. 5.1, L_c is missing in Fig. 5.2. The reason is explained later in this section. Since the purpose of this subsection is to validate circuit parameters derived in section 5.2.1 which are for the fundamental har-

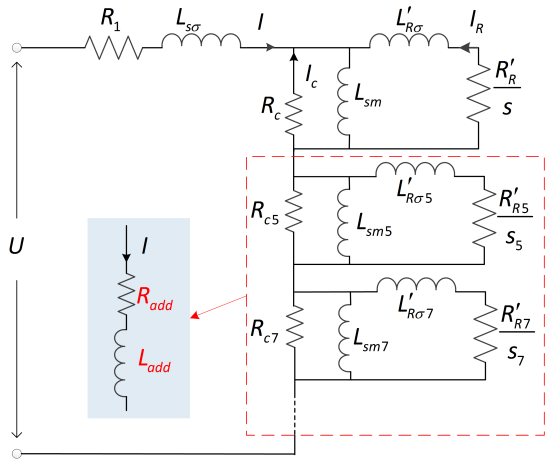

Figure 5.2: The extended equivalent circuit for the numerical model.

5

Table 5.2: Parameter Determination Based on Electrical Data

	Parameters	No-load	Blocked-rotor
Measurements	Stator resistance	R_1 =2.335Ω	R_1 = 2.335 Ω
	Phase current	I_{NL}=$\sqrt{2}$ A (rms)	I_{BL}=$\sqrt{2}$ A (rms)
	Phase voltage	U_{NL}=3.05$\sqrt{2}$ V (rms)	U_{NL}=3.1$\sqrt{2}$ V (rms)
	3-phase power	P_{NL}=14.1 W	P_{BL}=14.9 W
	Stator eddy current	$I_{c,NL}$=0.0238/$\sqrt{2}$ A (rms)	$I_{c,BL}$=0.0226/$\sqrt{2}$ A (rms)
	Torque		T_{BL}=12.16 mNm
Assumption	L_{sm} = 7.30 mH		
Outputs	$L_{s\sigma} + L_{add}$ = 23.64 mH		
	$L'_{R\sigma}$ = 4.675 mH		
	R'_R = 1.127 Ω		

monic, only L_{sm}, R'_R and $L'_{R\sigma}$ are concerned here. Due to the difficulty of determining all involved parameters, circuits corresponding to high order harmonics are transformed to an equivalent serial circuit composed of R_{add} and L_{add} in Fig. 5.2. Values of R_{add} and L_{add} vary with input frequencies and the slip.

As mentioned at the beginning of this part, the partial validation is conducted with the assumption of L_{sm}=7.3 mH. R'_R and $L'_{R\sigma}$ derived from the electrical measurements will be compared to those listed in Table 5.1.

Although R_1 is directly available from COMSOL simulations and L_{sm} is assumed, it is still difficult to determine the other parameters in the transformed equivalent circuit.

In the conventional electrical measurement approach, measured phase voltages, phase currents and 3-phase powers result in four equations in total:

- When the rotor is running at s=0 (no-load) with the input angular frequency of ω:

$$R_1 + R_{add,NL} + R_{NL} = \frac{P_{NL}}{3I_{NL}^2}\,, \tag{5.14a}$$

$$X_{s\sigma} + X_{add,NL} + X_{NL} = \sqrt{(\frac{V_{NL}}{I_{NL}})^2 - (\frac{P_{NL}}{3I_{NL}^2})^2}\,. \tag{5.14b}$$

  where $Z_{NL} = R_{NL} + jX_{NL}$ is the impedance of the parallel circuit formed by R_c and $j\omega L_{sm}$ in the no-load state. Since all space harmonics have the same angular frequency ω [169], the reactance X is always the product of ω and the corresponding inductance L.

- When the rotor is running at s=1 (blocked-rotor) with the input angular frequency of ω:

$$R_1 + R_{add,BL} + R_{BL} = \frac{P_{BL}}{3I_{BL}^2}\,, \tag{5.15a}$$

$$X_{s\sigma} + X_{add,BL} + X_{BL} = \sqrt{(\frac{V_{BL}}{I_{BL}})^2 - (\frac{P_{BL}}{3I_{BL}^2})^2}\,. \tag{5.15b}$$

  where $Z_{BL} = R_{BL} + jX_{BL}$ is the impedance of the parallel circuit formed by R_c, $j\omega L_{sm}$ and $R'_R + j\omega L'_{R\sigma}$ in the blocked-rotor simulation.

However, the number of unknowns in above equations is higher than 4. Therefore, to derive the values of R'_R and $L'_{R\sigma}$, some simplifications are required:

1. As illustrated in Fig. 5.2, powers are consumed on R_1, R_c, R'_R and R_{add}. In the case of no-load simulation, due to the unknown R_{add}, there is no way to determine R_c from the power aspect. As $I_{c,NL}$ can be measured from the numerical simulation (see the end of section 5.2.1) and the stator current I_{NL}=$\sqrt{2}$ A is known, R_c can be determined from

$$|\frac{j\omega L_{sm}}{R_c + j\omega L_{sm}}| \cdot I_{NL} = I_{c,NL}\,. \tag{5.16}$$

   Theoretically, both R_c and L_c (as well as R_{cv} and L_{cv}) shall be included in the equivalent circuit (see Fig. 5.1). However, the determination of L_c requires additional information. For instance, with the phase difference α between $I_{c,NL}$ and I_{NL} (corresponding to the phase difference between $\underline{\hat{i}}^s_{c,s=0}$ and $\underline{\hat{i}}^s_{s,s=0}$ in Fig. 5.1) measured from the numerical model, L_c and R_c can be determined from

$$\frac{j\omega L_{sm}}{R_c + j\omega L_c + j\omega L_{sm}} = \frac{I_{c,NL}}{I_{NL}} e^{i(\pi-\alpha)}\,. \tag{5.17}$$

   Since both R_c and L_c are unknown, their solutions derived from (5.17) are very sensitive to α, which however cannot be measured accurately in the numerical

model. Therefore, the conventional engineering strategy is adopted here to neglect L_c and treat the impedance $R_c + j\omega L_c$ as purely active resistance [167]. Therefore L_c and $L_{c\nu}$ are missing in Fig. 5.2.

2. Slips corresponding to the ν^{th} (ν=5, 7, 11...) space harmonic are $s_\nu = (1-\nu)+\nu\cdot s$ (if the harmonic is forward rotating) or $s_\nu = (1+\nu)-\nu\cdot s$ (if the harmonic is backward rotating) [167]. In the case of s=0, s_5 and s_7 are 6 and -6, respectively. At s=1, all the slips equal to 1. In the no-load or blocked-rotor simulation, depending on s_ν, the value of X_{add} varies. However, at a specific ω, the variation of X_{add} with s_ν is negligible and $X_{s\sigma} + X_{add}$ can be assumed constant. This simplification is based on the following consideration. As per [167] , $L'_{R\sigma\nu}$ is close to $L'_{R\sigma}$ and $R'_{R\nu}$ is close to R'_R. Meanwhile, the magnetizing reactance $X_{sm\nu}$ (or the differential leakage inductance $L_{sm\nu}$=$X_{sm\nu}/\omega$) is proportional to $(k_{w\nu}/\nu)^2$ [167], where $k_{w\nu}$ is the winding factor for the ν^{th} harmonic. For the employed distributed full-pitch windings, max$\{k_{w\nu}\}$ is around 0.2 and much smaller than the fundamental k_w. Therefore, the maximum $L_{sm\nu}$ (occurring at ν=5) is about $L_{sm}/100$. As per values derived in Table 5.1, $L'_{R\sigma\nu}$ is much larger than $L_{sm\nu}$. Therefore, the value of X_{add} changes very slightly with s_ν.

   With R_c determined from (5.16) and L_{sm} assumed, $X_{s\sigma} + X_{add,BL} = X_{s\sigma} + X_{add,NL}$ can be determined from (5.14b). Substituting it into (5.15b), X_{BL} is obtained.

3. Since $R_{c\nu}$ is unknown, the value of $R_{add,BL}$ may be different from that of $R_{add,NL}$. Therefore, the determination of R_{BL} in (5.15a) requires additional information. At s=1, the 3-phase copper loss on the rotor ($3I^2_{R,BL}R'_R$) equals to $T_{BL}\cdot\omega$ [164] where ω is known and T_{BL} is available in the numerical simulation. Besides, the 3-phase copper loss on the stator iron is $3I^2_{c,BL}R_c$, where R_c is determined from (5.16) and $I_{c,BL}$ is obtained from the numerical model. Hence, (5.15a) can be transformed to

$$3(R_1 + R_{BL})I^2_{BL} = P_{BL} - 3R_{add}I^2_{BL} = T_{BL}\cdot\omega + 3R_1 I^2_{BL} + 3R_c I^2_{c,BL}\,, \tag{5.18}$$

   and R_{BL} therefore can be obtained.

Since the obtained $R_{BL} + jX_{BL}$ is the impedance of the parallel circuit formed by $R_c + j\omega L_c$, $j\omega L_{sm}$ and $R'_R + j\omega L'_{R\sigma}$, rotor quantities (i.e, R'_R and $L'_{R\sigma}$) can be easily calculated. Parameters derived in the last column of Table 5.1 and those in Table 5.2 are based on the same numerical model. Their difference in R'_R is about 4.1% and the difference in $L'_{R\sigma}$ is about 3.2%.

Above, rotor quantities are determined from the state of s=1, where the (electrical) slip angular frequency $\Delta\omega = s\cdot\omega$ equals to ω. To check variations of determined circuit parameters with $\Delta\omega$, both the field distribution-based and the electrical measurements-based methods are implemented with a series of input frequencies. Since L_{sm} is identified from $|\underline{\hat{\lambda}}^{s'}_{R,s=0}|$ which is independent of ω, it keeps constant. Variations of R'_R and $L'_{R\sigma}$ are illustrated in Fig. 5.3. In the electrical measurement-based methods, L_{sm} is always assumed to be 7.3 mH [170]. Since L_{add} depends on the input angular frequency ω, $L_{s\sigma} + L_{add}$ applied to each block-rotor simulation shall be obtained from their corresponding no-load simulations. It is interesting to note that R_c obtained from each no-load simulation also varies with ω. This variation is due to the neglected L_c.

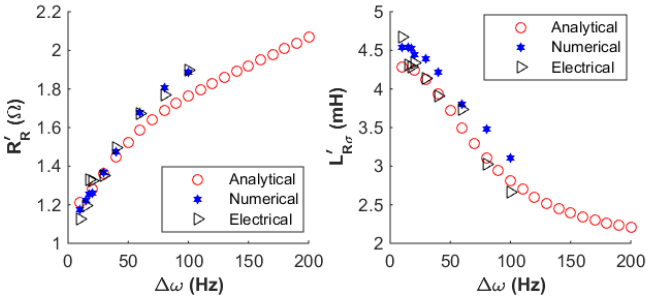

Figure 5.3: R'_R and $L'_{R\sigma}$ determined through the analytical/numerical field models and electrical measurements.

In Fig. 5.3, the increase of R'_R and the decrease of $L'_{R\sigma}$ are caused by the skin effect [170]. Instead of evenly distributed in the cross-section of Region II, eddy currents tend to concentrate in the upper layer when the slip frequency increases. The non-uniform distribution of eddy currents results in the increase of R'_R. Meanwhile, compared to currents flowing in the bottom layer, currents distributed in the upper layer link with less leakage flux which means a low leakage inductance. Therefore, $L'_{R\sigma}$ decreases when the slip frequency increases.

In Fig. 5.3, deviations between parameters derived from the analytical/numerical field models and those derived from electrical measurements are mainly caused by the neglected L_c and the resultantly overestimated R_c, as well as measurement errors. As illustrated in Fig. 5.1, L_c exists and connects serially to R_c. In the no-load simulation, when ω increases, more currents will flow through R_c since the reactance $X_{sm} = \omega L_{sm}$ increases. However, due to the existence of L_c, the increase of $I_{c,NL}$ is not as large as expected. Therefore, R_c derived from (5.16) is larger than its actual value. As per (5.18), the overestimated R_c leads to an overestimated R_{BL}. As a result, R'_R derived from the overestimated R_{BL} is slightly larger than its actual value while $L'_{R\sigma}$ is slightly smaller than its actual value. Hence, R'_R derived from electrical measurements increases faster while $L'_{R\sigma}$ decreases faster than those derived from the analytical/numerical field models. Their deviations become larger at high slip frequencies.

5.2.3. STEADY STATE TORQUE-SPEED CURVE

If there are no stator eddy currents, output torques of the reaction sphere (with the pole-pair number p=1) in steady states can be expressed as:

$$T = \frac{3}{2}\frac{R'_R|\hat{\underline{i}}^{sr}_R|^2}{s\cdot\omega} = \frac{1.5L^2_{sm}|\hat{\underline{i}}^{s}_s|^2 R'_R/\Delta\omega}{(R'_R/\Delta\omega)^2 + (L'_{R\sigma}+L_{sm})^2}\,. \tag{5.19}$$

As illustrated by (5.19), torques generated by the current-controlled induction machine depend on the slip angular frequency $\Delta\omega$ rather than the input angular frequency or the mechanical speed. Applying circuit parameters derived in the 3^{rd} column of Table 5.1 and the controlled input $|\hat{\underline{i}}^{s}_s|$=2 A to (5.19) results in the steady state torque-speed curve (the solid line) in Fig. 5.4. This curve predicts how much driving torques are gen-

erated when the actuator is running at different slip frequencies.

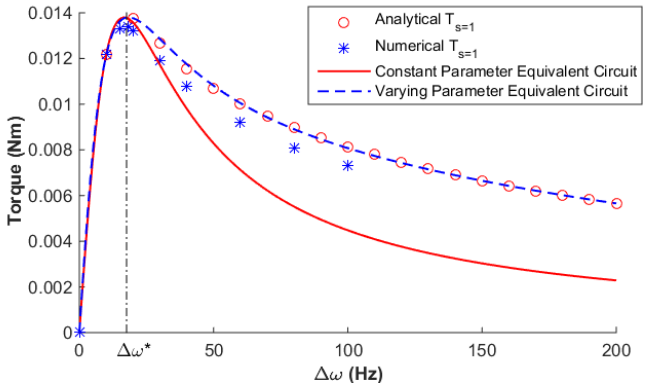

Figure 5.4: Steady state torque-speed curve of the single axis rotation.

To check the prediction accuracy, steady state torque-speed curves obtained from the analytical field model and numerical simulations are presented in Fig. 5.4 too. Firstly, due to the relation of $\Delta\omega = s \cdot \omega$, the value of $\Delta\omega$ can be adjusted by varying the slip s or the input angular frequency ω. Since torques at s=1 can be calculated through the analytical field model directly, applying the fixed s=1 and various ω to (4.53) results in a series of analytically calculated $T_{s=1}$ in Fig. 5.4. In numerical simulations, the same strategy (fixed s=1 and varying ω) is adopted. This is because the spinning rotor in COMSOL is modeled through a moving mesh which makes time-dependent simulations even slower. Therefore, the numerical $T_{s=1}$ data set is obtained from simulations with various input frequencies and it is shown in Fig. 5.4 too.

Secondly, for an induction motor, its stable operation region is $\Delta\omega \in [0, \Delta\omega^*]$, where $\Delta\omega^*$ corresponds to the slip frequency where the maximum torque T^* occurs. When the equivalent circuit model is employed for torque prediction, its prediction accuracy within the stable operation region is more concerned rather than outside the region. As illustrated in Fig. 5.4, deviations between torques predicted from the equivalent circuit model (i.e., through equation (5.19)) and those obtained from (4.53) or numerical simulations become larger when $\Delta\omega$ increases. Within the stable operation region, maximum deviations occur at $\Delta\omega^*$. At this point, the torque (i.e., T^*) predicted from the equivalent circuit model deviates from the analytical and numerical $T_{s=1}$ by only 0.3% and 3%, respectively.

Differences between the analytically calculated $T_{s=1}$ and those from numerical simulations are mainly due to stator eddy currents in the numerical model. Although high order space harmonics affect the numerical $T_{s=1}$ too, their influences at s=1 are negligible [164]. At the end of section 5.2.1, the magnitude of induced stator eddy currents is quantified. If that part is subtracted from the stator input current in the analytical model, the resultant analytical $T_{s=1}$ would match the numerical $T_{s=1}$ well. In conventional induction machines, stator eddy currents can be suppressed by employing laminated steel. However, in the spherical machine, to ensure the high permeability of magnetic paths

along with multiple directions, it is challenging to suppress unwanted eddy currents.

Deviations between the analytical $T_{s=1}$ curve and the torque-speed curve predicted by the equivalent circuit are caused by varying R'_R and $L'_{R\sigma}$. To illustrate the influence, variations of R'_R and $L'_{R\sigma}$ are approximated by curve fitting. Applying L_{sm}=7.3 mH, curve fitted R'_R and $L'_{R\sigma}$ to (5.19) results in the dashed line in Fig. 5.4, which fits the analytical $T_{s=1}$ curve well.

As presented above, the equivalent circuit model with constant circuit parameters predicts the achievable maximum torque T^* with reasonable accuracy. Based on (5.19), the achievable maximum torque of the single-axis rotation (with p=1) occurs at

$$\Delta\omega^* = R'_R/(L_{sm}+L'_{R\sigma})\,, \tag{5.20}$$

and its value is

$$T^* = 0.75L_{sm}^2|\hat{i}_R^{s\prime}|^2/(L_{sm}+L'_{R\sigma})\,. \tag{5.21}$$

5.3. VERIFICATION THROUGH EXPERIMENTAL DATA

5

The studied reaction sphere illustrated in chapter 4 is a basic design. Its performance analysis method, including field modeling and circuit parameter determination, is generally applicable to induction-based spherical actuators. Below, the developed performance analysis method is validated through an experimental case presented in [20]. In that case, a spherical conductive rotor is driven by a pair of inductors to perform single-axis rotations. A single inductor is with 6 slots, spanning 60° along $\vec{e}_\phi$ and 35° along $\vec{e}_\theta$. With slots handled by the Carter factor [171] and end effects neglected, the two inductors are approximated as one-third of a complete 6-pole-pair 3-phase slot-less winding set. The distribution of generated magnetic flux is solved by the analytical model presented in chapter 4. Due to the equivalent pole-pair number p_e=6 of the complete winding set, the approximated stator surface current density changes to $J_s\cos(\omega t-6\phi)/\sin\theta$.

Based on the flux density distribution at s=0 and s=1 with the input frequency of 25 Hz, equivalent circuit parameters are determined. Torques generated by the inductors are calculated through (5.19) multiplied by the factual pole-pair number p=2. Given the specific input stator current $|\underline{\hat{i}}_s^s|$ ($1.6\times\sqrt{2}$ A [20]), steady state torque-speed curves of the actuator can be predicted. In [20], torque measurements were conducted for two scenarios, where the rotor conductive layer is copper (W.Nr.2.0090 [172]) or the Cu-Zn-Sn alloy (W.Nr.2.0532). In both experimental scenarios, the rotor core is made of St-37 steel (SAE 1013) which has high relative permeability (μ_r=2000). Equivalent circuit parameters determined through the proposed method for the copper rotor and the ally rotor are listed in Table 5.3.

Predicted and experimental torque-speed curves (with the input frequency of 25 Hz) are compared in Fig. 5.5 and Fig. 5.6. Their differences are mainly due to longitudinal end effects since transverse end effects have been taken into account by the analytically modeled eddy currents distribution.

Torques caused by longitudinal end effects are calculated by applying L_{sm}, R'_R and $L'_{R\sigma}$ to the linear inductor model developed in [173]. They are added to torques predicted from the equivalent circuit model, resulting in modified torque-speed curves which are illustrated in Fig. 5.5 and Fig. 5.6 too. In both figures, the mean absolute percentage error between the modified torque-speed curve (with end effects) and the corresponding

Table 5.3: Equivalent circuit parameters for the copper rotor and the ally rotor

	Param	Copper	Cu-Zn-Sn alloy
Inputs	σ	4.3×10^7 S/m	1.3×10^7 S/m
	R_s	51.1 mm (considering the Carter factor)	
	R_r	50 mm	
	R_b	49 mm	
	ψ	72.5°	
	μ_r	2000	
	k_w	0.955	
	f	25 Hz (electrical input frequency)	
	p_e	6 (equivalent pole-pair number)	
	p	2 (factual pole-pair number)	
	N	180 (per phase per pole)	
Outputs	L_{sm}	0.0490 H	0.0490 H
	R'_R	37.87 Ω	125.2 Ω
	$L'_{R\sigma}$	0.00621 H	0.00628 H

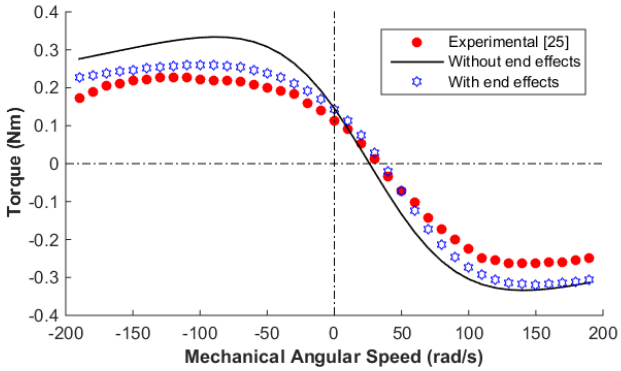

Figure 5.5: Steady state torque-speed curve of the copper rotor.

experimental data is within 23%. Notable deviations in the generating mode are caused by simplifications in the modeling of entry and exit waves [173], which become invalid when the slip is negative. To the best of the author's knowledge, how to accurately model end effects is still a challenge in the field of linear and rotary inductors. For a specific design (with specific geometry parameters, supplied with a specific input frequency and running at a specific speed), the study of end effects can be conducted through FEM simulations. However, the torque generated by end effects changes with the input frequency and the rotor moving speed, as well as geometry parameters. Here, the end effect model

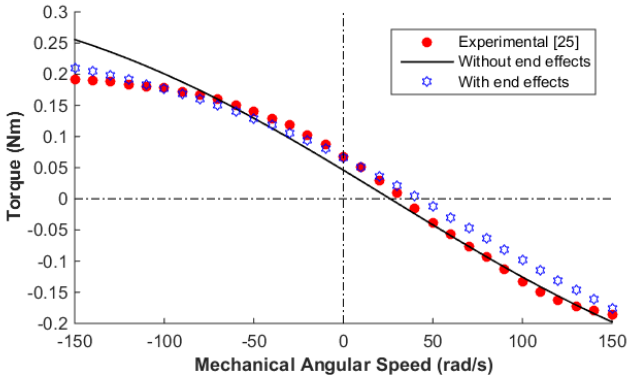

Figure 5.6: Steady state torque-speed curve of the Cu-Zn-Sn rotor.

presented in [173] is adopted for its acceptable accuracy.

5.4. OPTIMIZATION OF THE INDUCTION-BASED DRIVING UNIT

In this thesis, the reaction sphere is designed for applications on small spacecraft. To implement fast slew maneuvers, a large maximum torque (T^*) is desired. Meanwhile, due to limited power budgets, a low power consumption of the reaction sphere is demanded. In this study, copper loss on the stator windings (P_1) is formulated analytically. Optimization of the reaction sphere is conducted to maximize the ratio of T^*/P_1. Copper loss on the rotor and the output mechanical power are not included in the optimization since they vary with the reaction sphere's operation state. Calculations and minimizations of hysteresis loss, iron loss, frictions and windage losses (in ground tests) are beyond the scope of this study.

Based on (5.21), T^* is reformulated since L_{sm}, R'_R and $L'_{R\sigma}$ are determined through (5.8)-(5.12):

$$T^* = \frac{1}{2} \frac{|\underline{\hat{\lambda}}'_{R,s=0}|^2}{\sqrt{|\underline{\hat{\lambda}}'_{R,s=0}|^2 - |\underline{\hat{\lambda}}'_{R,s=1}|^2}} \frac{|T_{s=1}|}{|\underline{\hat{\lambda}}'_{R,s=1}|} . \tag{5.22}$$

Because $|\underline{\hat{\lambda}}^{s'}_{R,s=0}|$,$|\underline{\hat{\lambda}}^{s'}_{R,s=1}|$ and $T_{s=1}$ are calculated through the flux density distribution which depends on design variables of the reaction sphere, T^* can be further expressed as a function of design variables.

To restrict dimensions of the reaction sphere, the inner radius of the stator back iron (i.e., R_s) is set to its maximum limit and keeps constant in the optimization. To enhance the coupling between the rotor and the stator, the physical air gap width g=R_s-δ_w-R_r (where δ_w is the radial thickness of stator windings) and the angle ψ in Fig. 4.1 are set to their minimum values. The toroidal stator windings are wound in the regular pattern and opposite windings are connected in series. The filling factor is assumed $K_u = 0.4$. Parameters and design variables involved in the optimization are listed in Table 5.4. Since equation (5.22) illustrates that T^* is independent from ω, a random input angular frequency ω is adopted in the maximization of T^*.

Table 5.4: Parameters and Variables in the Optimization

	Param	Value	Note
Constant	R_s	30 mm	Limited by volume budget
	ψ	65°	Limited by assembly issues
	p	1	A high synchronous speed is desired
	μ_r	30	Unchanged material
	K_u	0.4	Round wires are adopted [167]
	g	0.5 mm	physical air gap width, limited by assembly tolerances
	l	72 mm	Wire length per turn (toroidally wound)
	k_w	0.96	Winding distribution factor
	ω	20π rad/s	For circuit parameters determination
Variables	d		Diameter of the conductive wire
	N		Turn number per phase per pole
	s_1		$s_1 = R_b/R_s$
	s_2		$s_2 = R_r/R_s$
	i_k		Input stator current density (peak value)

5.4.1. COPPER LOSS ON STATOR WINDINGS P_1

For simplification, we assume the space for stator windings to be filled by copper with a fill factor K_u, windings per phase per pole occupies an area of $\pi/6 \cdot \left(R_s^2 - (R_r+g)^2\right)$. The turn number per phase per pole is then

$$N = 2K_u R_s^2 \left(1-(s_2+g_s)^2\right)/(3d^2)\,, \tag{5.23}$$

where g_s=g/R_s=1/60.

Since coils are serially connected per phase, the stator resistance per phase is $R_1 = \rho 2Nl/(\pi d^2/4)$, where ρ is the resistivity of copper wires. Given the stator current density $I_s = \pi d^2 i_k/4$, the copper loss on stator windings is

$$P_1 = \frac{3}{2} I_s^2 R_1 = \frac{\pi}{2} \rho l i_k^2 K_u R_s^2 \left(1-(s_2+g_s)^2\right)\,. \tag{5.24}$$

5.4.2. EQUATIONS OF T^*

In the field modeling, energized stator windings are approximated as surface current density. Replacing (5.23) and I_s to the calculation of J_s results in:

$$|J_s| = 3NI_s k_w/(\pi R_s) = 0.5 k_w i_k R_s K_u \left(1-(s_2+g_s)^2\right)\,. \tag{5.25}$$

Based on (5.25), distributions of B_r and B_ϕ are formulated as functions of design

variables. With Φ_{rp} calculated through (5.7), rotor flux linkages become:

$$|\hat{\underline{\lambda}}^{s\prime}_{R,s=0}| = k_w^2 i_k N K_u \left[1-(s_2+g_s)^2\right] R_s^3 (|\sum_{n=1}^{\infty} G_{b,n}(s_1)| + |\sum_{n=1}^{\infty} G_{r,n}(s_1,s_2)|) \,, \tag{5.26a}$$

$$|\hat{\underline{\lambda}}^{s\prime}_{R,s=1}| = k_w^2 i_k N K_u \left[1-(s_2+g_s)^2\right] R_s^3 (|\sum_{n=1}^{\infty} F_{b,n}(s_1,s_2)| + |\sum_{n=1}^{\infty} F_{r,n}(s_1,s_2)|) \,. \tag{5.26b}$$

$T_{s=1}$ is calculated through the Maxwell stress tensor on the rotor surface:

$$|T_{s=1}| = \frac{k_w^2 i_k^2 K_u^2 s_2^3 R_s^5}{2\mu_0} \left[1-(s_2+g_s)^2\right]^2 |\sum_{n=1}^{\infty} Z_n(s_1,s_2)| \,. \tag{5.27}$$

Complete expressions of G, F and Z are provided in the Appendix.

To simplify the equation of T^*, convergence studies are conducted for $G_{b,n}(s_1)$, $G_{r,n}(s_1,s_2)$, $F_{b,n}(s_1,s_2)$, $F_{r,n}(s_1,s_2)$ and $Z_n(s_1,s_2)$ respectively. Instead of infinite orders, only the first 13 orders are included. Resultantly, (5.22) turns to (5.28)

$$T^*(s_1,s_2) = \frac{1}{4\mu_0} \frac{k_w^2 i_k^2 K_u^2 \left[1-(s_2+g_s)^2\right]^2 s_2^3 R_s^5 \left(|\sum_{n=1}^{13} G_{b,n}(s_1)| + |\sum_{n=1}^{13} G_{r,n}(s_1,s_2)|\right)^2}{\sqrt{\left(|\sum_{n=1}^{13} G_{b,n}(s_1)| + |\sum_{n=1}^{13} G_{r,n}(s_1,s_2)|\right)^2 - \left(|\sum_{n=1}^{13} F_{b,n}(s_1,s_2)| + |\sum_{n=1}^{13} F_{r,n}(s_1,s_2)|\right)^2}} \cdot \frac{|\sum_{n=1}^{13} Z_n(s_1,s_2)|}{\left(|\sum_{n=1}^{13} F_{b,n}(s_1,s_2)| + |\sum_{n=1}^{13} F_{r,n}(s_1,s_2)|\right)} \,. \tag{5.28}$$

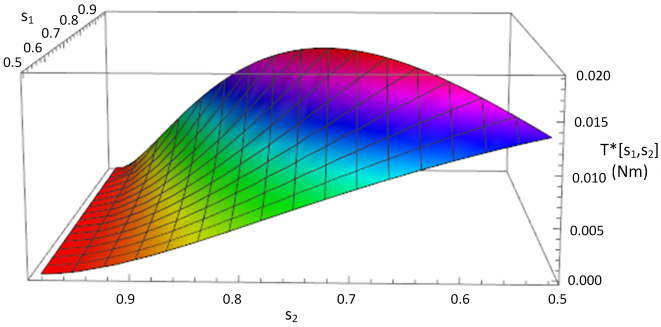

Figure 5.7: The variation of $T^*(s1,s2)$.

T^* is proportional to i_k^2 while being independent of d and N. Actually, K_u is affected by d and N slightly but their influences are neglected by setting K_u to a constant. With i_k= $5\sqrt{2}\times 10^6$ A/m^2, the variation of $T^*(s1,s2)$ over the range of $s_1 \in [0.5, 2.95/3]$ and $s_2 \in [s_1+0.02, 2.95/3]$ is shown in Fig. 5.7 and colored by the T^* value. It is clear that a smaller thickness of Region II (i.e., s_1-s_2) leads to a larger T^*. Here, the constraint of s_2-$s_1 \geq 0.02$ is to avoid numerical errors. The maximum T^* occurs at s_1^*=0.68, s_2^*=0.70

and $T^*(s_1^*, s_2^*)$ is about 18.9 mNm. The slip frequency corresponding to T^* is calculated through

$$\Delta\omega^*(s_1, s_2) = \frac{R'_R}{L'_{R\sigma} + L_m} = \frac{|\hat{\underline{\lambda}}^{s'}_{R,s=1}| \cdot \omega}{\sqrt{|\hat{\underline{\lambda}}^{s'}_{R,s=0}|^2 - |\hat{\underline{\lambda}}^{s'}_{R,s=1}|^2}} . \tag{5.29}$$

Given s_1^*=0.68 and s_2^*=0.70, $\Delta\omega^*(s_1^*, s_2^*)$ is about 119 Hz.

5.4.3. VALIDATION OF THE DERIVED T^*

To check whether s_1^* and s_2^* provide the maximum T^*, three sets of parameters (i.e., s_1=0.66/0.68/0.70 and s_2=s_1+0.02) are examined. They are applied to the analytical field model (in section II) where torques for specific input ω are calculated through the Maxwell stress tensor rather than predicted by the equivalent circuit. For each set of s_1 and s_2, the analytical model is executed with various ω, to search for the actual maximum torque T^*_{act} and its corresponding $\Delta\omega^*_{act}$.

Table 5.5: Found and Predicted T^* and $\Delta\omega^*$

	T^*_{act}	$\Delta\omega^*_{act}$	T^*(error%)	$\Delta\omega^*$(error%)
s_1=0.66 s_2=0.68	18.84 mNm	137 Hz	18.8 mNm (<1%)	128.3 Hz (≈6%)
s_1=0.68 s_2=0.70	18.95 mNm	128 Hz	18.9 mNm (<1%)	119.2 Hz (≈7%)
s_1=0.70 s_2=0.72	18.87 mNm	119 Hz	18.8 mNm (<1%)	110.5 Hz (≈7%)

Both the found and predicted T^* and $\Delta\omega^*$ are presented in Table 5.5. Their differences are mainly due to variations of R'_R and $L'_{R\sigma}$. As we can see, the proposed optimization model (based on parameters determined at ω=20π rad/s) provides a reliable prediction of $T^*(s_1, s_2)$. Predicted $\Delta\omega^*(s_1, s_2)$ are close to their actual values. The optimized variables (s_1^*=0.68 and s_2^*=0.70) actually provide the largest T^*.

5.4.4. OPTIMIZATION WITH RESPECT TO T^*/P_1

Since maximizing T^* and minimizing P_1 are independent optimization objectives, they are combined together through weighting factors to determine the value of s_1 and s_2. In this project, the optimized reaction sphere will be applied to a micro-satellite which has a mass of between 50 to 100 kg. Its power budget is not as limited as that of a nanosatellite. Meanwhile, its inertia is not as limited as that of a nanosatellite, which means its required control torque should not be too small. Therefore, the weighting factors are set to $\alpha_1 = \alpha_2 = 1$. Given (5.28) and (5.24), the variation of $T^*(s_1, s_2)/P_1(s_2)$ over the range of $s_1 \in [0.5, 2.95/3]$ and $s_2 \in [s_1+0.02, 2.95/3]$ is presented in Fig. 5.8 and colored by the T^*/P_1 value.

The maximum $T^*(s1, s2)/P_1(s_2)$ achieves 1.474 mNm/W, occurring at s_1=0.83 and s_2=0.85. Compared to the original design where s_1=2/3 and s_2=2.5/3, this ratio is improved by 115%. As per (5.28) and (5.24), improving K_u, k_w and R_s or reducing the length

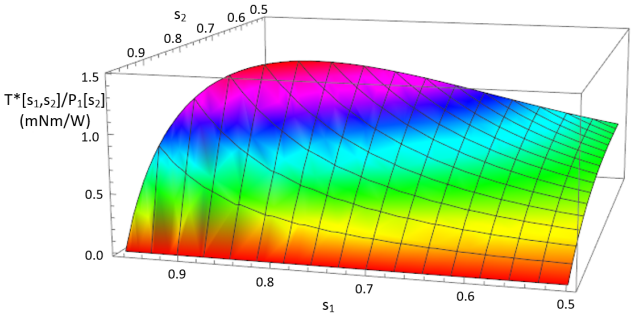

Figure 5.8: The variation of $T^*(s1, s2)/P_1(s_2)$.

of end windings helps to increase the ratio of T^*/P_1.

Actually, the developed performance model allows optimizations with respect to other objectives as well. For instance, with the predicted T^* and $\Delta\omega^*$, the maximum copper loss on the rotor can be calculated. It can be used to check the thermal constraint.

5.5. SUMMARY

In this chapter, the performances of an induction-based reaction sphere are analyzed through the equivalent circuit approach. Involved circuit parameters are determined through analytically solved magnetic field distributions. In this way, researchers can quickly evaluate the performances of newly designed actuators. Compared to numerical simulations and experiments on prototypes, the performance analysis method provides the steady state torque-speed curve of single-axis rotations in seconds, greatly saving time and cost. Besides, it can be generally applied to spherical induction-based actuators. For more advanced scenarios such as the experimental case above, the developed basic models shall be extended by taking additional factors into account.

6

MOTION COUPLING OF INDUCTION-BASED REACTION SPHERES

6.1. INTRODUCTION

The concept of induction-based reaction spheres initiates from the superposition law of vector fields. Since torques generated by each winding set are about different axes, the rotor shall be able to perform multi-dimensional rotations when multiple winding sets are energized. However, in practice, the resultant torque is affected by couplings between windings, overlapping magnetic fields, as well as the misalignment between the rotor's spin axis and the magnetic field's revolving axis. Additionally, due to difficulties in torque measurements on spherical actuators, the generated torque or performances of multi-dimensional rotations are rarely studied.

In [31], a spherical rotor surrounded by six linear inductors was developed. Each inductor was controlled like a conventional induction motor through the rotor flux field-oriented control. The thrust force generated by each inductor was assumed acting at the center of the inductor and along the longitudinal direction of the inductor. No couplings were considered. In [21], 2D numerical simulations of a spherical conductive rotor driven by two orthogonal winding sets were presented. It was found that generated thrust forces were fluctuating and lower in amplitude than those generated by conventional induction machines. In [15], performances of a reaction sphere driven by three stators were investigated through FEM simulations. When the rotation axis of the rotor was not aligned with that of the revolving magnetic field, a resistant torque was generated in addition to the expected driving torque. To take the resistant torque into account, torque models were developed through the surface fitting of FEM results obtained through Ansys Maxwell.

The content of this chapter will be submitted as a scientific paper titled *Motion Coupling Characteristics of Induction-Based Spherical Actuators*.

Similar couplings exist in other multi-dimensional induction machines. For instance, a linear-rotary 2D induction motor was studied in [27, 29]. The rotor was a cylinder while the stator was composed of two parts: one part excited rotary motions and the other excited the traveling field along the axial direction. Both electromagnetic coupling between the two stator parts [174] and motion coupling between the linear-rotary motion [175] were observed and investigated through 3D FEM. Due to end effects, the magnetic field excited by one stator segment extended to the area covered by the other stator segment and induced voltages. As per [28], voltages inducted in the orthogonally placed unenergized 3-phase windings were unbalanced. As a result, no stable disturbance torques or thrust forces were generated. The additional resistant torque generated by the normal speed component of the rotor with respect to the excited magnetic field was formulated as $B \cdot v_n$, where B is proportional to the excited magnetic flux density and v_n represents the normal speed component of the rotor [27, 32].

In an induction-based reaction sphere, the moving conductor-eddy currents problem is more complex. Different from the linear-rotary 2D machine, local velocities on the spherical surface vary with the location. Therefore, the torque model presented in [32] becomes inapplicable. To predict driving torques and resistant torques influenced by motion coupling in the reaction sphere design with ball bearings presented in section 3.4, an innovative analysis approach is proposed in this chapter. Although a large number of designs of induction-based reaction sphere have been proposed in literature and stator windings can be placed in different ways, a basic winding configuration is studied here and a general torque model is derived. Since the developed torque model is generally applicable to induction-based spherical actuators, it can be used to evaluate various designs.

6.2. PROBLEM DESCRIPTION

For an induction-based reaction sphere, the resultant torque acting on the rotor is not a simple superposition of torques provided by each winding set for various reasons.

Firstly, the resultant torque is affected by electromagnetic couplings between stator windings. Even if different winding sets do not overlap with each other, the magnetic field excited by one winding set could extend to the area covered by another winding set and induce voltages in it. As per [28], when magnetic fields excited by different winding sets travel along mutually orthogonal directions, voltages induced by the electromagnetic coupling are unbalanced and will not result in stable thrust forces.

Secondly, the resultant torque is affected by the coupling caused by the unaligned spin axes, which is referred to as motion coupling in this dissertation. When the spin axis of the rotor is not aligned with that of the excited revolving magnetic field, the driving torque which is about the revolving field's spin axis is smaller than expected [15, 175] and an additional resistant torque which is orthogonal to the revolving field's spin axis is generated [15, 21].

This chapter focuses on the study of motion coupling while electromagnetic coupling is neglected. This is because in the induction-based reaction sphere presented in section 3.4, three sets of stator windings are placed mutually orthogonal. As per [28], disturbances caused by electromagnetic coupling in such cases are not stable and can be neglected.

To simplify the analysis of motion coupling, this study concerns the case where only one set of AC windings is energized. Fig. 6.1 illustrates the structure of the induction-based reaction sphere and its simplified geometry. The conductive rotor is spinning about a specific axis $\vec{e}_r$ with a fixed velocity Ω. The energized winding set is placed about the z-axis in the inertial coordinate frame Γ. The Cartesian coordinate system of frame Γ is defined through a triad of mutually orthogonal base vectors $\vec{x}$, $\vec{y}$ and $\vec{z}$. A corresponding FEM model is developed in COMSOL through the Rotating Machinery, Magnetic physics interface. Relevant parameters are same as those listed in Table 4.1 and Table 4.2 except for the removed PMs.

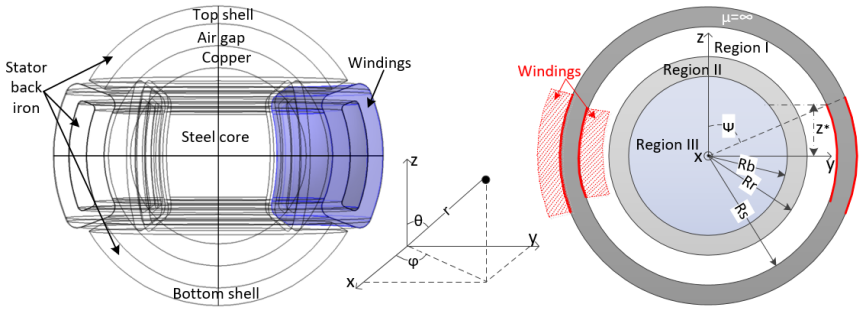

Figure 6.1: A basic structure of an induction-based spherical actuator and its simplified geometry.

6

In Chapter 4, the electromagnetic field excited by the energized winding set in blocked-rotor states has been modeled analytically. Energized stator windings are approximated as sinusoidally distributed surface currents at R_s. With the obtained flux density distribution within the actuator, torques acting on the rotor can be calculated through the Maxwell stress tensor. However, for arbitrary-axis rotations, the situation becomes different. For instance, in the study case here, the rotor is spinning at a velocity Ω about $\vec{e}_r$ in the inertial frame Γ. For a random conductor segment whose spatial vector is $\vec{r}$ on the rotor, its moving velocity is $\vec{v} = \Omega\vec{e}_r \times \vec{r}$. Since eddy currents are induced by both the time-dependent electromagnetic field and the moving conductor in the field, the governing equation for the rotor conductive region becomes

$$\nabla^2 \vec{A} = \mu_0 \mu_{r,c} \sigma \left(\frac{\partial \vec{A}}{\partial t} - \vec{v} \times (\nabla \times \vec{A}) \right), \tag{6.1}$$

or

$$\nabla^2 \vec{B} = \mu_0 \mu_{r,c} \sigma \left(\frac{\partial \vec{B}}{\partial t} - \nabla \times (\vec{v} \times \vec{B}) \right). \tag{6.2}$$

As per analysis presented in Chapter 5, when the rotor's spin axis is aligned with that of the revolving magnetic field, the governing equation can be simplified to

$$\nabla^2 \vec{A} = \mu_0 \mu_{r,c} \sigma \left(\frac{\partial \vec{A}}{\partial t} - \vec{v} \times (\nabla \times \vec{A}) \right) \approx j \mu_0 \mu_{r,c} \sigma (\omega - p\Omega) \vec{A}\,. \tag{6.3}$$

In cases where the rotor's spin axis deviates from that of the revolving magnetic field, the simplification in (6.3) becomes invalid. Additionally, the varying local velocity $\vec{v}$ on the spherical rotor surface makes (6.1) or (6.2) even more difficult to solve.

Rather than directly solving (6.1) or (6.2), an alternative approach to analyzing the moving conductor-eddy currents problem is to transfer the relative velocity from the rotor to the energized stator winding set. In the transferred scenario, the rotor is stationary while the energized AC winding set is revolving at the velocity Ω about the direction $\vec{e}_w = -\vec{e}_r$. Since the relative movement between the rotor and the revolving magnetic field is unchanged, torques exposed onto the rotor shall be the same. In the transferred scenario, the rotor conductive region will be governed by the heat diffusion equation rather than (6.1) or (6.2). However, the challenge in this approach is the modeling of stator currents. The winding set energized with 3-phase AC currents is revolving. If energized windings are approximated as surface currents, rotations of spherical harmonics will be involved and the approximated surface currents can not be simply formulated. Therefore, in the transferred problem, the governing equation is simplified but the formulation of boundary conditions becomes challenging.

Therefore, when the rotor is performing arbitrary-axis rotations, the torque calculation through analytically modeled flux density distribution within the actuator is difficult. Besides, since the revolving magnetic field and the rotor's movement may induce eddy currents flowing along multiple directions, the equivalent circuit of conventional induction machines becomes inapplicable.

6.3. TORQUE MODELING

In the torque modeling approach presented below, the spinning rotor-eddy current problem is transferred to the problem where the rotor is stationary while energized stator windings are revolving. As stated at the end of section 6.2, formulating the movement of revolving 3-phase AC windings is challenging. The solution proposed here is to focus on magnetic poles rather than the entire magnetic field.

Assumption 1: Electromagnetic forces act at magnetic poles inducted on the rotor surface.

Since the magnetic flux is distributed within the entire actuator and eddy currents are induced in the entire conductive region, electromagnetic forces actually act on the entire rotor. However, at magnetic poles induced on the rotor, the magnetic flux density achieves its maximum on the spherical surface. As per Maxwell's stress tensor or Lorentz force law, the resultant force distribution therefore also achieves its maximum at these rotor poles. Here, based on the study results of single-axis rotations presented in Chapter 5, electromagnetic forces acting on the entire rotor body are assumed acting on magnetic poles whose movement can be formulated simply.

6.3.1. TRACK OF INDUCED MAGNETIC POLES

Locations of magnetic poles induced on the rotor are determined through locations of stator magnetic poles. The movement of stator poles is composed of two rotations which are analyzed individually in the following. To describe these rotations, two reference frames are introduced first:

- $\mathscr{B}$ is the reference frame attached to the stationary rotor. Its Cartesian coordinate system is defined through mutually orthogonal unit vectors $\vec{x}_b$, $\vec{y}_b$ and $\vec{z}_b$. The spherical coordinate system of $\mathscr{B}$ is defined through unit vectors $\vec{r}_b$, $\vec{\theta}_b$ and $\vec{\phi}_b$. $[x^b, y^b, z^b]$ and $[r^b, \theta^b, \phi^b]$ are Cartesian and spherical coordinates of $\mathscr{B}$, respectively. Since the rotor is stationary, the frame $\mathscr{B}$ coincides with the frame Γ.
- $\mathscr{W}$ is the reference frame attached to the revolving winding set. Its Cartesian coordinate system is defined through mutually orthogonal unit vectors $\vec{x}_w$, $\vec{y}_w$ and $\vec{z}_w$. $[x^w, y^w, z^w]$ are Cartesian coordinates of $\mathscr{W}$.

Initially, the two frames $\mathscr{B}$ and $\mathscr{W}$ are aligned (see Fig. 6.2). Their origins coincide at all times. To generalize the torque model, the stator winding's transverse center is placed at the inclination angle θ_w in Fig. 6.2. For the design corresponding to Fig. 6.1, θ_w is $\pi/2$.

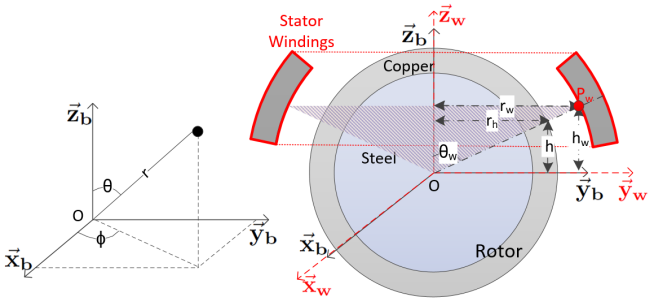

Figure 6.2: The rotor-fixed and the winding-fixed frames in a generalized geometry.

When the winding set energized with AC currents is stationary, stator magnetic poles are revolving in the winding frame. With L_{sm}, R'_R and $L'_{R\sigma}$ obtained from the study of single-axis rotations and the given ω (which equals to $\Delta\omega$ since the rotor is stationary), the azimuthal phase lag ξ between the stator pole and the induced rotor pole can be determined by

$$\xi = \arctan \frac{\Delta\omega(L_{sm} + L'_{R\sigma})}{R'_R} . \tag{6.4}$$

Assumption 2: Stator magnetic poles are located at the energized windings' transverse center.

When the winding set is energized with DC currents and is revolving about $\vec{e}_w$ in the stationary frame $\mathscr{B}$, stator magnetic poles will be located at fixed positions in the frame $\mathscr{W}$. The transverse width of stator windings is neglected such that stator poles can be approximated as points rather than areas. Eddy currents are induced on the rotor to prevent the change of enclosed flux. Due to the electromagnetic induction, the induced rotor poles can not catch up with the stator poles. This lead to a phase lag η between the induced rotor pole and the stator pole [142].

Although an induction-based spherical actuator may have a pole-pair number of p, the movement of only one pole point (which is named P_w for the stator magnetic pole and P for the corresponding induced rotor pole) will be analyzed below. Movements of other pole points can be obtained in the same way as P_w and P.

If the input angular frequency of the 3-phase AC winding set is ω, the position of P_w in the frame $\mathscr{W}$ will be revolving at the mechanical speed ω_m=ω/p:

$$\begin{bmatrix} x^w_{P_w} & y^w_{P_w} & z^w_{P_w} \end{bmatrix}^{\mathrm{T}} = \begin{bmatrix} r_w\cos(\omega_m t+\epsilon_0) & r_w\sin(\omega_m t+\epsilon_0) & h_w \end{bmatrix}^{\mathrm{T}}, \tag{6.5}$$

where r_w=$R_s\sin\theta_w$, h_w=$R_s\cos\theta_w$ and ϵ_0 defines the initial position of P_w.

Due to the phase lag ξ caused by electromagnetic induction, the induced rotor pole is located at P_m

$$\begin{bmatrix} x^w_{P_m} & y^w_{P_m} & z^w_{P_m} \end{bmatrix}^{\mathrm{T}} = \begin{bmatrix} r_h\cos(\omega_m t-\xi+\epsilon_0) & r_h\sin(\omega_m t-\xi+\epsilon_0) & h \end{bmatrix}^{\mathrm{T}}, \tag{6.6}$$

where r_h=$R_r\sin\theta_w$ and h=$R_r\cos\theta_w$.

The rotation of frame $\mathscr{W}$ is described by Euler's eigen-axis rotation. Since $\vec{e}_w$ keeps its relative orientation unchanged both with respect to $\mathscr{B}$ and $\mathscr{W}$, it is defined as the eigen-axis:

$$\vec{e}_w = e_1\vec{x}_b + e_2\vec{y}_b + e_3\vec{z}_b = e_1\vec{x}_w + e_2\vec{y}_w + e_3\vec{z}_w\,. \tag{6.7}$$

The rotation matrix is defined as

$$\begin{bmatrix} \vec{x}_w & \vec{y}_w & \vec{z}_w \end{bmatrix} = \begin{bmatrix} \vec{x}_b & \vec{y}_b & \vec{z}_b \end{bmatrix} \mathbf{C}_\alpha\,, \tag{6.8}$$

where $\mathbf{C}_\alpha$ is given in (6.9).

$$\mathbf{C}_\alpha = \begin{bmatrix} \cos\alpha+e_1^2(1-\cos\alpha) & e_2e_1(1-\cos\alpha)-e_3\sin\alpha & e_3e_1(1-\cos\alpha)+e_2\sin\alpha \\ e_1e_2(1-\cos\alpha)+e_3\sin\alpha & \cos\alpha+e_2^2(1-\cos\alpha) & e_3e_2(1-\cos\alpha)-e_1\sin\alpha \\ e_1e_3(1-\cos\alpha)-e_2\sin\alpha & e_2e_3(1-\cos\alpha)+e_1\sin\alpha & \cos\alpha+e_3^2(1-\cos\alpha) \end{bmatrix}, \tag{6.9}$$

where α=Ωt. In this dissertation, we study the case where the winding set is revolving at a stable speed Ω.

Coordinates of P_m in the stationary frame $\mathscr{B}$ are

$$\begin{bmatrix} x^b_{P_m} & y^b_{P_m} & z^b_{P_m} \end{bmatrix}^{\mathrm{T}} = \mathbf{C}_{\Omega t} \begin{bmatrix} r_h\cos(\omega_m t-\xi+\epsilon_0) & r_h\sin(\omega_m t-\xi+\epsilon_0) & h \end{bmatrix}^{\mathrm{T}}. \tag{6.10}$$

Due to the phase lag η caused by electromagnetic induction, the induced rotor pole P is located at

$$\begin{bmatrix} x^b_P & y^b_P & z^b_P \end{bmatrix}^{\mathrm{T}} = \mathbf{C}_{(\Omega t-\eta)} \begin{bmatrix} r_h\cos(\omega_m t-\xi+\epsilon_0) & r_h\sin(\omega_m t-\xi+\epsilon_0) & h \end{bmatrix}^{\mathrm{T}}. \tag{6.11}$$

The value of η is calculated similarly as for ξ, and corresponding circuit parameters will be discussed in section 6.3.4.

To facilitate the following analysis, another reference frame $\mathscr{R}$ with a virtual winding set is introduced. It is obtained by rotating the energized stator winding set and the winding-fixed reference frame $\mathscr{W}$ backward with the angle η. Therefore, frame $\mathscr{R}$ keeps rotating with $\mathscr{W}$ but having a fixed phase lag η. The Cartesian coordinate system of $\mathscr{R}$ is defined through mutually orthogonal unit vectors $\vec{x}_r$, $\vec{y}_r$ and $\vec{z}_r$, with $[x^r, y^r, z^r]$ being the corresponding Cartesian coordinates. The spherical coordinate system of $\mathscr{R}$ is defined through unit vectors $\vec{r}_r$, $\vec{\theta}_r$ and $\vec{\phi}_r$, with $[r^r, \theta^r, \phi^r]$ being the corresponding spherical polar coordinates.

6.3.2. SLIP FREQUENCY

The time derivative of the location of P in the $\mathscr{B}$ frame provides its moving speed on the rotor surface. The mechanical moving speed $\vec{v}_{P,mech}$ can be separated into two components: along the longitudinal and transverse directions of the virtual winding set respectively:

$$\vec{v}_{P,mech} = v_{P,l}\vec{e}_{l,P} + v_{P,t}\vec{e}_{t,P} \,. \tag{6.12}$$

Unit vectors of the longitudinal and transverse directions of the winding set at point P in the frame $\mathscr{B}$ are referred to as $\vec{e}_{l,P}$ and $\vec{e}_{t,P}$. They are obtained by transferring $\vec{\phi}_{r,P}$ and $\vec{\theta}_{r,P}$ at point P in the frame $\mathscr{R}$ to the frame $\mathscr{B}$:

$$\vec{e}_{l,P} = \mathbf{C}_{(\Omega t-\eta)}\vec{\phi}_{r,P} \,, \tag{6.13a}$$

$$\vec{e}_{t,P} = \mathbf{C}_{(\Omega t-\eta)}\vec{\theta}_{r,P} \,. \tag{6.13b}$$

If the energized winding set has a pole-pair number of p, the change rate of flux density will be p times that of the mechanical moving speed. The electrical moving speed of the induced rotor pole represents the flux change rate and

$$\vec{v}_P = p \cdot v_{P,l}\vec{e}_{l,P} + v_{P,t}\vec{e}_{t,P} \,. \tag{6.14}$$

Angular velocities along the longitudinal and transverse directions are $p \cdot v_{P,l}/r_h$ and $v_{P,t}/R_r$, respectively. Slip frequencies along the longitudinal and transverse directions are

$$\Delta\omega_l = p \cdot v_{P,l}/r_h \,, \tag{6.15a}$$

$$\Delta\omega_t = v_{P,t}/R_r \,. \tag{6.15b}$$

6.3.3. TORQUE CALCULATION

Electromagnetic torques of induction machines are generated by the Lorentz force acting on rotor eddy currents. In the equivalent circuit analysis method of conventional induction machines (where rotor quantities are referred to the stator side for the case that the air gap flux is in the center), the generated torque is expressed as [166]

$$\vec{T}_e = \frac{3}{2}p(\vec{i}_R^{s\prime} \times \vec{\lambda}_R^{s\prime}) \,. \tag{6.16}$$

Since the secondary field excited by rotor eddy currents changes the primary field excited by stator currents, the referred rotor flux linkage is

$$\vec{\lambda}_R^{s\prime} = L'_{R\sigma}\vec{i}_R^{s\prime} + L_{sm}\left(\vec{i}_s^{s} + \vec{i}_R^{s\prime}\right) = L_{sm}\vec{i}_s^{s} + L'_R\vec{i}_R^{s\prime} \,, \tag{6.17}$$

where L'_R is the referred total rotor inductance.

In the induction-based reaction sphere, the challenge of employing (6.16) to calculate the generated electromagnetic torque is how to determine $\vec{i}_R^{s\prime}$ and $\vec{\lambda}_R^{s\prime}$. Additionally, the two vectors are restricted by the voltage equation

$$\vec{u}_R^{s\prime} = R'_R\vec{i}_R^{s\prime} + \frac{\mathrm{d}\vec{\lambda}_R^{s\prime}}{\mathrm{d}t} \,, \tag{6.18}$$

where $\vec{u}_R^{s\prime}$ is the referred rotor voltage and has a zero magnitude. Since the direction of $\vec{\lambda}_R^{s\prime}$ is the direction of the maximum flux density in the rotor conductive region, $\vec{\lambda}_R^{s\prime}$ points in the radial direction at point P.

Eddy currents induced on the rotor can be separated into two components: $i_{r,t}$ and $i_{r,l}$. The eddy current $i_{r,t}$ flows along the transverse direction of the virtual winding set and generates torques against $\Delta\omega_l$. The eddy current $i_{r,l}$ flows along the longitudinal direction of the virtual winding set and generates torques against $\Delta\omega_t$. Both eddy currents change the magnetic flux density excited by the stator currents. To determine the magnitude of $\vec{\lambda}_R^{s\prime}$, a vector diagram is illustrated in Fig. 6.3:

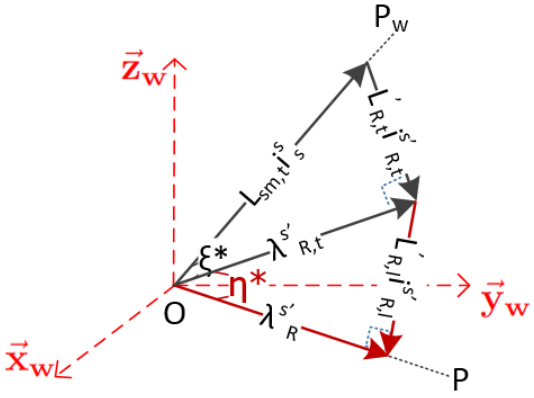

Figure 6.3: Determination of the resultant rotor flux linkage $\lambda_R^{s\prime}$.

1. Firstly, flux linkage of $i_{r,l}$ is not considered. Effects brought by $\Delta\omega_l$ are analyzed through the equivalent circuit of conventional induction machines. Rotor currents, voltages and flux linkages are referred to the stator side through

$$\vec{i}_R^{s\prime} = \frac{N_{re}}{N_{se}}\vec{i}_r \; ; \; \vec{u}_R^{s\prime} = \frac{N_{se}}{N_{re}}\vec{u}_r \; ; \; \vec{\lambda}_R^{s\prime} = \frac{N_{se}}{N_{re}}\vec{\lambda}_r \tag{6.19}$$

where N_{se} and N_{re} are effective stator and rotor turn numbers, respectively. Referred rotor quantities are with the subscript R and the superscript prime. The superscript s refers to the stator side.

The flux linkage $\vec{\lambda}_{R,t}^{s\prime}$ generated by $\vec{i}_s^s$ and $\vec{i}_{R,t}^{s\prime}$ is:

$$\vec{\lambda}_{R,t}^{s\prime} = L_{sm,t}\vec{i}_s^s + L'_{R,t}\vec{i}_{R,t}^{s\prime} \, . \tag{6.20}$$

The approximated stator pole P_w locates on the direction of $\vec{i}_s^s$.

Since the rotor voltage is zero, and due to the relation of $\mathrm{d}\vec{\lambda}_{R,t}^{s\prime}/\mathrm{d}t = j\Delta\omega_l\vec{\lambda}_{R,t}^{s\prime}$, (6.18) is converted to:

$$0 = R'_{R,t}\vec{i}_{R,t}^{s\prime}/\Delta\omega_l + j\vec{\lambda}_{R,t}^{s\prime} \, , \tag{6.21}$$

which means $\vec{\lambda}^{s\prime}_{R,t}$ is orthogonal to $\vec{i}^{s\prime}_{R,t}$. Fig. 6.3 illustrates how the phase lag ξ^* is introduced. From (6.21), the value of ξ^* is derived

$$\xi^* = \arctan \frac{\Delta\omega_l L'_{R,t}}{R'_{R,t}} . \tag{6.22}$$

The angle of ξ^* is not directly related to ξ given in (6.4). In subsection 6.3.1, ξ is estimated by assuming it is independent from Ω and the eigen-axis $\vec{e}_w$. However, ξ^* is affected by ω, Ω and $\vec{e}_w$ through $\Delta\omega_l$.

In Chapter 5, single-axis rotations of the induction-based reaction sphere have been studied and only eddy currents flowing in the transverse direction are considered. Since the direction of $i_{r,t}$ is along $\vec{\theta}_r$ in the frame $\mathscr{R}$, circuit parameters (i.e., $L_{sm,t}$, $L'_{R\sigma,t}$ and $R'_{R,t}$) equal to those determined in Chapter 5. As illustrated in Fig. 5.3, R'_R and $L'_{R\sigma}$ vary with the slip frequency. In calculating ξ^*, values of $R'_{R,t}$ and $L'_{R\sigma,t}$ shall be taken from their variation curves, as per the slip frequency.

2. Secondly, flux linkage of $i_{r,l}$ is taken into account. The magnetic flux density distribution excited by $\vec{i}^s_s$ and $\vec{i}^{s\prime}_{R,t}$ is further changed by $\vec{i}^{s\prime}_{R,l}$. The resultant referred rotor flux is

$$\vec{\lambda}^{s\prime}_R = \vec{\lambda}^{s\prime}_{R,t} + L'_{R,l}\vec{i}^{s\prime}_{R,l} . \tag{6.23}$$

The induced rotor pole P is located in the direction of $\vec{\lambda}^{s\prime}_R$. Due to the zero rotor voltage and the relation of $\mathrm{d}\vec{\lambda}^{s\prime}_{R,l}/\mathrm{d}t = j\Delta\omega_t\vec{\lambda}^{s\prime}_{R,l}$, the resultant rotor flux linkage $\vec{\lambda}^{s\prime}_R$ is orthogonal to $\vec{i}^{s\prime}_{R,l}$

$$0 = R'_{R,l}\vec{i}^{s\prime}_{R,l}/\Delta\omega_t + j\vec{\lambda}^{s\prime}_R . \tag{6.24}$$

The angle η^* is quantified through

$$\eta^* = \arctan \frac{\Delta\omega_t L'_{R,l}}{R'_{R,l}} . \tag{6.25}$$

Similarly as for ξ^*, η^* is not directly related to η. Determination of circuit parameters $L_{sm,l}$, $L'_{R\sigma,l}$ and $R'_{R,l}$ is discussed in section 6.3.4.

Due to the relation of $\mathrm{d}\vec{\lambda}^{s\prime}_R/\mathrm{d}t = j\Delta\omega\vec{\lambda}^{s\prime}_R$ and the zero rotor voltage, the resultant rotor flux linkage $\vec{\lambda}^{s\prime}_R$ is orthogonal to $\vec{i}^{s\prime}_R$. As per (6.24), $\vec{\lambda}^{s\prime}_R$ is also orthogonal to $\vec{i}^{s\prime}_{R,l}$. Therefore, $\vec{i}^{s\prime}_{R,t}$ which can be expressed as a combination of $\vec{i}^{s\prime}_R$ and $\vec{i}^{s\prime}_{R,l}$ is orthogonal to $\vec{\lambda}^{s\prime}_R$, too.

The force generated by $\vec{i}^{s\prime}_{R,t}$ at the rotor pole P is along $\vec{e}_{l,P}$

$$\vec{F}_{l,P} = \frac{1.5p|\vec{i}^{s\prime}_{R,t}\times\vec{\lambda}^{s\prime}_R|}{2\cdot p\cdot r_h}\vec{e}_{l,P} = \frac{1.5p|\vec{i}^{s\prime}_{R,t}|\cdot|\vec{\lambda}^{s\prime}_R|}{2\cdot p\cdot r_h}\vec{e}_{l,P} . \tag{6.26}$$

As per Fig. 6.3, $|\vec{\lambda}^{s\prime}_R| = |\vec{\lambda}^{s\prime}_{R,t}|\cos\eta^*$. Additionally, $1.5p|\vec{i}^{s\prime}_{R,t}|\cdot|\vec{\lambda}^{s\prime}_{R,t}|$ is the torque generated by single-axis rotations, whose magnitude in steady states can be expressed as [159]

$$T_c = \frac{1.5pL^2_{sm,t}|\vec{i}^s_s|^2 R'_{R,t}/\Delta\omega_l}{(R'_{R,t}/\Delta\omega_l)^2 + L'^2_{R,t}} . \tag{6.27}$$

Therefore, the force generated by $\vec{i}^{s\prime}_{R,t}$ at the rotor pole P can be converted to

$$\vec{F}_{l,P} = \frac{T_c \cos\eta^*}{2 \cdot p \cdot r_h} \cdot \vec{e}_{l,P} \,. \tag{6.28}$$

Similarly, the force $\vec{F}_{t,P}$ generated by $\vec{i}^{s\prime}_{R,l}$ at the rotor pole P is along $\vec{e}_{t,P}$

$$\vec{F}_{t,P} = \frac{1.5p|\vec{i}^{s\prime}_{R,l}| \cdot |\vec{\lambda}^{s\prime}_{R}|}{2 \cdot p \cdot r_h} \cdot \vec{e}_{t,P} \,. \tag{6.29}$$

Due to $|\vec{i}^{s\prime}_{R,l}| = |\vec{\lambda}^{s\prime}_{R,t}| \sin(\eta^*)/L'_{R,l}$ from Fig. 6.3 and $\vec{\lambda}^{s\prime}_{R,t} = R'_{R,t}\vec{i}^{s\prime}_{R,t}/\Delta\omega_l$, the expression of $\vec{F}_{t,P}$ can be written as

$$\vec{F}_{t,P} = \frac{T_c \cos(\eta^*)\sin(\eta^*) R'_{R,t}}{\Delta\omega_l L'_{R,l} \cdot (2 \cdot p \cdot r_h)} \cdot \vec{e}_{t,P} \,. \tag{6.30}$$

To facilitate torque calculation, forces generated at point P are decomposed into components along $\vec{x}_b$, $\vec{y}_b$ and $\vec{z}_b$ in the stationary frame $\mathscr{B}$

$$\vec{F}_P = F_{x,P} \cdot \vec{x}_b + F_{y,P} \cdot \vec{y}_b + F_{z,P} \cdot \vec{z}_b \,, \tag{6.31}$$

where

$$F_{i,P} = (\vec{F}_{l,P} + \vec{F}_{t,P}) \cdot \vec{i}_b \,, \ (i = x, y, z.) \tag{6.32}$$

Since electromagnetic forces are acting at induced rotor poles, the resultant total torque formulated in the stationary frame $\mathscr{B}$ is:

$$\vec{T}^B = \sum_{i=0}^{2p-1} (\vec{P}_j \times \vec{F}_{P_j}) \,, \tag{6.33}$$

where j is the index of rotor poles.

Above, electromagnetic torques acting on the stationary rotor have been calculated for the transferred problem. However, in the original problem, the rotor is spinning while stator windings are stationary. So, for the original problem, electromagnetic torques acting on the rotor shall be expressed in the winding fixed frame $\mathscr{W}$ and

$$\begin{bmatrix} T_x & T_y & T_z \end{bmatrix}^{\mathrm{T}} = \mathbf{C}^{-1}_{\Omega t} \begin{bmatrix} T^B_x & T^B_y & T^B_z \end{bmatrix}^{\mathrm{T}} \,. \tag{6.34}$$

6.3.4. EQUIVALENT CIRCUIT PARAMETERS CORRESPONDING TO $\Delta\omega_t$

To determine $L_{sm,l}$, $L'_{R\sigma,l}$ and $R'_{R,l}$, a series of numerical simulations where $\vec{e}_r$ is orthogonal to the energized winding's axial direction, are conducted. Concerning the basic configuration presented in Fig. 6.1, its numerical simulations are conducted in COMSOL. The 3-phase winding placed about the z-axis in the inertial frame Γ is energized with direct current (I_A=2 A,I_B=I_C=1 A) so that the stator pole P_w locates on the x-axis. This is to ensure the slip frequency about the z-axis is zero (i.e, $\Delta\omega_l$=0) while $\Delta\omega_t$=Ω. Frame Γ is the reference frame by default when numerical models are considered. The rotor is set to be rotating about the y-axis with a stable velocity Ω. Fig. 6.4 illustrates resistant torques T_r about the y-axis, which are obtained through numerical simulations.

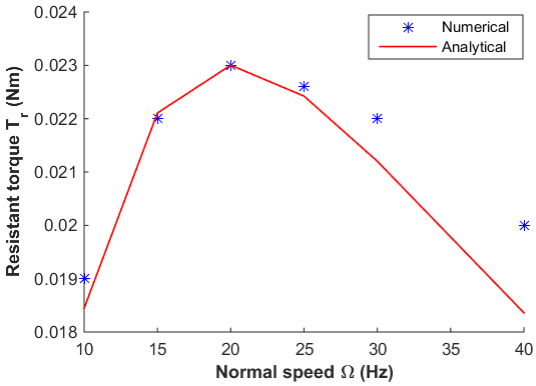

Figure 6.4: The resistant torque T_r varies with the normal revolving speed Ω when $\Delta\omega_l$ is zero.

Regardless of how transverse end effects influence the resistant torque T_r, the torque-speed relation of conventional current-controlled induction machines is utilized to describe the relation between T_r and Ω. Similar to (6.27),

$$T_r = \frac{1.5L_{sm,l}^2|\vec{i}_s^s|^2 R'_{R,l}/\Omega}{(R'_{R,l}/\Omega)^2 + L'^2_{R,l}} . \tag{6.35}$$

Since the magnitude of main flux excited by stator windings $\vec{\lambda}_{sm}^s = L_{sm}\vec{i}_s^s$ is unchanged regardless of the rotor's spin axis, $L_{sm,l}$ equals to $L_{sm,t}$. As per (6.35), the maximum resistant torque occurs at

$$\Omega^* = R'_{R,l}/L'_{R,l} , \tag{6.36}$$

and its value is

$$T_r^* = \frac{3L_{sm,l}^2|\vec{i}_s^s|^2}{4L'_{R,l}} . \tag{6.37}$$

Both Ω^* and T_r^* are available in the numerically obtained torque-speed curve. With $L_{sm,l}$ known, $R'_{R,l}$ and $L'_{R,l}$ are derived from (6.36) and (6.37). For the basic configuration, $R'_{R,l}$=0.87 Ω and $L'_{R,l}$=-0.35 mH. Replacing them into (6.35) leads to the torque-speed curve in red in Fig. 6.4.

In Fig. 6.4, deviations between the numerical results and the corresponding analytical approximations increase with Ω. This is because the generation of the resistant torque is complex. Firstly, even if the generation of T_r can be described by (6.35), parameters $R'_{R,l}$ and $L'_{R,l}$ vary with Ω, as explained in Chapter 5 for Fig. 5.3. Similar to Fig. 5.4 in Chapter 5, when constant $R'_{R,l}$ and $L'_{R,l}$ are employed, the analytical expression cannot approximate the numerical results within the entire Ω range.

Secondly, the resistant torque is affected by transverse end effects whose influence is unclear. To the author's knowledge, there are no models available describing transverse end effects in cases where $\Delta\omega_t$ is non-zero. Here, equation (6.35) is employed to describe the resistant torque, and parameters $R'_{R,l}$ and $L'_{R,l}$ are determined through numerical Ω^*

and T_r^*. Since the numerical results are influenced by transverse end effects, the analytical approximation has already taken transverse end effects into account. Therefore, values of $R'_{R,l}$ and $L_{R,l}$ do not have practical meanings. Equations (6.36) and (6.37) specify the relations between $R'_{R,l}$, $L'_{R,l}$ and $L_{sm,l}$, so that these relations can be utilized in the calculation of η^* in (6.25) and $\vec{F}_{t,P}$ in (6.30).

From (6.36) and (6.37), only a constant value of $R'_{R,l}$ and $L_{R,l}$ can be determined. Furthermore, due to the defect brought by the separate analysis of $\Delta\omega_l$ and $\Delta\omega_l$ (which will be discussed in section 6.4.1), a close approximation of the numerical T_r is expected only for the low Ω range.

Concerning η involved in the position determination of P, it is calculated in a similar way as to ξ. In the transferred problem, $\Omega\cdot\vec{e}_w$ of the revolving winding set can be decomposed into $\Omega_\parallel$ and $\Omega_\perp$ which are parallel and normal to the z-axis of the inertial frame Γ. Since circuit parameters corresponding to $\Omega_\parallel$ and $\Omega_\perp$ are different, η can be calculated by

$$\eta = \alpha\cdot\arctan\frac{\Omega_\perp L'_{R,l}}{R'_{R,l}} + (1-\alpha)\cdot\arctan\frac{\Omega_\parallel L'_{R,t}}{R'_{R,t}}\,, \tag{6.38}$$

where $\alpha = |\Omega_\perp|/(|\Omega_\perp| + |\Omega_\parallel|)$.

6.3.5. TIME CONSTANTS

Equations (6.4) and (6.38) provide the ideal values of ξ and η for steady states of individual rotation cases. However, when the two rotations are combined, there are no steady states anymore. Since the magnetic flux can not be changed instantaneously, ξ and η are affected by the rotor time constant [176]:

$$\tau_t = L'_{R,t}/R'_{R,t}\,, \tag{6.39a}$$

$$\tau_l = L'_{R,l}/R'_{R,l}\,. \tag{6.39b}$$

For designs with p=1, the actual values of ξ and η are restricted by $tt = \min\{T_\Omega/4, T_\omega/4\}$, where T_Ω and T_ω are periods of Ω and ω, respectively. For example, assuming the winding set of the basic configuration is revolving about $\vec{y}_b$ in the stationary frame $\mathscr{B}$. The phase lag η increases when P_m moves from ϕ^b=1.5π to 2π and decreases when P_m moves from ϕ^b=0 to 0.5π.

Hence, ξ and η shall be corrected as:

$$\xi = (1-e^{-tt/\tau_t})\cdot\arctan\frac{\omega L'_{R,t}}{R'_{R,t}} \tag{6.40a}$$

$$\eta = (1-e^{-tt/\tau_l})\cdot\arctan\frac{\Omega L'_{R,l}}{R'_{R,l}}\,. \tag{6.40b}$$

6.4. VALIDATION OF THE TORQUE MODEL

Due to the difficulty of measuring 3-dimensional torques generated by a spherical actuator, torque models are usually validated indirectly through open-loop or closed-loop

tests [15, 175]. Based on the developed torque model, an inverse relationship can be derived which enables the calculation of required inputs from desired output torques. By feeding calculated control signals to the prototype [6, 15, 31, 45] and checking whether desired movements are followed or not, the developed torque and dynamic models of the actuator are validated simultaneously.

In this study, because of the absence of hardware prototypes, the developed torque model is validated through comparisons with numerical simulation results. In the numerical simulations, the rotor is spinning about a specific axis $\vec{e}_r$ in the inertial frame while the energized stator winding set placed about the z-axis is stationary.

6.4.1. THE BASIC DESIGN

The torque model developed in section 6.3 is applied to the basic design shown in Fig. 6.1. The corresponding numerical model is built in COMSOL and it is the same numerical model that has been mentioned in Chapter 4 with the PMs removed. The rotational speed of the rotor is Ω. Cartesian coordinates of the rotor spin axis $\vec{e}_r$ in the inertial frame Γ are given in the form $[x, y, z]$. The stator winding set is energized with the input angular frequency ω.

To validate the developed torque model thoroughly, the rotor spin axis is set to [0, -1, 0], $[0, -1/\sqrt{2}, 1/\sqrt{2}]$ and $[1/\sqrt{3}, -1/\sqrt{3}, 1/\sqrt{3}]$, respectively in the three test cases. As mentioned in section 6.3.3, circuit parameters corresponding to $\Delta\omega_l$ (i.e., $L_{sm,t}$, $L'_{R\sigma,t}$ and $R'_{R,t}$) equal to those determined in single-axis rotations. In Chapter 5, equivalent circuit parameters for single-axis rotations are determined at the slip frequency $\Delta\omega$=10 Hz. To keep the rotation about the z-axis within its stable operation region illustrated in Fig. 5.4, the speed difference $\omega - \Omega_{\parallel}$ is restricted within the range of 0 to 10 Hz. Since $\Omega_{\parallel}$ is zero in Case 1, ω is set to 10 Hz. As discussed in the later part of this subsection, the developed torque model provides acceptable accuracy only for a low speed range of $\Omega_{\perp}$. Therefore, the rotor speed Ω is also set to 10 Hz in the test cases.

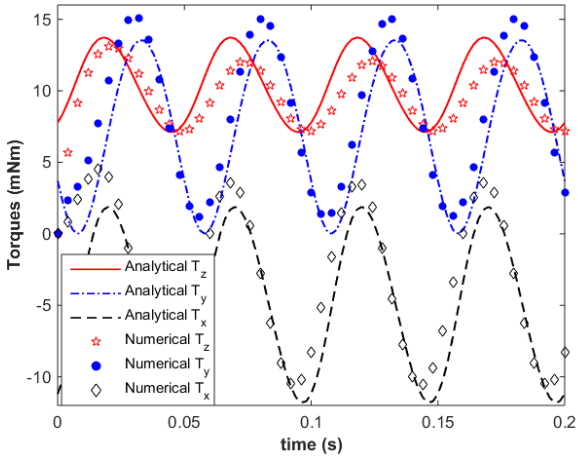

Figure 6.5: Comparison of analytical and numerical T_z, T_y and T_x generated in Case 1.

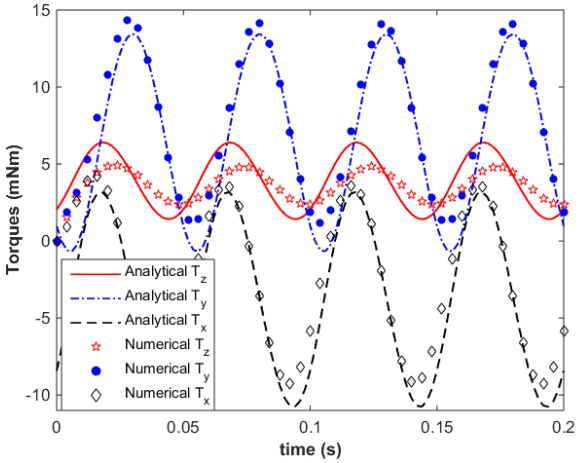

Figure 6.6: Comparison of analytical and numerical T_z, T_y and T_x generated in Case 2.

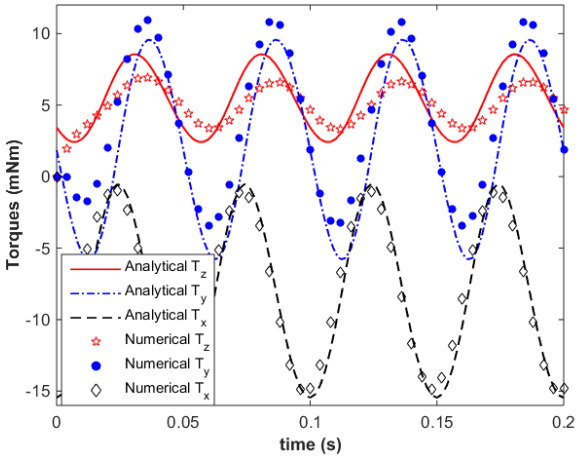

Figure 6.7: Comparison of analytical and numerical T_z, T_y and T_x generated in Case 3.

Analytical torques calculated from the developed torque model and corresponding numerical results are compared for each case and are illustrated in Fig. 6.5 to Fig. 6.7. As illustrated in these figures, in addition to the intended driving torque about the z-axis, disturbances are introduced by the motion coupling. Torques T_z, T_y and T_x fluctuate and their fluctuation magnitudes depend on ω, $\vec{e}_r$ and Ω. In practice, especially when the fluctuation frequency is high, mean torques are concerned and they are referred to as $\bar{T}$. In Table 6.1, analytically calculated values of $\bar{T}_{i,ana}$ $(i = x, y, z)$ in each case are compared to $\bar{T}_{i,num}$ $(i = x, y, z)$ obtained from corresponding numerical simulations. Numerical mean torques are obtained by averaging fluctuating torques over their stable

fluctuation periods, for instance, over the time range $t \in [0.1\,\text{s}, 0.2\,\text{s}]$ in the presented three cases.

Table 6.1: Comparison of mean torques in different cases.

Case	$\vec{e}_r$	Ω [Hz]	ω [Hz]	$\bar{T}_{z,num}$ [mNm]	$\bar{T}_{z,ana}$ [mNm]	error	$\bar{T}_{y,num}$ [mNm]	$\bar{T}_{y,ana}$ [mNm]	error	$\bar{T}_{x,num}$ [mNm]	$\bar{T}_{x,ana}$ [mNm]	error
1	[0, -1, 0]	10	10	9.64	10.38	7.66%	8.13	7.16	11.91%	-3.49	-4.95	41.63%
2	$[0, \frac{-1}{\sqrt{2}}, \frac{1}{\sqrt{2}}]$	10	10	3.59	3.89	8.33%	7.55	6.57	12.93%	-2.79	-3.86	38.60%
3	$[\frac{1}{\sqrt{3}}, \frac{-1}{\sqrt{3}}, \frac{1}{\sqrt{3}}]$	10	10	4.99	5.46	9.57%	3.72	2.04	45.13%	-8.00	-8.24	3.10%

DEVIATION OF T_x

In Table 6.1, $\bar{T}_{x,ana}$ deviates from $\bar{T}_{x,num}$ considerably in some cases. This is because the phase lag η is restricted by the top/bottom shells in the numerical model. In single-axis rotations, the existence of top/bottom shells facilitates the field modeling and torque calculation. However, in arbitrary-axis rotations, the transverse end effect brought by the top/bottom shells restricts the phase lag η. This phenomenon is illustrated in Fig. 6.8, where the distributions of B_r and induced eddy currents on the surface at r=24.5 mm at the time instant t=0.08 s in the numerical model with and without top/bottom shells in case 1 are compared. Torques generated in the two simulations are compared in Fig. 6.9. The absence of the top/bottom shells influences the torque generation from two aspects. Firstly, the generated $\bar{T}_z$ is much greater than that generated in Case 1 due to transverse edge effects and $\bar{T}_y$ is also affected. Secondly, since η is not restricted by the shells anymore, the generated T_x is more close to the analytically calculated T_x in Case 1. In Fig. 6.5 to Fig. 6.7, numerical results are obtained from the numerical model with top/bottom shells whose structure is illustrated in Fig. 6.1.

The restriction of top/bottom shells to η is not included in the analytical model. In the determination of $L_{sm,l}$, $L'_{R\sigma,l}$ and $R'_{R,l}$, since stator windings are energized with direct currents, only the resistant torque T_r is generated and T_r is independent from η.

In the studied cases, the magnetic field excited by stator windings is about the z-axis in frame Γ. Through the analysis presented in section 6.3, it is noticed that when the rotor's spin axis $\vec{e}_r$ has a zero component along the x-axis, T_x is purely caused by disturbance and its average is determined by η and the magnitude of $\vec{F}_{t,P}$. Therefore, T_x is influenced by the overestimated η most strongly. Since it fluctuates around zero, the deviation of $\bar{T}_{x,ana}$ from $\bar{T}_{x,num}$ could achieve 100% if the mean value is small enough. The deviation of $\bar{T}_{y,ana}$ from $\bar{T}_{y,num}$ in Case 3 is due to the same reason.

DEVIATION OF T_y

When the spin axis of the rotor $\vec{e}_r$ has a zero component along the x-axis, T_y is purely the resistant torque. Differences between the analytical and numerical results are mainly due to the following two reasons:

- The analytical model focuses on the change of magnetic poles rather than the entire magnetic field;

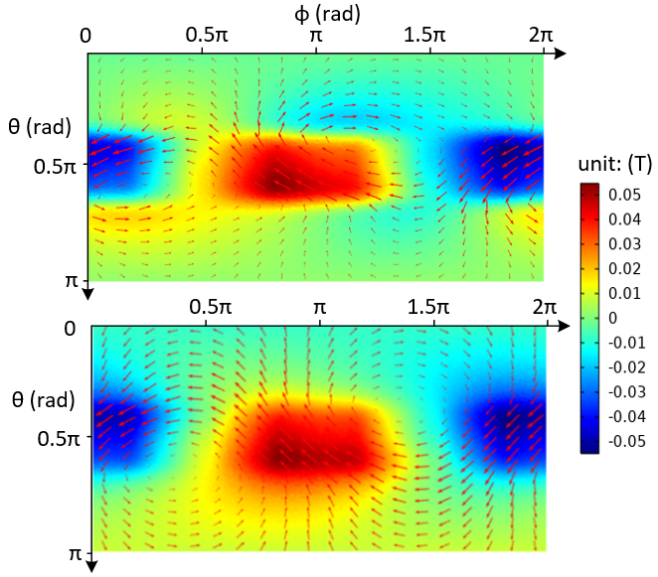

Figure 6.8: The distribution of B_r and induced eddy currents in numerical models with (upper) and without (lower) top/bottom shells in case 1.

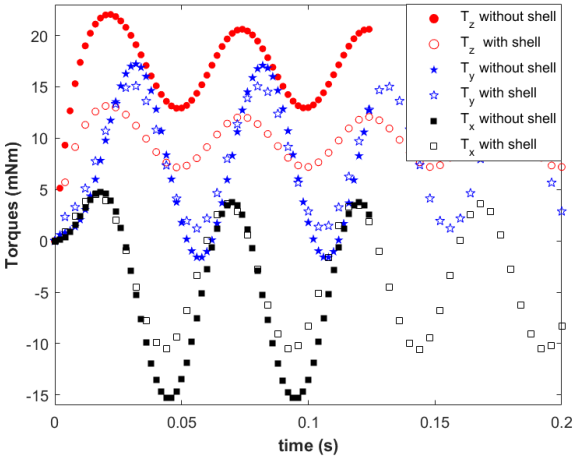

Figure 6.9: Influences of the top/bottom shells on T_z, T_y and T_x in case 1.

- Since influences brought by $\Delta\omega_l$ and $\Delta\omega_l$ are analyzed separately, the magnitude of the calculated rotor flux linkage $\vec{\lambda}_R^{s\prime}$ is smaller than its actual magnitude. As a result, both the magnitude of $\vec{F}_{l,P}$ and $\vec{F}_{t,P}$ are affected.

When $\vec{e}_r$ has a non-zero component along the x-axis, T_y is affected by the overestimated

η and fluctuates across zero, and the deviation of $\bar{T}_y$ is amplified.

DEVIATION OF T_z

The deviation of $\bar{T}_{z,ana}$ from $\bar{T}_{z,num}$ is lower than 10%. However, the fluctuations of $T_{z,ana}$ and $T_{z,num}$ have a notable phase difference. The phase difference comes from the magnitude deviation between analytical and numerical T_i^B $(i = x, y, z)$. Numerical T_i^B are obtained from the same numerical model by employing the material frame which is fixed to the material in the rotor body. Fig. 6.10 compares the analytical and numerical T_i^B generated in Case 2. As illustrated in the figure, their main differences lay on the magnitude and there are no obvious phase differences. However, when T_i^B are converted to T_i through (6.34), the phase of T_z is greatly affected by the inaccurate modeling of the magnitude of T_i^B.

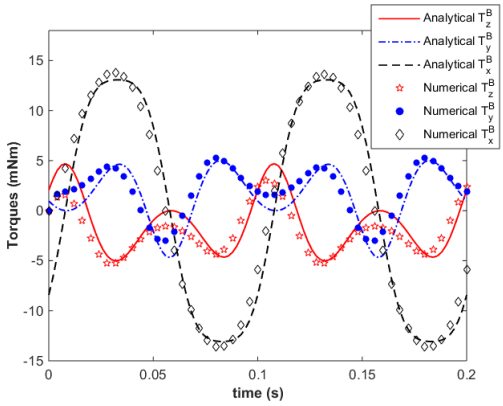

Figure 6.10: Comparisons of analytical and numerical T_z^B, T_y^B and T_x^B generated in Case 2.

6.4.2. APPLICATION TO AERS

For further validation, the developed torque model is applied to an aerostatic-bearing supported electrodynamic reaction sphere (AERS) presented in [15]. The AERS is composed of a conductive rotor, an aerostatic-bearing and three stators which are wound with AC windings. Energized stators excite revolving magnetic fields and drive the omnidirectional rotation of the rotor. The motion coupling studied in this dissertation is referred to as electromagnetic dynamic distortion effect (EDDE) and modeled by FEM in [15].

To validate the torque model developed in section 6.3, motion coupling involved in the case presented in Fig. 6.11 is investigated. Only the stator placed below the rotor is energized and it excites the magnetic field revolving about the z-axis. The rotor performs stable rotations about the x-axis. As defined in [15], the rotational speed about x-axis is n_v. Since the rotation speed about the z-axis n_r is zero (H. Zhou, personal communication, March 16, 2021), the input frequency of the energized stator equals to the slip frequency f_s. The input AC current has a constant RMS value $I_{\text{RMS}} = 3$ A.

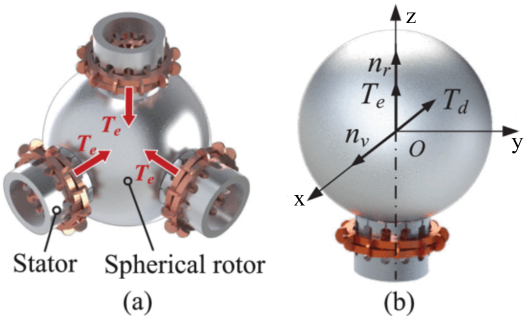

Figure 6.11: (a) AERS presented in [15]. (b) The study case for motion coupling analysis.

Equivalent circuit parameters of the AERS are obtained in the sequel. First, utilizing parameters of the AERS provided in Table 6.2, its magnetic field distribution and driving torque generated by a single stator in the blocked-rotor state are modeled through the method presented in Chapter 4. Energized stator windings are approximated as surface currents distributed within $\theta \in [\psi_1, \psi_2]$ on the inner stator surface. As per [15], an additional torque is produced by the transverse end effect and it varies with the input current frequency. To take the additional torque into account, the approximated values ψ_1 and ψ_2 are adjusted for each input frequency to fit its analytically calculated driving torque to the corresponding experimental result in [15].

Table 6.2: Design parameters of AERS [15]

Parameters	Value	Description
σ	1.92×10^7 S/m	Conductivity of the solid rotor
R_s	51 mm	Upper radius of the stator
R_r	50 mm	Radius of the rotor
r_1	15 mm	Inner radius of the stator iron core
r_2	20 mm	Outer radius of the stator iron core
k_w	0.933	Winding coefficient
p	1	Pole-pair number
N	92	Turn number per phase per pole

Based on the field model, equivalent circuit parameters of the AERS's single-axis rotation are derived from the method presented in Chapter 5. As illustrated in Fig. 6.12, derived equivalent circuit parameters vary with the input frequency. Since ψ_1 and ψ_2 are adjusted for each input frequency to approximate the transverse end effect, the calculated $L_{sm,t}$ is decreasing as the input frequency increases. The variation trends of $L'_{R\sigma,t}$ and $R'_{R,t}$ are similar to those presented in Fig. 5.3 and they are caused by the skin effect. The slight increase of $L'_{R\sigma,l}$ at the low-frequency range should be attributed to the calculation error involved in $L_{sm,t}$ and the measurement error involved in torques (during single-axis rotations) provided in [15].

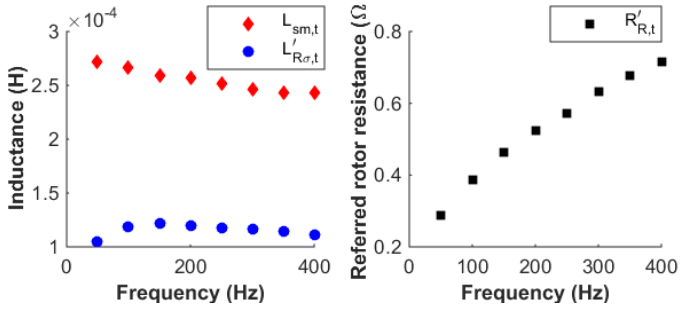

Figure 6.12: Varying equivalent circuit parameters for AERS.

The equivalent circuit parameters $L_{sm,l}$, $L'_{R\sigma,l}$ and $R'_{R,l}$ are obtained by curving fitting the resistant torque T_d generated at the zero f_s in FEM simulations. As discussed in section 6.4.1, transverse edge effects in designs without top/bottom shells have a major influence on the driving torque but little influence on the resistant torque. Therefore, $L_{sm,t}$ obtained at the input current frequency of 400 Hz is taken as $L_{sm,l}$. As a result, $L_{sm,l}$=0.243 mH, $L'_{R\sigma,l}$=0.084 mH and $R'_{R,l}$=0.069 Ω.

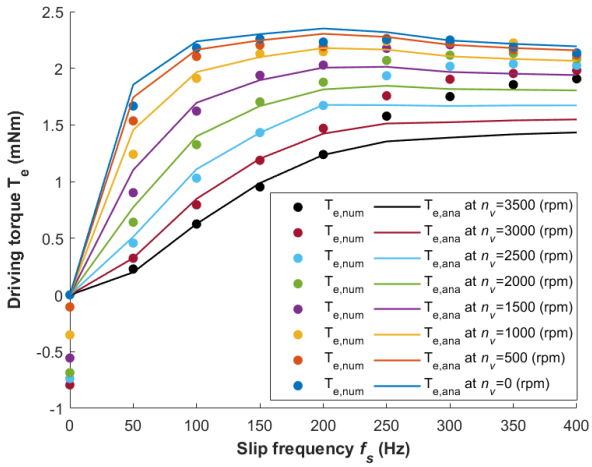

Figure 6.13: Comparison of the analytical and numerical driving torque T_e generated at different slip frequencies f_s and different normal speeds n_v.

Fig. 6.13 compares the analytical and numerical driving torque T_e (about the z-axis) generated by AERS at different slip frequencies f_s and different normal speeds n_v. The numerical results are provided in [15] and are obtained from FEM simulations conducted in Ansys Maxwell. At a low normal speed n_v, the analytical torque-speed curve T_e-f_s can match the corresponding numerical results well. When n_v increases, the peak of the numerical T_e-f_s curve does not decrease significantly and the slip frequency f_s corresponding to the peak increases. However, the T_e-f_s curve obtained from the analyt-

ical model has a notably decreasing peak value when n_v increases and the slip frequency f_s corresponding to the peak does not increase as fast as that in the numerical curves. As a result, deviations between the analytical and numerical T_e increase. The increasing deviation is believed attributed to two reasons:

- Circuit parameters $L_{sm,t}$, $L'_{R,t}$ and $R'_{R,t}$ do not constantly equal to those determined in single-axis rotations. They are influenced by eddy currents induced by the normal speed.
- In section 6.3, influences brought by $\Delta\omega_l$ and $\Delta\omega_t$ are analyzed separately. As a result, the magnitude of the calculated rotor flux linkage $\vec{\lambda}^{s\prime}_R$ is smaller than its actual magnitude. Consequently, both the analytical driving torque and the analytical resistant torque are smaller than their corresponding numerical results.

Over the range of $f_s \in [0\text{ Hz}, 400\text{ Hz}]$ and $n_v \in [0\text{ rpm}, 3500\text{ rpm}]$, the standard deviation between the analytical and FEM results is 0.267 which is about 11.8% of the maximum value of FEM T_e. At f_s=0 Hz, if the input frequency is non-zero, the driving torque calculated from the analytical model is negative. However, as n_r is zero, T_e at f_s=0 Hz shall be zero theoretically.

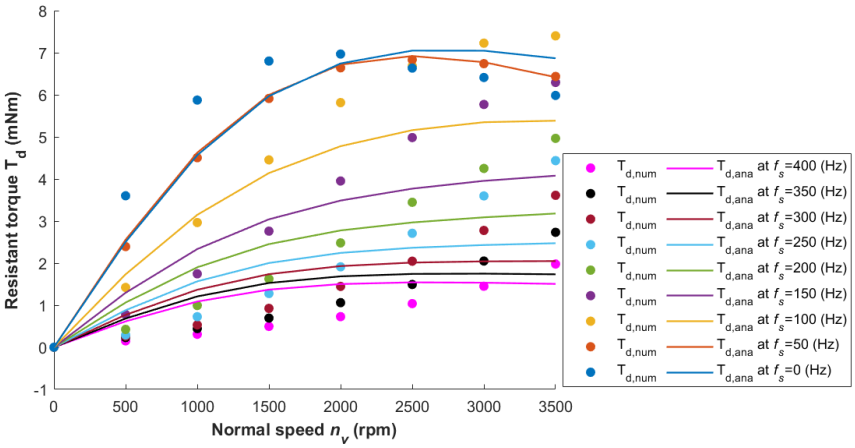

Figure 6.14: Comparison of the analytical and numerical resistant torque T_d generated at different slip frequencies f_s and different normal speeds n_v.

Fig. 6.14 compares the analytical and numerical resistant torque T_e (about the x-axis) generated by AERS at different slip frequencies f_s and different normal speeds n_v. Similar to Fig. 6.13, at a low slip frequency f_s, the analytical torque-speed curve T_d-n_v can match the corresponding numerical results well. When f_s increases, n_v corresponding to the peak of the numerical T_d-n_v curve increases. However, in the analytical T_d-n_v curve, n_v corresponding to the peak torque does not increase as fast as that in the numerical curves. As a result, deviations between the analytical and numerical T_e increase. Reasons for the increasing deviation are the same as those for the deviation presented in

Fig. 6.13. Over the range of $f_s \in [0\ \text{Hz}, 400\ \text{Hz}$ and $n_v \in [0\ \text{rpm}, 3500\ \text{rpm}]$, the standard deviation between the analytical and FEM results is 0.843 which is about 11.4% of the maximum value of FEM T_d.

6.5. SUMMARY

Motion coupling involved in induction-based reaction spheres is investigated. Driving torques and resistant torques influenced by the motion coupling are modeled through a hybrid FEM-analytical approach. The developed torque model is validated through comparisons with corresponding numerical simulations. Deviations between analytically and numerically obtained results for driving and resistant torques are within 13%, if disturbances are not considered. Although the torque model is derived from a basic design, it is generally applicable to induction-based spherical actuators. For validation, the developed torque model is applied to the prototype of an electrodynamic reaction sphere. The standard deviation between torques analytically calculated and those from finite element simulations is within 11.8% of the maximum torque value. Compared to numerical simulations and experiments on a prototype, the proposed analysis method reduces time and cost significantly. Performance analysis for the arbitrary-axis rotation of a newly designed induction-based spherical actuator is greatly facilitated.

7

CONCLUSIONS AND OUTLOOK

7.1. SUMMARY

This dissertation is focused on the development of reaction spheres suitable for the attitude control of small satellites. Compared to conventional reaction wheels, reaction spheres appear superior since a single actuator can provide three-dimensional torques. By replacing a set of reaction wheels with a single reaction sphere, both the volume and power consumption of ADCS can be reduced. Currently, although dozens of designs of reaction spheres have been proposed and some even have been manufactured, their development is still at a low TRL. To help with the design and development of reaction spheres, this dissertation addresses three research questions:

RQ1: How does a reaction sphere work and what restricts performances of existing reaction spheres?

The first research question was addressed in Chapter 2 through a literature review. The driving unit and the bearing, as two essential parts of a reaction sphere, were reviewed in depth. The driving unit of a reaction sphere could be classified into two types: electromagnetic motor-based and piezo/ultrasonic motor-based. Electromagnetic motor-based driving units can be further classified into four categories: PM motor-based, induction motor-based, reluctance motor-based and hysteresis motor-based. The advantages and disadvantages of each type of driving unit are discussed and compared in detail. Concerning the application of reaction spheres to the attitude control of small satellites, these types of driving units are evaluated in Chapter 3. Due to the speed limit of piezo/ultrasonic motors, complicated orientation measurements and coil switching strategies of PM-based spherical motors, the induction motor-based driving unit is selected as the most promising candidate for further study. A wide-ranging review was also conducted for the bearing unit and possible candidates are evaluated. Active magnetic bearings and ball bearings are chosen as the top two most suitable bearings for the selected induction-based driving unit.

RQ2: How to effectively model performances of an induction-based reaction sphere?

RQ2 is answered in Chapter 5 while Chapter 3 and Chapter 4 facilitate the research presented in Chapter 5 and Chapter 6. In Chapter 3, an induction-based reaction sphere

is designed. The rotor is made of a ferromagnetic core and an external copper layer. The rotor is surrounded by three sets of stator windings energized with alternating currents. Both configurations with active magnetic bearings and ball bearings are presented. In the case where active magnetic bearings are employed, the conductive rotor will be attached with PMs. In Chapter 4, electromagnetic fields excited by PMs and energized stator windings are modeled analytically. With the analytically calculated magnetic flux density, electromagnetic torques acting on the rotor can be calculated through the Maxwell stress tensor. When active magnetic bearings are employed, interactions between PMs, the ferromagnetic core and the revolving magnetic field excited by stator windings generate disturbance forces in addition to driving torques. By analyzing possible methods to mitigate the disturbance, the configuration with ball bearing appears easier to control and was adopted for further study. In Chapter 5, the reaction sphere's single-axis rotation performance is analyzed through the equivalent circuit approach. Circuit parameters are obtained from the analytically calculated magnetic flux density distribution within the actuator. Based on this, performance characteristics such as the torque-speed curve and the achievable maximum torque can be calculated within seconds. For validation, the proposed performance analysis method is applied to an experimental case. Mean absolute percentage errors of predicted torque-speed curves are within 23% and are mainly caused by end effects.

RQ3: What is the biggest challenge to control an induction-based reaction sphere?

RQ3 is addressed in Chapter 6. Couplings involved in the induction-based reaction sphere are discussed since they complicate the speed and torque control of the actuator. Among two types of couplings (i.e., electromagnetic coupling and motion coupling), motion coupling is investigated thoroughly. Motion coupling refers to the phenomenon that when the rotor's spin axis deviates from the revolving axis of the magnetic field, a resistant torque will be generated in addition to the driving torque. A hybrid FEM-analytical torque model was developed for the case where only one stator winding set is energized while the rotor performs arbitrary-axis rotations. In the proposed analysis method, the original problem is transferred to the scenario where the rotor is stationary while the AC winding set performs rotations about an arbitrary axis. Based on the study results of single-axis rotations presented in Chapter 5, electromagnetic forces acting on the entire rotor body are assumed acting on magnetic poles whose movement can be formulated in a simple way. The movement of a magnetic pole is decomposed into movements along the longitudinal direction (referred to as $\vec{e}_{l,P}$) and the transverse direction (referred to as $\vec{e}_{t,P}$) of the winding set. The movement along $\vec{e}_{l,P}$ generates a thrust force along $\vec{e}_{l,P}$ whose magnitude is calculated based on the study results of single-axis rotations. Similarly, the movement along $\vec{e}_{t,P}$ generates a thrust force along $\vec{e}_{t,P}$. Calculation of the thrust along $\vec{e}_{t,P}$ is based on a set of FEM simulations where the stator winding set is energized with direct currents and the rotor's spin axis is orthogonal to the winding set's axial direction. In this way, a hybrid FEM-analytical torque model was developed which was validated through comparisons with corresponding numerical simulations of arbitrary-axis rotation. Drivings torques and resistant torques obtained through the developed model deviate from those obtained by numerical simulations by 13% at maximum, if additional disturbances brought by the arbitrary-axis rotation are not considered.

7.2. INNOVATIONS AND CONCLUSIONS

This dissertation focuses on the study of induction-based reaction spheres. The relation between their design parameters and single-axis rotation performances was modeled analytically. A revealing insight into motion coupling involved in arbitrary-axis rotations was offered through a hybrid FEM-analytical analysis approach. Main results and contributions of this dissertation to the scientific body of knowledge are summarized in the following.

A comprehensive review of the driving unit and the bearing unit of a reaction sphere was presented. Through comparisons and discussions, factors restricting the performances of each type of reaction sphere were identified. Concerning the application for attitude control of small satellites, the induction-based reaction sphere is selected as the most promising choice via the analytic hierarchy process (AHP) for its relatively simple manufacture and control.

The magnetic field excited by three-phase stator windings was modeled analytically with the three components of magnetic flux density. Usually, only components along the radial direction and the longitudinal direction of the winding set are modeled and they are sufficient for the calculation of electromagnetic torques. In this dissertation, the magnetic flux density distribution along the transverse direction of the winding set was modeled for the first time. It helps to understand how transverse end effects change the magnetic field distribution. Furthermore, through analytical modeling of fields involved in the designed reaction sphere, disturbance brought by active magnetic bearings to the induction-based driving unit was analyzed. It was found that electromagnetic forces are generated in addition to the driving torque.

Performances of single-axis rotations of an induction-based reaction sphere were analyzed through the equivalent circuit approach. Circuit parameters are determined innovatively through analytically modeled magnetic field distribution. In this way, the torque generation capability of a newly designed actuator can be evaluated before the manufacturing process. Compared to numerical simulations or prototype experiments, the proposed performance analysis method reduces compute time and develop cost greatly. Since equivalent circuit parameters of single-axis rotations are determined through the analytically modeled field distribution, they can be expressed as functions of the design parameters of the actuator. Hence, performances such as the achievable maximum torque during the single-axis rotation can be formulated as functions of design parameters too. In this way, an analytical optimization model of induction-based spherical actuators was developed, concerning their single-axis rotation performances. This model facilitates the design and modification process of an induction-based spherical actuator significantly.

Couplings involved in arbitrary-axis rotations of the induction-based reaction sphere were investigated. Influences brought by each type of coupling, i.e., electromagnetic coupling between windings and motion coupling caused by the changeable spin axis of the rotor, were analyzed. Among the two types of coupling, motion coupling is inevitable and affects the resultant torque greatly. In this dissertation, motion coupling was investigated thoroughly for the first time. A hybrid FEM-analytical model was developed to model the generated driving torque and the additional resistant torque. Both the driving torque and the resistant torque fluctuate. Their mean values and fluctuating

magnitudes are determined by the stator winding's input angular frequency, the rotor's spin speed and the spin axis.

7.3. OUTLOOK

Considering the application for attitude control of small satellites, the induction-based reaction sphere has been selected as the most promising candidate. However, it is a complicated actuator. Making it work as efficiently as conventional induction machines is challenging and requires extensive further research to be conducted.

Firstly, the configuration of stator windings of an induction-based reaction sphere shall be improved. In Fig. 6.11, the three stator winding sets do not overlap with each other. However, since the radius of each stator winding set is much smaller than that of the rotor, the arm length of the generated electromagnetic force is short and results in a limited torque generation capability. Usually, for a maximum arm length, stator windings are placed at the rotor's equator area (see Fig. 6.1). A problem brought by such a configuration is how to assemble three winding sets. If winding sets overlap, the volume taken by windings will expand. To avoid overlapping, linear inductors mentioned in Chapter 1 may be a good choice. If the longitudinal end effect of linear inductors can be modeled with better precision, the manufacturing and assembly of induction-based spherical actuators will be greatly simplified.

Concerning the single-axis rotation of induction-based spherical actuators, the developed performance analysis model allows designers to optimize the achievable maximum torque and its corresponding slip frequency. As per (5.19), copper loss on the rotor of the designed rection sphere can be expressed as the product of the generated torque and the corresponding slip frequency. If the reaction sphere works in the stable operation region, the maximum copper loss on the rotor occurs at the maximum torque point. Since the heat dissipation capability of a reaction sphere is limited during operations in space, thermal analysis is necessary.

Extensive research into transverse end effects is expected. In this dissertation, both the study for single-axis rotation and the study for arbitrary-axis rotation focuses on the case where only one stator winding set is energized and unenergized winding sets are approximated as the top/bottom shells. For single-axis rotations, the existence of top/bottom shells helps to model the field distribution and torque generation. Concerning the basic reaction sphere design, it is found that with exactly the same input parameters, driving torques generated by the numerical model without top/bottom shells are about 60% higher than those generated by the numerical model with shells. This phenomenon happens both in single-axis rotations and arbitrary-axis rotations. However, resistant torques generated by the two models are similar and their difference is about 13%. In practice, induction-based spherical actuators are usually without top/bottom shells. Therefore, investigating how transverse end effects influence single-axis and arbitrary-axis rotations is of vital importance.

In the analytical torque modeling for arbitrary-axis rotations, since movements of magnetic poles are focused instead of changes of the entire magnetic field, the minimum value of the resistant torque generated during rotations is always lower than the corresponding numerical result. Additionally, because slip frequencies along the longitudinal and transverse directions are analyzed separately, insufficient couplings are

included in the torque model. As a result, the magnitude of the calculated rotor flux linkage is smaller than its actual value and this error becomes notable when the normal speed component is high. Therefore, the developed torque model provides acceptable accuracy of mean torques only for cases where the normal speed component is within a low speed range. For the designed reaction sphere, the upper limit of the speed range is usually smaller than the difference between the parallel speed component and the mechanical synchronous speed. And the upper limit of the speed range decreases when the difference between the parallel speed component and the mechanical synchronous speed increases. To correct this defect, an improved model where eddy currents flowing along the longitudinal and transverse directions are more closely coupled shall be developed.

REFERENCES

[1] W. J. Larson and J. R. Wertz, *Space mission analysis and design*, Vol. 1 (Microcosm, Inc., Torrance, CA, 1992).

[2] W. Haeussermann, *The spherical control motor for three axis attitude control of space vehicles*, Tech. Rep. (NASA, 1959).

[3] C. Fan, D. Fan, Y. He, J. Song, N. Zhang, and X. Liu, *Attitude dynamics modeling and analysis of aggregated modular spacecraft with magnetically levitated spherical momentum actuators,* in *2016 35th Chinese Control Conference (CCC)* (IEEE, 2016) pp. 1926–1931.

[4] J. Zhang, L. Yuan, S.-L. Chen, Y. Liang, X. Huang, C. Zhang, and G. Yang, *A survey on design of reaction spheres and associated speed and orientation measurement technologies,* ISA transactions **99**, 417 (2012).

[5] O. Chételat, *Torquer apparatus,* (2012), uS Patent 8,164,294.

[6] L. Rossini, E. Onillon, A. Boletis, S. Mingard, R. Wawrzaszek, J. Serin, and C. Ortega, *Development and closed-loop experimental results of a reaction sphere elegant breadboard,* in *Proc. 16th Eur. Space Mech. Tribol. Symp.* (2015) pp. 1–6.

[7] E. Stagmer, *Reaction sphere for stabilization and control in three axes,* (2016), uS Patent 9,475,592.

[8] C. Fan, D. Fan, Y. He, N. Zhang, X. Liu, and J. Song, *A fast ball momentum module installed attitude control actuator,* (2018), cN105388903B.

[9] A. Yew, M. Colvin, E. Stagmer, and M. Stoddard, *3d motor for multi-axis attitude control on smallsats,* .

[10] L. Zhu, J. Guo, and E. Gill, *Scaling effects in miniaturization of reaction spheres,* in *69th International Astronautical Congress (IAC)* (2018) pp. 1–10.

[11] L. Spitzer Jr, *Space telescopes and components,* Astronomical Journal, **65**, 242 (1960).

[12] J. P. D. Matthew P. Wampler-Doty, *A reaction sphere for high performance attitude control,* in *8th Annual CubeSat Workshop, CalPoly, USA* (CalPoly, 2011).

[13] D.-K. Kim, H. Yoon, W.-Y. Kang, Y.-B. Kim, and H.-T. Choi, *Development of a spherical reaction wheel actuator using electromagnetic induction,* Aerospace Science and Technology **39**, 86 (2014).

[14] Y. Shirasawa and Y. Tsuda, *System performance analysis of three dimensional reaction wheel for the attitude control of microsatellites,* Transactions of the Japan Society for Aeronautical and Space Sciences **7**, Pd_105 (2009).

[15] Z. Huai, M. Zhang, Y. Zhu, A. Chen, K. Yang, C. Hu, J. Hu, L. Xin, and L. Wang, *A novel electrodynamic reaction sphere prototype for spacecraft attitude control,* IEEE Transactions on Industrial Electronics **67**, 3879 (2019).

[16] H. A. Toliyat and G. B. Kliman, *Handbook of electric motors*, Vol. 120 (CRC press, 2018).

[17] L. Zhou, M. I. Nejad, and D. L. Trumper, *One-axis hysteresis motor driven magnetically suspended reaction sphere,* Mechatronics **42**, 69 (2017).

[18] V. Bakanauskas, R. Bansevičius, D. Bručas, and A. Domeika, *Development of a novel device for attitude control over small satellites,* in *Solid State Phenomena*, Vol. 220 (Trans Tech Publ, 2015) pp. 561–564.

[19] R. Takehana, H. Paku, and K. Uchiyama, *Attitude control of satellite with a spherical rotor using two-degree-of-freedom controller,* in *2016 7th International Conference on Mechanical and Aerospace Engineering (ICMAE)* (IEEE, 2016) pp. 352–357.

[20] B. Dehez, V. Froidmont, D. Grenier, and B. Raucent, *Design, modeling and first experimentation of a two-degree-of-freedom spherical actuator,* Robotics and Computer-Integrated Manufacturing **21**, 197 (2005).

[21] S. Čorović, M. Vidrih, and D. Miljavec, *Three-dimensional finite element modeling and analysis of spherical induction motor,* in *2016 17th International Conference on Mechatronics-Mechatronika (ME)* (IEEE, 2016) pp. 1–4.

[22] B. Dehez, G. Galary, D. Grenier, and B. Raucent, *Development of a spherical induction motor with two degrees of freedom,* IEEE Transactions on Magnetics **42**, 2077 (2006).

[23] K. Davey, G. Vachtsevanos, and R. Powers, *The analysis of fields and torques in spherical induction motors,* IEEE Transactions on Magnetics **23**, 273 (1987).

[24] J. F. P. Fernandes, V. M. Machado, and P. J. C. Branco, *Magnetic field analysis in shell-like spherical induction machines with zenithal traveling waves,* IEEE Transactions on Energy Conversion **32**, 1081 (2017).

[25] F. Wani, *Three dimensional Finite Element Modeling of a Brushless Doubly-fed Induction Machine*, Master's thesis, TU Delft (2016).

[26] L. Yan, Z. Duan, Q. Zhang, H. Qiao, and C. Gerada, *Development and structure of multi-dof spherical induction motor,* in *2018 13th IEEE Conference on Industrial Electronics and Applications (ICIEA)* (IEEE, 2018) pp. 2831–2835.

[27] J. Han, *Coupling Characteristic and Control System of 2-DOF Direct Drive Induction Motor*, Master's thesis, Henan Polytechnic University (2016).

[28] J. Si, L. Xie, X. Xu, Y. Zhu, and W. Cao, *Static coupling effect of a two-degree-of-freedom direct drive induction motor,* IET Electric Power Applications **11**, 532 (2017).

[29] J. Si, L. Ai, H. Feng, Y. Zhu, and Y. Hu, *Analysis on coupling effect of 2-dof direct drive induction motor based on 3-d model,* in *2014 17th International Conference on Electrical Machines and Systems (ICEMS)* (IEEE, 2014) pp. 1157–1163.

[30] M. Kumagai and R. L. Hollis, *Development and control of a three dof spherical induction motor,* in *Robotics and Automation (ICRA), 2013 IEEE International Conference on* (IEEE, 2013) pp. 1528–1533.

[31] A. Bhatia, M. Kumagai, and R. Hollis, *Six-stator spherical induction motor for balancing mobile robots,* in *2015 IEEE International Conference on Robotics and Automation (ICRA)* (IEEE, 2015) pp. 226–231.

[32] J. Si, L. Xie, J. Han, H. Feng, W. Cao, and Y. Hu, *Mathematical model of two-degree-of-freedom direct drive induction motor considering coupling effect,* Journal of Electrical Engineering and Technology **12**, 1227 (2017).

[33] T. L. Saaty, *How to make a decision: the analytic hierarchy process,* European journal of operational research **48**, 9 (1990).

[34] L. Zhu, J. Guo, and E. Gill, *Review of reaction spheres for spacecraft attitude control,* Progress in Aerospace Sciences **91**, 67 (2017).

[35] L. Yan, I.-M. Chen, G. Yang, and K.-M. Lee, *Analytical and experimental investigation on the magnetic field and torque of a permanent magnet spherical actuator,* IEEE/ASME Transactions on Mechatronics **11**, 409 (2006).

[36] K. Bai, J. Ji, K.-M. Lee, and S. Zhang, *A two-mode six-dof motion system based on a ball-joint-like spherical motor for haptic applications,* Computers & Mathematics with Applications **64**, 978 (2012).

[37] H. Li, C. Xia, P. Song, and T. Shi, *Magnetic field analysis of a halbach array pm spherical motor,* in *IEEE International Conference on Automation and Logistics, Jinan, China* (IEEE, 2007) pp. 2019–2023.

[38] C. Xia, H. Li, and T. Shi, *3-d magnetic field and torque analysis of a novel halbach array permanent-magnet spherical motor,* IEEE Transactions on Magnetics **44**, 2016 (2008).

[39] C. Xia, J. Xin, H. Li, and T. Shi, *Design and analysis of a variable arc permanent magnet array for spherical motor,* IEEE Transactions on Magnetics **49**, 1470 (2013).

[40] T. Yano, Y. Kubota, T. Shikayama, and T. Suzuki, *Basic characteristics of a multi-pole spherical synchronous motor,* in *International Symposium on Micro-NanoMechatronics and Human Science, Nagoya, Japan* (IEEE, 2007) pp. 383–388.

[41] K. Kahlen and R. De Doncker, *Current regulators for multi-phase permanent magnet spherical machines,* in *IEEE Industry Applications Conference: 35th IAS Annual Meeting and World Conference on Industrial Applications of Electrical Energy, Roma, Italy*, Vol. 3 (IEEE, 2000) pp. 2011–2016.

[42] E. Onillon, O. Chételat, L. Rossini, L. Lisowski, S. Droz, and J. Moerschell, *Reaction sphere for attitude control,* in *13th European Space Mechanisms and Tribology Symposium, Vienna, Austria* (ESA, 2009).

[43] L. Rossini, O. Chételat, E. Onillon, and Y. Perriard, *An open-loop control strategy of a reaction sphere for satellite attitude control,* in *International Conference on Electrical Machines and Systems (ICEM), Beijing, China* (IEEE, 2011) pp. 1–4.

[44] L. Rossini, S. Mingard, A. Boletis, E. Forzani, E. Onillon, and Y. Perriard, *Rotor design optimization for a reaction sphere actuator,* IEEE Transactions on Industry Applications **50**, 1706 (2014).

[45] L. Rossini, E. Onillon, O. Chételat, and Y. Perriard, *Closed-loop magnetic bearing and angular velocity control of a reaction sphere actuator,* Mechatronics **30**, 214 (2015).

[46] T. Yano, *Basic characteristics of a hexahedron-octahedron based spherical stepping motor,* in *International Symposium on Power Electronics, Electrical Drives, Automation and Motion (SPEEDAM), Pisa, Italy* (IEEE, 2010) pp. 1748–1753.

[47] E. Stagmer, *Reaction sphere for stabilization and control in three axes,* (2014), uS Patent App. 14/170,104.

[48] S. Ikeshita, A. Gofuku, T. Kamegawa, and T. Nagai, *Development of a spherical motor driven by electro-magnets,* Journal of mechanical science and technology **24**, 43 (2010).

[49] G. S. Chirikjian and D. Stein, *Kinematic design and commutation of a spherical stepper motor,* IEEE/ASME transactions on mechatronics **4**, 342 (1999).

[50] Q. Wang, Z. Li, Y. Ni, and W. Jiang, *Magnetic field computation of a pm spherical stepper motor using integral equation method,* IEEE transactions on magnetics **42**, 731 (2006).

[51] Z. Li, *Intelligent control for permanent magnet spherical stepper motor,* in *IEEE International Conference on Automation and Logistics, Qingdao, China* (IEEE, 2008) pp. 1807–1812.

[52] M. K. Rashid and Z. A. Khalil, *Configuration design and intelligent stepping of a spherical motor in robotic joint,* Journal of Intelligent and Robotic Systems **40**, 165 (2004).

[53] Z. Li, *Robust control of pm spherical stepper motor based on neural networks,* IEEE Transactions on Industrial Electronics **56**, 2945 (2009).

[54] K.-M. Lee, J. Pei, and R. Roth, *Kinematic analysis of a three-degrees-of-freedom spherical wrist actuator,* Mechatronics **4**, 581 (1994).

[55] R. D. Ormsby, *A free reaction sphere satellite attitude control system,* in *IAS National Specialists Meeting on Guidance of Aerospace Vehicles, Boston, Mass* (1960) pp. 53–55.

[56] R. D. Ormsby, *Capabilities and limitations of reaction spheres for attitude control,* ARS Journal **31**, 808 (1961).

[57] F. Williams, E. Laithwaite, and J. Eastham, *Development and design of spherical induction motors,* Proceedings of the IEE-Part A: Power Engineering **106**, 471 (1959).

[58] Y. Shirasawa and Y. Tsuda, *Experimental study and analysis on three dimensional reaction wheel for microsatellites,* in *18th AAS/AIAA Space Flight Mechanics Meeting, Galveston, Texas*, Vol. 130 (AIAA, 2008) pp. 507–17.

[59] A. Iwakura, S. Tsuda, and Y. Tsuda, *Investigation of 3 dimensional reaction wheel,* in *57th International Astronautical Congress (IAC), Valencia, Spain* (2006).

[60] A. IWAKURA, S.-i. TSUDA, and Y. TSUDA, *Feasibility study on three dimensional reaction wheel,* Proceedings of the School of Engineering of Tokai University **33**, 51 (2008).

[61] G. Park, H. Yoon, D.-k. Kim, K.-L. Yong, and S. E. Petrov, *Feasibility study & system conceptual design for the spherical actuator,* in *11th International Conference on Control, Automation and Systems (ICCAS), Gyeonggi-do, South Korea* (IEEE, 2011) pp. 1875–1879.

[62] J. Doty, *Reaction sphere for spacecraft attitude control,* (2010), wO Patent App. PCT/US2010/029,283.

[63] T. Finken, M. Felden, and K. Hameyer, *Comparison and design of different electrical machine types regarding their applicability in hybrid electrical vehicles,* in *18th International Conference on Electrical Machines (ICEM), Vilamoura, Portugal* (IEEE, 2008) pp. 1–5.

[64] G. Kamiński and A. Smak, *Modern constructions of motors with spherical rotors,* Archives of Electrical Engineering **50**, 215 (2001).

[65] C. Wildmann, T. Nussbaumer, and J. Kolar, *10 mrpm spinning ball motor: Preparing the next generation of ultra-high speed drive systems,* in *International Power Electronics Conference (IPEC), Sapporo, Japan* (IEEE, 2010) pp. 278–283.

[66] C. Wildmann, T. Nussbaumer, and J. Kolar, *Design considerations for the drive system of an ultra-high speed spinning ball motor,* in *International Symposium on Power Electronics, Electrical Drives, Automation and Motion (SPEEDAM), Pisa, Italy* (IEEE, 2010) pp. 1478–1483.

[67] P. Vijayraghavan and R. Krishnan, *Noise in electric machines: A review,* in *Industry Applications Conference, 1998. Thirty-Third IAS Annual Meeting. The 1998 IEEE*, Vol. 1 (IEEE, 1998) pp. 251–258.

[68] L. Zhou, *Magnetically suspended reaction sphere with one-axis hysteresis drive,* (2014).

[69] H. A. Toliyat and G. B. Kliman, *Handbook of electric motors*, Vol. 120 (CRC press, 2004).

[70] L. Zeng, J. Wang, and D. Zhang, *Mechanism of magnetic force and electromagnetic torque for spherical reluctance motor with magnetic levitation,* Zhongguo Jixie Gongcheng(China Mechanical Engineering) **22**, 208 (2011).

[71] J. Liu, *Structural design and three-dimensional magnetic field analysis of magnetic levitation switched reluctance spherical motor*, Master's thesis, Yangzhou University (2011).

[72] L. Zeng, Z. Zhu, J. Sun, Z. Fan, and L. Zhang, *Study on mathematical modeling and experiment of inductive magnetic-gas mixed suspension spherical joint,* in *Proceedings of the 5th IIAE International Conference on Intelligent Systems and Image* (2011).

[73] K.-M. Lee, R. B. Roth, and Z. Zhou, *Dynamic modeling and control of a ball-joint-like variable-reluctance spherical motor,* Journal of dynamic systems, measurement, and control **118**, 29 (1996).

[74] Z. Zhou and K.-M. Lee, *Real-time motion control of a multi-degree-of-freedom variable reluctance spherical motor,* in *IEEE International Conference on Robotics and Automation, Minneapolis, Minnesota*, Vol. 3 (IEEE, 1996) pp. 2859–2864.

[75] K.-M. Lee, R. A. Sosseh, and Z. Wei, *Effects of the torque model on the control of a vr spherical motor,* Control engineering practice **12**, 1437 (2004).

[76] K.-M. Lee, G. Vachtsevanos, and C. Kwan, *Development of a spherical stepper wrist motor,* Journal of Intelligent and Robotic Systems **1**, 225 (1988).

[77] K.-M. Lee and C.-K. Kwan, *Design concept development of a spherical stepper for robotic applications,* IEEE Transactions on Robotics and Automation **7**, 175 (1991).

[78] K. Spanner and B. Koc, *Piezoelectric motors, an overview,* in *Actuators*, Vol. 5 (Multidisciplinary Digital Publishing Institute, 2016) p. 6.

[79] A. Shafik and R. B. Mrad, *Piezoelectric motor technology: a review,* in *Nanopositioning Technologies* (Springer, 2016) pp. 33–59.

[80] H. Paku and K. Uchiyama, *Satellite attitude control system using a spherical reaction wheel,* Applied Mechanics and Materials **798**, 256 (2015).

[81] H. Paku, R. Takehana, and K. Uchiyama, *spherical reaction wheel system for satellite attitude control,* in *54th AIAA Aerospace Sciences Meeting, San Diego, USA* (AIAA, 2016) p. 0693.

[82] Y. Ting, Y.-R. Tsai, B.-K. Hou, S.-C. Lin, and C.-C. Lu, *Stator design of a new type of spherical piezoelectric motor,* IEEE transactions on ultrasonics, ferroelectrics, and frequency control **57** (2010).

[83] R. Bansevicius and V. Kargaudas, *Attitude control of micro-and nanosatellites using multi-degree-of-freedom piezoelectric actuators,* in *Vibration Problems ICOVP* (Springer, 2011) pp. 379–384.

[84] K. Takemura, N. Kojima, and T. Maeno, *Development of a bar-shaped ultrasonic motor for multi-degrees of freedom motion,* in *4th International Conference on Motion and Vibration Control, ETH Zurich, Switzerland*, Vol. 1 (1998) pp. 195–200.

[85] C. Zhao, *Ultrasonic motors: technologies and applications* (Springer Science & Business Media, 2011).

[86] S. Zhao, *Investigation of non-contact bearing systems based on ultrasonic levitation*, Ph.D. thesis, Paderborn University (2010).

[87] C. Chen, J. Wang, B. Jia, and F. Li, *Design of a noncontact spherical bearing based on near-field acoustic levitation,* Journal of Intelligent Material Systems and Structures **25**, 755 (2014).

[88] C. Galassi, M. Dinescu, K. Uchino, and M. Sayer, *Piezoelectric materials: advances in science, technology and applications*, Vol. 76 (Springer Science & Business Media, 2012).

[89] H. Schröpl, *Attitude stabilization of satellites by means of the free reaction sphere*, Tech. Rep. (NASA, 1965).

[90] S. Earnshaw, *On the nature of the molecular forces which regulate the constitution of the luminiferous ether,* Transactions of the Cambridge Philosophical Society **7**, 97 (1842).

[91] M. BERRY, *The levitron: an adiabatic trap for spins,* in *Proceedings: Royal Society. Mathematical and physical sciences, UK*, Vol. 452 (Royal Society of London, 1996) pp. 1207–1220.

[92] R. Jansen and E. DiRusso, *Passive magnetic bearing with ferrofluid stabilization*, Tech. Rep. (NASA, 1996).

[93] H. Bleuler, M. Cole, P. Keogh, R. Larsonneur, E. Maslen, Y. Okada, G. Schweitzer, A. Traxler, G. Schweitzer, E. H. Maslen, *et al.*, *Magnetic bearings: theory, design, and application to rotating machinery* (Springer Science & Business Media, 2009).

[94] Y. Su, Z. Xiao, Z. Ye, and K. Takahata, *Micromachined graphite rotor based on diamagnetic levitation,* IEEE Electron Device Letters **36**, 393 (2015).

[95] K. Liu, W. Zhang, W. Liu, W. Chen, K. Li, F. Cui, and S. Li, *An innovative micro-diamagnetic levitation system with coils applied in micro-gyroscope,* Microsystem technologies **16**, 431 (2010).

[96] A. Judge, *Air gap elimination in permanent magnet machines*, Ph.D. thesis, Worcester Polytechnic Institute (2011).

[97] D. Spalek and K. Waleczek, *Spherical induction motor with ferrofluids in gap,* in *International Conference on Electrical Machines (ICEMS), Cracow, Poland* (IEEE, 2004).

[98] A. Nethe, T. Scholz, H.-D. Stahlmann, and M. Filtz, *Ferrofluids in electric motors-a numerical process model,* IEEE transactions on magnetics **38**, 1177 (2002).

[99] S. Van Veen, *Planar ferrofluid bearings for precision stages*, Ph.D. thesis, Delft University of Technology (2013).

[100] A. Chen, M. Zhang, Y. Zhu, Z. Huai, K. Yang, C. Hu, and J. Hu, *Force and torque model utilising transfer-matrix theory for a novel electrodynamic suspension reaction sphere,* IET Electric Power Applications **12**, 63 (2017).

[101] J. L. Nikolajsen, *Experimental investigation of an eddy-current bearing,* in *Magnetic Bearings* (Springer, 1989) pp. 111–118.

[102] J. Detoni, *Progress on electrodynamic passive magnetic bearings for rotor levitation,* Proceedings of the Institution of Mechanical Engineers, Part C: Journal of Mechanical Engineering Science **228**, 1829 (2014).

[103] L. Ting and J. Tichy, *Stiffness and damping of an eddy current magnetic bearing,* Journal of tribology **114**, 600 (1992).

[104] E. Cocci, *Optimal control of reaction wheels disturbance transients,* (2016).

[105] J. Seddon, *3Dwheel: attitude control of small satellites using magnetically levitated momentum wheels*, Ph.D. thesis, University of Surrey (2011).

[106] Y. J. Li Lijun, Fan Yahong, *Application of magnetically suspended gimbaling flywheel in satellite attitude maneuver,* Chinese Journal of Mechanical Engineering **51**, 206 (2015).

[107] A. Borisavljevic, *Limits, modeling and design of high-speed permanent magnet machines*, Ph.D. thesis, TU Delft, Delft University of Technology (2011).

[108] M. Scharfe, K. Meinzer, and R. Zimmermann, *Development of a magnetic-bearing momentum wheel for the amsat phase 3-d small satellite,* in *International Symposium on Small Satellites, Annecy, France* (ESA, 1996).

[109] L. Burgmeier and M. Poursaba, *Ceramic hybrid bearings in air-cycle machines,* Journal of Engineering for Gas Turbines and Power **118**, 184 (1996).

[110] L. Yan, I.-M. Chen, C. K. Lim, G. Yang, W. Lin, and K.-M. Lee, *Design and analysis of a permanent magnet spherical actuator,* IEEE/ASME Transactions on mechatronics **13**, 239 (2008).

[111] W. H. Isely, *Magnetically supported and torqued momentum reaction sphere,* (1986), uS Patent 4,611,863.

[112] B. Bellakhdhar, A. Dogui, and J. Ligier, *Main bearing stiffness investigation,* International Journal of Mechanical and Materials Engineering **2**, 8 (2011).

[113] K. Kahlen, I. Voss, C. Priebe, and R. W. De Doncker, *Torque control of a spherical machine with variable pole pitch,* IEEE Transactions on power electronics **19**, 1628 (2004).

[114] S. J. Woo, *Contact-free handling using actively controlled electrostatic levitating fields*, Ph.D. thesis, TU Delft, Delft University of Technology (2012).

[115] L. Epstein, *Electrostatic suspension,* American Journal of Physics **33**, 406 (1965).

[116] J.-U. Jeon, J. Jin, and T. Higuchi, *Electrostatic suspension of 8-inch silicon wafer,* in *Annual Meeting of The Institute of Electrostatics Japan, Japan*, Vol. 21 (1997) pp. 62–68.

[117] T. Shigeki, S. Shigeru, Z. Guoqiang, M. Yasutaro, and N. Kazuto, *Multi degree of freedom spherical ultrasonic motor,* in *20th International Conference on Industrial Electronics, Control, and Instrumentation, Bologna, Italy*, Vol. 2 (IEEE, 1994) pp. 900–905.

[118] J. Wang, K. Mitchell, G. W. Jewell, and D. Howe, *Multi-degree-of-freedom spherical permanent magnet motors,* in *IEEE International Conference on Robotics and Automation (ICRA), Seoul, Korea*, Vol. 2 (IEEE, 2001) pp. 1798–1805.

[119] W. Wang, J. Wang, G. Jewell, and D. Howe, *Design and control of a novel spherical permanent magnet actuator with three degrees of freedom,* IEEE/ASME transactions on mechatronics **8**, 457 (2003).

[120] K.-M. Lee, H. Son, J. Joni, *et al.*, *Concept development and design of a spherical wheel motor (swm),* in *IEEE International Conference on Robotics and Automation, Barcelona, Spain*, Vol. 4 (IEEE; 1999, 2005) p. 3652.

[121] L. Zhang, W. Chen, J. Liu, and X. Wu, *Analysis and decoupling control of a permanent magnet spherical actuator,* Review of Scientific Instruments **84**, 125001 (2013).

[122] C.-H. Cho, D.-w. Kang, S.-Y. Kim, S.-H. Won, and J. Lee, *Using mathematical method of torque simulation for reducing calculation time of permanent magnet spherical wheel motor,* in *18th International Conference on Electrical Machines, Vilamoura, Portugal* (IEEE, 2008) pp. 3112–3115.

[123] A. Muszynska, *Whirl and whip—rotor/bearing stability problems,* Journal of Sound and vibration **110**, 443 (1986).

[124] G. Belforte, F. Colombo, T. Raparelli, A. Trivella, and V. Viktorov, *High speed rotors on gas bearings: design and experimental characterization, Tribology in Engineering,* , 81 (2013).

[125] P. Goenka and J. Booker, *Spherical bearings: static and dynamic analysis via the finite element method,* Journal of Lubrication Technology **102**, 308 (1980).

[126] L. Mattei, F. Di Puccio, B. Piccigallo, and E. Ciulli, *Lubrication and wear modelling of artificial hip joints: A review,* Tribology International **44**, 532 (2011).

[127] Y. Ji and C.-s. Zhao, *A new type non-contact ultrasonic motor with higher revolution speed,* Piezoelectrics & Acoustooptics **28**, 527 (2006).

[128] R. L. Hollis Jr and M. Kumagai, *Spherical induction motor,* (2014), uS Patent App. 14/177,450.

[129] G. Galary, B. Dehez, and D. Grenier, *Finite element modeling of a two-degree of freedom spherical actuator,* COMPEL: Int J for Computation and Maths. in Electrical and Electronic Eng. **25**, 399 (2006).

[130] C. Stelter, B. Biering, and B. Heym, *Bus design of the microsatellite bird for infrared earth observation,* in *Proceedings of the 11th AIAA/USU Conference on Small Satellites* (1997).

[131] S. Hulst, *The Basics of Motor Selection*, Tech. Rep. (Groschopp, Sioux Center, IA USA, 2013).

[132] X. Xie, *Comparison of bearings: For the bearing choosing of high-speed spindle design,* University of Utah (2003).

[133] J. Powell, *the Design of Aerostatic Bearings* (The machinery Publishing Co.,LTD., 1970).

[134] W. Wu, J. Hong, Y. Li, and X. Li, *Investigation of non-uniform preload effect on stiffness behavior of angular contact ball bearings,* Advances in Mechanical Engineering **9**, 1687814017694118 (2017).

[135] L. Rossini, *Electromagnetic modeling and control aspects of a reaction sphere for satellite attitude control*, Ph.D. thesis, EPFL (2014).

[136] T. A. Lembke, *Design and analysis of a novel low loss homopolar electrodynamic bearing*, Ph.D. thesis, KTH (2005).

[137] A. Filatov, P. McMullen, K. Davey, and R. Thompson, *Flywheel energy storage system with homopolar electrodynamic magnetic bearing,* CEM Publications (2006).

[138] J. Van Verdeghem, V. Kluyskens, and B. Dehez, *Stability and performance analysis of electrodynamic thrust bearings,* in *Actuators*, Vol. 8 (Multidisciplinary Digital Publishing Institute, 2019) p. 11.

[139] H. Takebayashi, *Bearings for extreme special environment (4)- application of ceramic bearings-,* Koyo Engineering Journal , 56 (2002).

[140] H.-I. Lee and M. D. Noh, *Optimal design of toroidally-wound brushless dc machines,* in *Industrial Technology, 2009. ICIT 2009. IEEE International Conference on* (IEEE, 2009) pp. 1–5.

[141] H.-I. Lee, S.-y. Yoo, and M. D. Noh, *Toroidally-wound self-bearing bldc motor with lorentz force,* IEEE Transactions on Magnetics **46**, 2148 (2010).

[142] L. Zhu, J. Guo, and E. Gill, *Analytical field and torque analysis of a reaction sphere,* IEEE Transactions on Magnetics **54**, 1 (2018).

[143] A. Schwab, *Field Theory Concepts: Electromagnetic Fields. Maxwell's Equations grad, curl, div. etc. Finite-Element Method. Finite-Difference Method. Charge Simulation Method. Monte Carlo Method* (Springer Science & Business Media, 2012).

[144] M. Curti, J. J. Paulides, and E. A. Lomonova, *An overview of analytical methods for magnetic field computation,* in *Ecological Vehicles and Renewable Energies (EVER), 2015 Tenth International Conference on* (IEEE, 2015) pp. 1–7.

[145] K.-M. Lee, H. Son, and K. Bai, *Image method with distributed multipole models for analyzing permanent-magnet-based electromagnetic actuators,* in *ASME 2008 Dynamic Systems and Control Conference* (American Society of Mechanical Engineers, 2008) pp. 1083–1089.

[146] L. Yan, D. Liu, Z. Jiao, C.-Y. Chen, and I.-M. Chen, *Magnetic field modeling based on geometrical equivalence principle for spherical actuator with cylindrical shaped magnet poles,* Aerospace Science and Technology **49**, 17 (2016).

[147] W. Xiuhe *et al.*, *Permanent magnet Machines* (Beijing: China Power Press, 2007).

[148] Z. Zhu, D. Howe, and C. Chan, *Improved analytical model for predicting the magnetic field distribution in brushless permanent-magnet machines,* IEEE Transactions on Magnetics **38**, 229 (2002).

[149] D. Lide, *Magnetic susceptibility of the elements and inorganic compounds,* Handbook of Chemistry and Physics , 130 (2000).

[150] A. Candeo, *Induction hardening of components for the aerospace industry,* (2012).

[151] J. D. Jackson, *Classical electrodynamics* (John Wiley & Sons, 2007).

[152] G. Arfken and H. Weber, *Mathematical Methods For Physicists* (Elsevier Science, 2005).

[153] L. Yan, I. Chen, C. Lim, G. Yang, and K. Lee, *Design, Modeling and Experiments of 3-DOF Electromagnetic Spherical Actuators* (Springer Netherlands, 2011).

[154] W. Smythe, *Static and dynamic electricity* (New York, NY (USA); Hemisphere Publishing, 1988).

[155] G. Mrozynski and E. Baum, *Analytical determination of eddy currents in a hollow sphere excited by an arbitrary dipole,* IEEE transactions on magnetics **34**, 3822 (1998).

[156] M. Strumik, R. Wawrzaszek, M. Banaszkiewicz, K. Seweryn, M. Sidz, E. Onillon, and L. Rossini, *Analytical model of eddy currents in a reaction sphere actuator,* IEEE Transactions on Magnetics **50**, 1 (2014).

[157] D. Spałek, *Spherical induction motor with anisotropic rotor–analytical solutions for electromagnetic field distribution, electromagnetic torques and power losses,* Int. Compumag Society. Testing Electromagnetic Analysis Methods (TEAM) **34** (2007).

[158] A. Chiba, T. Fukao, O. Ichikawa, M. Oshima, M. Takemoto, and D. G. Dorrell, *Magnetic bearings and bearingless drives* (Elsevier, 2005).

[159] L. Zhu, J. Guo, and E. Gill, *Performance analysis of induction-based reaction spheres,* IEEE Transactions on Industrial Electronics **67**, 7746 (2019).

[160] J. F. P. Fernandes and P. J. C. Branco, *The shell-like spherical induction motor for low-speed traction: electromagnetic design, analysis, and experimental tests,* IEEE Transactions on Industrial Electronics **63**, 4325 (2016).

[161] M. Cheng, P. Han, G. Buja, and M. G. Jovanovic, *Emerging multiport electrical machines and systems: Past developments, current challenges, and future prospects,* IEEE Transactions on Industrial Electronics **65**, 5422 (2018).

[162] J. Zhang, L.-M. Yuan, S.-L. Chen, C. Zhang, C.-y. Chen, and J. Zhou, *Design and optimization aspects of a novel reaction sphere actuator,* in *Recent Advances in Intelligent Manufacturing* (2018) pp. 84–93.

[163] W. Frei, *How much memory is needed to solve large comsol models?* .

[164] P. C. Sen, *Principles of electric machines and power electronics*, 3rd ed. (John Wiley & Sons, New Jersey, 2007).

[165] A. E. Fitzgerald, C. Kingsley, S. D. Umans, and B. James, *Electric machinery*, 6th ed., Vol. 5 (McGraw-Hill, New York, 2003).

[166] M. Hoeijmakers, *Modelling of AC Machines ET 4121* (TU Delft, Delft, 2004).

[167] I. Boldea and S. A. Nasar, *The induction machine handbook*, 1st ed. (CRC press, Boca Raton, Florida, 2002).

[168] S.-J. Lee, J.-M. Kim, D.-K. An, and J.-P. Hong, *Equivalent circuit considering the harmonics of core loss in the squirrel-cage induction motor for electrical power steering application,* IEEE Transactions on Magnetics **50**, 1 (2014).

[169] X. Liang and Y. Luy, *Harmonic analysis for induction motors,* in *Electrical and Computer Engineering, 2006. CCECE'06. Canadian Conference on* (2006) pp. 172–177.

[170] C. Grantham and D. J. McKinnon, *Rapid parameter determination for induction motor analysis and control,* IEEE Transactions on Industry Applications **39**, 1014 (2003).

[171] T. A. Lipo, *Introduction to AC machine design*, 1st ed., Vol. 63 (John Wiley & Sons, New Jersey, 2017).

[172] *Copper data sheet cu-dhp,* .

[173] W. Xu, J. G. Zhu, Y. Zhang, Y. Li, Y. Wang, and Y. Guo, *An improved equivalent circuit model of a single-sided linear induction motor,* IEEE Transactions on Vehicular Technology **59**, 2277 (2010).

[174] P. Wang, J. Si, L. Xie, Y. Hu, and W. Hua, *Analysis of magnetic-coupling effect on the performances of 2dof direct-drive induction motors,* IET Electric Power Applications **12**, 946 (2018).

[175] L. Xie, J. Si, Y. Hu, H. Feng, and K. Ni, *Characteristics analysis of the motions of the two-degree-of-freedom direct drive induction motor,* IEEE Transactions on Industrial Electronics **67**, 931 (2019).

[176] A. Hughes and B. Drury, *Electric motors and drives: fundamentals, types and applications* (Newnes, 2013).

ACKNOWLEDGEMENTS

Studying in the Space System Engineering group at TU Delft is an important period in my career and in my life. I owe my gratitude to so many people.

First of all, I would like to express my deepest appreciation to my promotors Prof. dr. Eberhard Gill and Dr. Jian Guo. Thank you for providing this opportunity to me to study in this wonderful group. I am so grateful for your support and guidance through these years. Thank you for the discussions and helpful feedback. Thank you for showing me the right direction every time when I was completely lost in the confusion about research. In the past years, I have learned a lot from the way you do research. This invaluable experience will influence me for the rest of my life.

Secondly, I gratefully acknowledge China Scholarship Council for providing the financial support.

Next, I want to thank my husband Zewei for being with me and backing me up all the time. I also want to thank my parents Zhenling Zhu, Juping Li, and my sister Linjie Zhu. Thank you for your unconditional support. My dearest Guan, thank you. Although your birth makes my Ph.D. study more challenging, you bring so much happiness to my life. I love you all my life.

I really appreciate the help from my friends and my Ph.D. colleagues. Thank you, Dadui, Marsil and Johan. I really miss those interesting discussions in the office. Thank you Samiksha, for sharing so much with me and encouraging me so much. Thank you, Minghe, Zixuan, Mao, Yuxin, Fiona, Dennis, Victor, Mario, Prem, Stefano, Lorenzo, Salvatore, and Aldofo for your help. Ruipeng, Pengyu, Erdem, and Stefano, thank you all and wish you good luck with your Ph.D.

I would also like to thank all the staff members at the SSE group, in particular, Debby, Marielle, Vidhya, Barry, Robert, Sevket, Kevin, Stefano, and Sunghoon. I love the friendly atmosphere in the amazing and international group.

At last, thank you, everyone!

A

INVOLVED FUNCTIONS

Functions involved in Chapter 5 are defined:

$$Q_n^1(\theta) = \sqrt{\frac{2n+1}{4\pi}\frac{(n-1)!}{(n+1)!}} P_n^1(\cos\theta) \tag{A.1}$$

note: $P_n^1(\cos\theta)$ is associated Legendre polynomial.

$$\begin{aligned} H_n = n(1+n)(1-s_2^{1+2n})\cdot\big[&\mu_r\left(k_n(as_2R_s)X_n(as_1R_s) + i_n(as_2R_s)Y_n(as_1R_s)\right) \\ &+(1+n)\left(i_n(as_2R_s)k_n(as_1R_s) - i_n(as_1R_s)k_n(as_2R_s)\right)\big] \\ +(1+n+ns_2^{1+2n})\cdot\big[&\mu_r\left(X_n(as_2R_s)Y_n(as_1R_s) - X_n(as_1R_s)Y_n(as_2R_s)\right) \\ &+(1+n)\left(k_n(as_1R_s)X_n(as_2R_s) + i_n(as_1R_s)Y_n(as_2R_s)\right)\big] \end{aligned} \tag{A.2}$$

$$\zeta_n = \frac{(1+2n)s_2^n R_s N_n\left[(1+n)k_n(as_1R_s) + \mu_r Y_n(as_1R_s)\right]}{H_n} \tag{A.3}$$

$$\nu_n = \frac{(1+2n)s_2^n R_s N_n\left[-(1+n)i_n(as_1R_s) + \mu_r X_n(as_1R_s)\right]}{H_n} \tag{A.4}$$

$$N_n = M_n J_s / j \tag{A.5}$$

$$M_n = \int_{\psi}^{\pi-\psi} \frac{\mu_0}{2}\sqrt{\frac{(2n+1)\pi}{n(n+1)}} P_n^1(\cos\theta)\sin\theta\,\mathrm{d}\theta \tag{A.6}$$

$$G_{b,n}(s_1) = \frac{n(2n+1)\mu_r s_1^{n+1} M_n \int_{\theta_b}^{\pi-\theta_b} Q_n^1(\theta)\sin\theta\,\mathrm{d}\theta}{1+n+\mu_r n-(\mu_r-1)ns_1^{1+2n}} \tag{A.7}$$

$$G_{r,n}(s_1,s_2) = \frac{\left[(\mu_r-1)(1+n)s_1^{1+2n} + (1+n+\mu_r n)s_2^{1+2n}\right]}{1+n+\mu_r n-(\mu_r-1)ns_1^{1+2n}} \cdot ns_2^{-n} M_n \int_{\theta_r}^{\pi-\theta_r} Q_n^1(\theta)\sin\theta\,\mathrm{d}\theta \tag{A.8}$$

A

$$F_{b,n}(s_1,s_2) = n(n+1)(1+2n)s_1 s_2^n M_n \cos(\phi_{b,n}-\phi_{b,1})\cdot|U_{b,n}|\int_{\theta_b}^{\pi-\theta_b} Q_n^1(\theta)\sin\theta\,\mathrm{d}\theta \tag{A.9}$$

$$F_{r,n}(s_1,s_2) = n(n+1)(1+2n)s_2 s_2^n M_n \cos(\phi_{r,n}-\phi_{r,1})\cdot|U_{r,n}|\int_{\theta_r}^{\pi-\theta_r} Q_n^1(\theta)\sin\theta\,\mathrm{d}\theta \tag{A.10}$$

note: $\phi_{b,n} = \arg U_{b,n}$ and $\phi_{r,n} = \arg U_{r,n}$.

$$U_{b,n} = \frac{\mu_r\left(k_n(aR_s s_1)X_n(aR_s s_1) + i_n(aR_s s_1)Y_n(aR_s s_1)\right)}{H_n} \tag{A.11}$$

$$\begin{aligned} U_{r,n} = &\frac{\mu_r\left(k_n(as_2R_s)X_n(as_1R_s) + i_n(as_2R_s)Y_n(as_1R_s)\right)}{H_n} \\ &+ \frac{(1+n)\left(i_n(as_2R_s)k_n(as_1R_s) - i_n(as_1R_s)k_n(as_2R_s)\right)}{H_n} \end{aligned} \tag{A.12}$$

$$Z_n(s_1,s_2) = n(n+1)(2n+1)^2 s_2^{2n-2} M_n^2 |V_n|\cdot|W_n|\sin(\phi_{p,n}-\phi_{q,n}) \tag{A.13}$$

note: $\phi_{q,n} = \arg V_n$ and $\phi_{p,n} = \arg W_n$.

$$\begin{aligned} V_n = &\frac{\mu_r\left(X_n(as_2R_s)Y_n(as_1R_s) - X_n(as_1R_s)Y_n(as_2R_s)\right)}{H_n(s_1,s_2)} \\ &+ \frac{(1+n)\left(k_n(as_1R_s)X_n(as_2R_s) + i_n(as_1R_s)Y_n(as_2R_s)\right)}{H_n(s_1,s_2)} \end{aligned} \tag{A.14}$$

$$W_n = U_{r,n} \tag{A.15}$$

CURRICULUM VITÆ

Linyu ZHU

02-11-1989 Born in Henan, China.

EDUCATION

2008–2012 B.Sc. in Detection, Guidance & Control
Northwestern Polytechnical University
Xi'an, China

2012–2015 M.Sc. in Navigation, Guidance & Control
Northwestern Polytechnical University
Xi'an, China

2015–2021 Ph.D. in Aerospace Engineering
Delft University of Technology
Delft, Netherlands

Thesis: Reaction Spheres for Attitude Control of Microsatellites

Promotor: Prof. dr. E.K.A. Gill

Promotor: Dr. J. Guo

List of Publications

Journal Papers

1. **Linyu Zhu**, Jian Guo, Eberhard Gill, *Motion Coupling Characteristics of Induction-Based Spherical Actuators*, to be submitted.

2. **Linyu Zhu**, Jian Guo, Eberhard Gill, *Performance Analysis of Induction-Based Reaction Spheres*, IEEE Transactions on Industrial Electronics **67**, 7746 (2019).

3. **Linyu Zhu**, Jian Guo, Eberhard Gill, *Analytical Field and Torque Analysis of a Reaction Sphere*, IEEE Transactions on Magnetics **54**, 1 (2018).

4. **Linyu Zhu**, Jian Guo, Eberhard Gill, *Review of Reaction Spheres for Spacecraft Attitude Control*, Progress in Aerospace Sciences **91**, 67 (2017).

Conference Papers

1. **Linyu Zhu**, Jian Guo, Eberhard Gill, *Scaling Effects in Miniaturization of Reaction Spheres*, the 69th International Astronautical Congress (IAC), Bremen, Germany. IAC-18, B4, 6A, 5, x45265 (2018).

2. **Linyu Zhu**, Jian Guo, Eberhard Gill, *Reaction Sphere for Microsatellite Attitude Control*, the 67th International Astronautical Congress (IAC), Guadalajara, Mexico. IAC-16,B4,6A,8,x35015 (2016).